A First Principles Approach to Understanding Geophysical Granular Flows

by

P.J. Zrelak

A dissertation accepted and approved in partial fulfillment of the
requirements for the degree of
Doctor of Philosophy
in Earth Sciences

Dissertation Committee:
Josef Dufek, Chair
Brittany Erickson, Core Member
Amanda Thomas, Core Member
Eric Corwin, Institutional Representative

University of Oregon
June 2025

DISSERTATION ABSTRACT

P.J. Zrelak

Doctor of Philosophy in Earth Sciences

Title: A First Principles Approach to Understanding Geophysical Granular Flows

Granular flow phenomena are ubiquitous in nature. Granular flow processes can be evidenced in, for example, hillslope creep, rock avalanches, landslides, debris flows, and concentrated pyroclastic density currents. Nevertheless, granular flows remain some of the most enigmatic natural phenomena. Advancements in the fields of granular physics and suspension rheology suggests that granular flow phenomenology, ranging from solid-like, liquid-like, to gas-like flows may be unified by a dimensionless shear rate. Here, I utilize this framework and simulate granular flows using discrete element methods, with the goal of understanding the relationship between internal processes and measurable signals. Chapter 2 presents data showing that granular forces exerted onto a rough substrate scale with a globally defined dimensionless shear rate and particle concentration. These forces record a change in state as the flow transitions from a liquid-like flow, where particles are in prolonged friction-like contact, to a gas-like limit where particles transmit momentum through binary-particle collisions. Chapter 3 relaxes the assumption of monodisperse flows over substrates with invariable boundary roughness by considering flows with disparate grain-size distributions, as well as flows over disparate basal plates that represent varying degrees of roughness. This shows that basal roughness and assemblage grain-size distribution has a direct effect on internal energy partitioning. Moreover, relatively smooth substrates can lead to shear localization that results in a flow regime where effective basal friction is dramatically reduced. The third chapter ends with a one-dimensional surface-wave propagation calculation showing that recorded spectra may indeed record granular-flow regime changes. Finally, Chapter 4 presents data exploring how granular flow history and emplacement processes can affect the stability of static piles on time-varying slopes. The data presented in this chapter show that the particle velocity auto-correlation function may be used to predict when a granular assemblage will fail and arrest. The chapters herein suggest that the discrete element approach can be used to improve flow models and explore ways

in which researchers can probe the internal dynamics of geophysical granular flows with indirect measurements, yielding a more refined understanding of natural hazards posed to life and infrastructure.

This dissertation contains both published and unpublished co-authored results.

ACKNOWLEDGEMENTS

I would like to thank my advisor Josef Dufek and the Department of Earth Sciences for giving me the privilege to apply my attention to the problems and processes herein. I would also like to thank Brittany Brand for providing me my undergraduate research experience. Without it, I would have never realized that graduate school and research was an option. I am also grateful for the guidance and support of Eric Breard, thank you for sharing your love for grains. Finally, I would thank my family, ancestors, J.J.B., and most importantly, Genesee Lucia.

To J.J.B and G.L.
ταὶς κάλαις' ὔμμιν ⟨τὸ⟩ νόημμα τῶ̂μον
οὐ διάμειπτον
Sappho, fr. 41, Carson

TABLE OF CONTENTS

Chapter Page

Chapter Page

LIST OF FIGURES

Figure Page

LIST OF TABLES

Table Page

CHAPTER I
INTRODUCTION

Granular materials are everywhere. They are (by weight) the second-most manipulated material in industry [de Gennes, 1999] and make up a significant portion of the Earth's surface providing the source material for mass transport phenomena. Granular media can be defined as particulate systems made of grains with diameters d larger than one micron, such that thermal agitation, and Brownian motion, are unimportant [Andreotti et al., 2013]. Despite their ubiquity, granular materials are enigmatic, and can span a wide range of dynamic conditions. Children playing in school-yard sandpits know this: collections of grains can act as a solid under static conditions, but once a yield criterion is met, the collection will flow like a liquid. This is one example of the rich phenomenology exhibited by granular materials. Nevertheless, understanding these systems is a key task for the mitigation of natural hazards posed by geophysical granular flows.

Examples of geophysical granular flows include landslides, debris flows, pyroclastic density currents, rock falls, avalanches, and even hillslope creep. What defines geophysical granular flow phenomenology are the variable admixtures of fluid and solid particle concentrations and the dynamic coupling between these two phases [Delannay et al., 2017, Jerolmack and Daniels, 2019, Lube et al., 2020, Guazzelli, 2024]. Moreover, any collection of particles has the capacity to make distinct dynamical transitions that are analogous to the phases of matter. For example, a debris flow may be sourced from a static pile of debris, to the extent that the pile is a perceptibly rigid mass that follows Coulomb friction and will not yield until some yield criterion is met [Iverson, 1997]. After initiation, a debris flow can, on average, behave visco-plastically. This fluid-like nature, after initiation, has led to great efforts in utilizing shallow-water equations to model these flows in transit (e.g., [George and Iverson, 2014, Iverson and George, 2014]). Nevertheless, this treatment ignores internal non-uniformity and unsteady processes that can lead to the apparently seamless transition from solid-like, liquid-like, to gas-like states. For example, both debris flows and dry granular flows can self channelize through the process of coarse-grained levee formation which can lead to increased runout distances [Rocha et al., 2019, Johnson et al., 2012, Kokelaar et al., 2014]. Moreover, debris flows can feature an internal architecture where the leading front is composed of a dilute granular-gas-like flow, exemplified by saltation and binary particle collisions [Iverson

et al., 2010]. This example highlights the need for a strong theoretical framework in which researchers can develop a unified understanding of these complex flows.

1.1 Granular flows viewed through the lens of soft-matter research

Jerolmack and Daniels [2019] presents a review of geophysical granular systems by considering Earth's surface as a soft-matter landscape. Soft matter can be simply defined as materials whose phenomenology depends on collective effects [de Gennes, 1992]. This means that soft matter displays complex emergent properties that cannot be defined apriori by knowing the physical properties of constituents comprising the system. This is exemplified by granular materials. For example, imagine a monodisperse (i.e., a single grain-size) system in which you know the microscopic particle-properties, such as the particle-friction coefficient μ_p. If knowing the properties of constituent parts was sufficient in understanding the properties of the bulk, then it may follow that knowing the particle-friction coefficient will give knowledge of the macroscopic friction coefficient μ—the ratio of internal shear and normal stresses. Then, by applying Mohr-Couloumb failure models (i.e., a solid-state mechanical model that determines the shear and normal stresses required to yield frictional materials), one may know the slope angle at which the collection of particles will yield and transition into liquid-like flowing states. Nevertheless, this is not the case (see Chapters 3 and 4 for data and discussion on this topic). In fact, it appears that excluded-volume effects—or the process in which particles are excluded from accessing nearby states (positions) because that state is occupied by another particle—plays a major role in dictating the rigidity of granular systems, such that a system of frictionless particles can have a macroscopic friction coefficient defining bulk rigidity [Peyneau and Roux, 2008]. Another key feature of soft matter is that bulk properties are responsive to external forcings; a material's current metastable state can rapidly change when it is perturbed. In a geophysical context, this can be viewed through hill-slope failure via a landslide. Critical-state soil mechanics attempts to model this feature by emphasizing the above mentioned Mohr-Coloumb failure model in continuum frameworks (e.g. Schofield and Wroth [1968]). Nevertheless, this model fails even in weakly-disorderd—i.e., non-crystalline—systems [Dansereau et al., 2019]. Furthermore, soft matter often exhibits glassy dynamics which, in the context of geophysical systems, is typified by soil creep. As such, a natural system can span dynamic conditions from, for example, sub-yield creep, to yielding bulk failure via a landslide, to the downstream development of a visco-plastic-like debris flow. The

implications for this is that models commonly considering each one of these processes in isolation are incommensurate with one another. Unification requires a better understanding of how granular systems behave under disparate driving conditions.

In recent decades, there has been a push to unify the rheologies of dry granular flows and particulate suspensions under a variety of shear rates and volume fractions. A product of this effort is the observed empirical relationship between the macroscopic effective friction coefficient μ and a dimensionless shear rate. In dry systems (where hydrodynamic forces do not play a role in governing bulk dynamics), this is expressed as the $\mu(I)$-rheology, where I is the dimensionless shear rate known as the inertial number [MiDi, 2004, Cruz et al., 2005, Jop et al., 2006]. In this context, the dry inertial number can be seen as a ratio of two timescale $I = \tau_p/\tau_f$, where τ_p is a microscopic timescale represented by particle motion under a confining pressure, and τ_f is macroscopic timescale defined by the bulk strain rate. A similar relation can be made when granular systems are immersed in a liquid phase, where the $\mu(I)$-rheology is replaced by the $\mu(I_v)$-rheology [Boyer et al., 2011]. I_v is the viscous number similarly expressing the ratio of microscopic and macroscopic timescales, where τ_p in I_v is the viscous drag timescale that is a function of the interstitial fluid viscosity. Further, through assuming additivity of stress scales I and I_v, a modified, or mixed inertial number can be introduced: $I_m = I_v + \alpha I^2$, where α is a fit parameter on the order of 1 [Trulsson et al., 2012, Amarsid et al., 2017, Guazzelli, 2024]. What necessarily follows from the the empirical rheologies $\mu(I)$, $\mu(I_v)$, and $\mu(I_m)$ is that the concentration becomes diagnostic of the dimensionless shear-rate. Therefore, a variety of geophysical granular-flow phenomena can be plotted in a phase space spanned by the concentration Φ and a dimensionless shear-rate (Figure 1). Plotted in this space are typical values for disparate processes and a black line expressing $\mu(I_v)$-rheology through the solids concentration for comparison. This provides a useful basis for describing geophysical granular flows, and will be central in the chapters that follow.

While advancements in soft-matter research and granular physics have brought about great insights into a variety of granular flow processes, this understanding has yet to be fully implemented in frameworks utilized by the Earth Science community. Nevertheless, there is a growing body of research that attempt to incorporate this soft-matter, granular, perspective into rheological analysis and modeling of geophysical granular flows. This includes D-CLAW, the previously mentioned depth-averaged model designed to reproduce dense debris flows, which defines dilatancy—or how

a volume of material changes with strain—as a function of the viscous number I_v [Iverson and George, 2014]. This is important for accurately modeling the pore-pressure feedback that alters debris-flow rheology [Iverson et al., 1997]. While this model has been effective in reproducing debris-flow runout (e.g., George and Iverson [2014]), it relies on a relatively simple basal friction model that will not capture the entire distribution of basal-granular forces that can affect substrate erosion and entrainment [McCoy et al., 2012]. Similarly, frameworks have been developed to forward model seismic signals generated via bed-load transport and debris flows by assuming uncorrelated particle impacts on the substrate [Tsai et al., 2012, Farin et al., 2019]. This approach provides an excellent first-order estimate of granular forcings, but ignores collective effects that typify soft matter. Despite this, recent studies have shown that incorporating rheolgical descriptions, typically applied to rather simple granular-fluid mixtures, effectively captures the rheology of natural samples [Kostynick et al., 2022, Pradeep et al., 2024]. This highlights the potential impact of using soft-matter research and granular mechanics to describe geophysical granular flows.

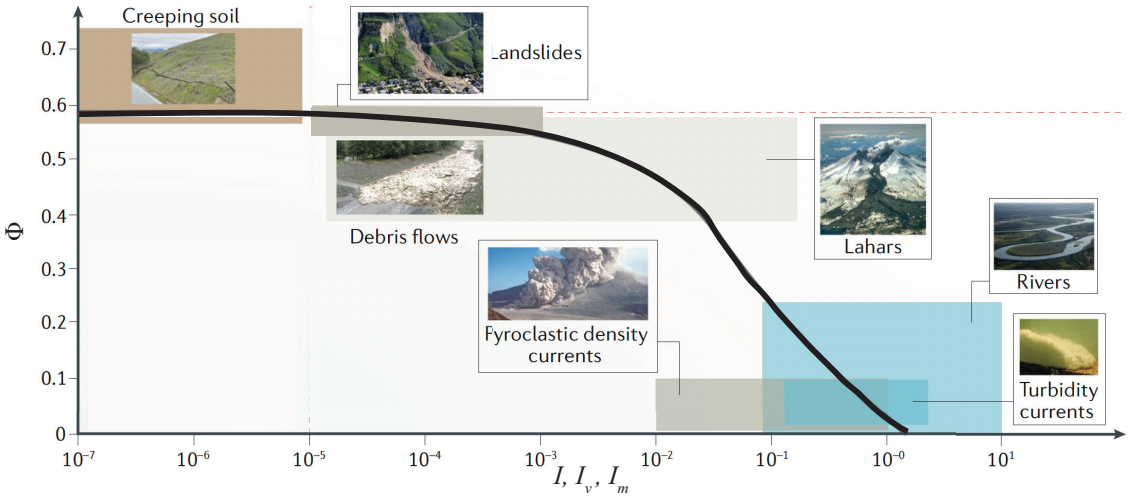

Figure 1. Phase space with fields representing disparate geophysical granular-flow phenomenon with their solids concentration Φ as a function of dimensionless shear rate I, I_v, or I. Black line depicts $\Phi(I_v)$-rheology from Houssais et al. [2016]. Adapted from Jerolmack and Daniels [2019]

1.2 Dissertation outline

In this dissertation, I present findings from my efforts in modeling granular flows from a first-principles perspective. This means that, rather than making assumptions

on the nature of particle-scale dynamics (as is required in, for example, a depth-average hydrodynamic approach), I explicitly resolve each individual grain in the system. This requires me to utilize discrete element methods in computational fluid dynamics (DEM-CFD), using the Department of Energy's software MFiX-DEM [Garg et al., 2012]. Resolving each individual particle in the system makes DEM-CFD is a powerful tool for improving our understanding of disordered systems, but also makes it intractable to simulate flows on the scale of real-world flows. Therefore, scaling arguments are used to relate numerical experiments to dimensionless numbers with values that are expected for natural flows. The overarching goal of this dissertation is to understand the relationship between bulk flow properties, internal energy partitioning, internal force fluctuations, and tractions imposed at the flow-substrate interface. This is, in-part, motivated by the fact that geophysical mass flows have the ability to emit remotely detectable geophysical signals [Allstadt et al., 2018]. Therefore, an improved understanding of how bulk flow properties relate to, for example, basal forces that generate seismic signals, may not only improve monitoring techniques, but will also allow for the development of improved flow models that can accurately reproduce flow substrate interactions.

Chapter 2 reports data derived from numerically modeled monodisperse granular flows in both dry and liquid-immersed states. In this chapter I report findings that basal force fluctuations can record a granular-phase change as flows transition from a liquid-like to gas-like states. Moreover, I suggest that this phase change results in a de-correlation in internal, and basal, force transmission. As such, approaches using the assumption that basal forces are derived from uncorrelated particle impacts with the substrate may fail to fully capture basal-force distribution. This has implications not only for modeling granular-flow induced seismic signals, but also for modeling transport processes such as substrate erosion and entrainment. Chapter 2 has been published in the *Journal of Geophysical Research: Earth Surface*.

Chapter 3 presents a follow-up study where I relax the null-hypothesis of monodisperse flow over a substrates that have a common roughness. This is in recognition that natural flows can have a variety of grain-size distributions, from well to poorly sorted, and that individual flows can traverse a variety of substrates, each with a different scale roughness. In this way I explore the effect grain-size distribution has on shaping the rheology of granular flows, and how boundary roughness affects internal energy partitioning. I end this study with a one-dimensional (1-D) steady-

state surface-wave propagation exercise to understand how changes in flow regime, grain-size distribution, and substrate roughness may lead to changes in signals recorded by off-channel receivers. I show that basal roughness directly controls the static friction coefficient, having implications for runout distance and flow initiation. Moreover, relatively smooth substrates lead to non-linear velocity profiles that can affect grain-size segregation, important for the development of lateral grading through coarse-grained levee formation, and the development of a 'supported' flow regime that reduces basal friction. When granular-flow assemblages are relatively fines enriched, internal energy is redistributed to internal kinetic energy fluctuations that decrease the power of basal-force signals. Finally, 1-D seismic wave propagation calculations suggest there is a optimal distance away from the channel at which granular flow regime changes can be observed. This chapter is submitted to *Journal of Geophysical Research: Earth Surface* and is in review.

Chapter 4 presents data from numerical experiments exploring how preparation history directly effects the slope angle at which granular assemblages reach a bulk-yielding state. I perform simulations in three phases: (1) granular assemblages are prepared by a prescribed shear-rate under plane-shear, (2) assemblages are emplaced by progressive deceleration or the instantaneous removal of flow-driving forcings, and (3) assemblages are 'placed' on time-varying slopes. I show that assemblage history is predominantly encoded within the static-state solids concentration and packing uniformity, with both the flow history and emplacement style affecting the assemblage's stability. This highlights the importance emplacement processes have on the metastability of granular piles. Moreover, through the velocity auto-correlation function, I show that the density of vibrational modes may be used to not only define bulk failure, but also predicts when jamming occurs as slope angles are decreased after bulk failure is achieved. Furthermore, there appears to be a slight signal that presages failure. Since previous work has used acoustic signals to calculate the density of vibrational modes, my findings suggest that acoustic techniques might be used to assess deposit stability. This chapter is unpublished work.

The Platonic dialogue *Timaeus* begins with the titular character conditioning his cosmological account with the words 'eikôs muthos', or 'likely story' [Zeyl and Sattler, 2023]. This expresses his belief that the veracity of his account scales with that which he is attempting to describe. Since the universe is a complex interaction of unsteady processes, the best he can do is give a likely story and not a definitive

account. This is an early example of the development of a theoretical framework, in that the theory is a function of the quality and amount of data available. The descriptions of geophysical granular flows in the preceding section is a likely story attempting to unify complex natural phenomena. This label is not intended to be disparaging, nor to express skepticism in its approach; rather, it signals that the above description offers an excellent framework that can, and must, be continually built upon. In the following chapters, I use this likely story—this understanding of granular-flow phenomena as soft-matter systems potentially unified under a single theoretical framework—not only to improve modeling and monitoring techniques, but also to provide a clearer sense of how researchers might use measurable signals to continually refine our understanding of these enigmatic events.

CHAPTER II
BASAL FORCE FLUCTUATIONS AND GRANULAR RHEOLOGY: LINKING MACROSCOPIC DESCRIPTIONS OF GRANULAR FLOWS TO BED FORCES WITH IMPLICATIONS FOR MONITORING SIGNALS

From *P. Zrelak, E. Breard, and J. Dufek. Basal force fluctuations and granular rheology: Linking macroscopic descriptions of granular flows to bed forces with implications for monitoring signals. Journal of geophysical research. Earth surface, 129(7), 2024.*

2.1 Introduction

Flowing granular mixtures are prevalent in nature. Geophysical mass flows experience a range of granular interactions due to spatio-temporal variations in particle concentration, particle-fluid-particle interactions, grain size distributions, and shear rates. Debris flows, pyroclastic density currents, and debris avalanches showcase complex phenomenological behavior that is intrinsic to granular materials. In this view, debris flows are fluid-particle mixtures that can span from dilute, near hyperconcentrated flow conditions, to dense flows able to support large clasts [Iverson, 1997]. Pyroclastic density currents, gravity flows of volcanic particles and gas, display enhanced mobility that is attributed to the liquid-like nature of gas fluidized granular flows and the development of pore pressure (e.g., Lube et al. [2019], Breard et al. [2023]). Each of these disparate phenomena can span from dry conditions, where particle inertia allows for drag effects to be neglected, to fluid immersed conditions, where fluid drag and pore pressure gradients become important [Delannay et al., 2017, Lube et al., 2020]. Moreover, these geophysical flows can produce remotely detectable seismic signals (e.g., Allstadt et al. [2018]). It is our goal to aid in developing a framework relating basal forces that drive seismicity to bulk rheology. In this effort, we will report on data derived from granular flow numerical simulations utilizing discrete element methods where individual particle motion is explicitly resolved in the presence, and absence, of an interstitial continuous fluid. We will use these simulations to observe flow rheology under disparate shear states which can be expressed via non-dimensional parameters, allowing us to compare our scaled simulations to large scale geophysical mass flows. During these simulations we will be recording basal forces exerted on a simulated force plate, allowing us to relate bulk flow rheology to measured forcings.

Several processes are involved in the generation and transmission of seismic waves from source to receiver. A recorded seismic signal e.g., ground velocity $\dot{u}(t)$, measured at some distance from the flow, is a result of a convolution of three functions:

$$\dot{u}(t) = F(t) * g(t) * r(t) \tag{2.1}$$

with $F(t)$ being the time-varying forces exerted on the substrate (i.e., source function), $g(t)$ being a transfer function—known as the Green's function—representing path effects that attenuate and disperse forcing energy, and $r(t)$ being the instrument impulse response (e.g., Stein and Wysession [2003]; Figure 2). Much effort has been invested in utilizing geophysical signals to inform scientists and hazard coordinators, with the aim to improve detection and monitoring. For example, time and spectral characteristics of seismic signals have been used to train machine learning algorithms to detect debris flow events (e.g., Chmiel et al. [2021]); seismic envelopes have been correlated to event volume (e.g., Levy et al. [2015]) and potential energy loss (e.g., Farin et al. [2018]); and the ratio of horizontal and vertical ground displacements have been used to posit turbulent flow conditions [Cole et al., 2009, Walsh et al., 2020]. Nevertheless, the link between internal dynamics and the source function $F(t)$ is a non-trivial one. Allstadt et al. [2020] report data from controlled, large scale ($8-10\ m^3$), debris-flow experiments and calculated empirical green's functions, constraining the path effects term $g(t)$. This allows the authors to invert basal tractions from seismic signals recorded by near-channel receivers. These inverted forces compare well with in-channel force plate measurements. However, the authors were limited in their ability to use these inverted signals to infer detailed flow information due to the poorly constrained relationship between macroscopic flow dynamics and boundary forcing.

Measuring boundary forces, thus constraining the source function $F(t)$, is important to understand not only how seismic forces are generated, but how flows affect and are affected by their environment. McCoy et al. [2013] measure basal forces in natural debris flows, relating these basal forces to channel incision. These authors leverage the high rate of debris flow events per year at their study site (Chalk Cliffs, CO), instrumenting the channel with a variety of sensors, creating a natural laboratory. Nevertheless, collecting data from real-world flows is difficult, providing the need for controlled experiments. Large-scale debris-flow experiments have been conducted at a controlled test site in Blue River, Oregon, USA since 1994 [Iverson et al., 2010]. Here, a wealth of data is collected and disparate sensor

arrays supply multiple data streams to analyze a flow. These experiments not only provided data for Allstadt et al. [2020] but also for the development of depth-averaged models [Iverson and George, 2014, George and Iverson, 2014], and, in general, led to a more refined understanding of the physics of debris flows [Iverson, 1997]. Large-scale experiments are needed to reliably recreate near-scale geophysical flows. Nevertheless, as experimental scale increases, so does uncertainty. For example, near-scale experiments utilizing natural particles (e.g., sand and gravel) may have complex shape and size distribution, which may lead to unforeseen phenomenon. Further, steady states are difficult to maintain when conducting large experiments. These uncertainties, paired with the resources required for conducting such experiments, highlights the need for smaller, scaled experiments. Researchers have utilized scaled experiments in various configurations to observe the probability distribution of boundary forces and the dynamical nature of these forces as they approach the jamming transition [Longhi et al., 2002, Corwin et al., 2005, Gardel et al., 2009, Kheiripour Langroudi et al., 2010]. The development of force chains in granular flows has been shown to create bed-force localization that can greatly exceed mean forces [Estep and Dufek, 2012]. Other authors have looked at forces generated during individual particle-impact events, deriving scaling laws relating the mass and speed of the particle to energy transferred to the boundaries [Farin et al., 2015]. Recent work has performed monodisperse inclined-slope flow experiments, recording basal forces at high frequencies, comparing these data to modeled data from stochastic impact models [Arran et al., 2021]. Importantly, these authors find that the normalized squared basal-force fluctuation, in the intermediate and high frequency ranges associated with uncorrelated particle interactions, is related to the bulk scaled shear rate.

In the limit where grain-inertia dominates flow behaviour (e.g., unsaturated debris avalanches, the snouts of particle concentrated pyroclastic flows, and the coarse front of debris flows), substrate forcing, like bulk flow dynamics, is expected to be controlled by particle-particle interaction [Forterre and Pouliquen, 2008]. Previous efforts show that sheared granular media span three distinct regimes that are related to the shear rate: (1) stick-slip unsteady motion, (2) continuous deformation of the granular bed, (3) high energy collisional flow, with the nature of particle velocity fluctuations being controlled by these regimes [Cruz et al., 2005]. Velocity fluctuations are what give rise to a quantity referred to as granular temperature [Lun et al., 1984].

Much like the thermal temperature of a gas, this quantity measures fluctuations in kinetic energy of individual particles in a system, generating a variance in the particle velocity distribution. While often treated as isotropic, heterogeneties in granular flows may give rise to local anisotropy in granular temperature, i.e. velocity fluctuations in different directions may vary in magnitude. As opposed to molecular gasses, granular systems are by definition in a perpetual state of dis-equilibrium due to energy being dissipated through inelastic particle-particle and particle-domain interactions [Goldhirsch, 2008]. Trulsson et al. [2012] show that the dissipation mechanism in dense granular suspensions is a function of confining pressure P_s scaled by the interstitial fluid's viscosity η_f: $\sqrt{\rho_s P_s} d/\eta_f = I/\sqrt{I_v}$, where ρ_s is the solid particle density, I is the inertial number from Cruz et al. [2005], and I_v is the viscous inertial number from Boyer et al. [2011] (Eqs. (2.13) and (2.14), respectively). As this scaled confining pressure (i.e., $I/\sqrt{I_v}$) approaches 10, contact forces increase rapidly to a limit where dissipation is controlled solely by particle contacts, and the flow behaves as a pure granular flow. In other terms, the dissipation mechanism in fluid immersed flows is dictated by the competition between confining pressure (this can be referred to as the solids pressure, or the pressure that the granular material exerts upon itself), and viscous effects. Further, scaling laws relating wall friction to slip velocity scaled by velocity fluctuations provides evidence that fluctuations are key to describing dense flows near wall boundaries [Artoni and Richard, 2015]. This suggests that flow information may be extracted from force fluctuations, or through the measurement of energy dissipation, near the flow-boundary.

While much progress has been made on end-member conditions, detailed information of bed-force distributions across a range on inertial numbers is still lacking. Here we perform a series of three-dimensional numerical simulations utilizing the discrete element method (DEM) to examine granular contributions to wall forcing, thus observing the source-time function $F(t)$ in Eq. 2.1 as a function of flow state. The discrete element approach resolves the interactions of individual particles with the bottom boundary, enabling a high resolution record of bed forces across a range of flows at different flow states. With DEM, we can track the forces associated with each individual particle in the system, rather than estimating granular stresses through, for example, theoretical relations or phenomenological approximations between flow properties and particle forcings that may rely on simplifying assumptions. The goal of this study is to relate macroscopic descriptions of granular flows to basal forcing

under ideal conditions, but over a wide range of inertial numbers. We will first briefly describe our methods, pointing the reader to preceding studies that advanced these efforts. Then, in Section 2.3, we will detail bed-averaged flow conditions, afterwards discussing basal forces recorded under these conditions in Section 2.3.2. We will close with a discussion relating the two observations culminating in a phase space spanned by our data in Section 2.4.2, and examine the implications of these efforts as we scale towards real-world flows in Section 2.4.3.

2.2 Methods

2.2.1 MFiX-DEM

Our three-dimensional numerical simulations are conducted using the Department of Energy MFiX-DEM solver. Detailed information on MFiX-DEM is discussed in [Garg et al., 2012]. MFiX-DEM solves the ordinary differential equations governing the motion of the i^{th} particle

$$m_i \frac{d\mathbf{V}_i}{dt} = m_i \mathbf{g} + \mathbf{F}_d(t) + \mathbf{F}_c(t) \tag{2.2}$$

where $\mathbf{V}_i$ is the velocity of the particle, $\mathbf{g}$ is the gravity vector, $\mathbf{F}_c(t)$ is the net contact forces associated with contacting particles, m_i is the mass of the i^{th} particle, $\mathbf{F}_d(t)$ is the drag forces acting on the i^{th} particle, and t is time. We perform our simulations under steady state conditions. Consequently, the added mass and history terms of the generalized Basset-Boussinesq-Oseen equation, arising due to unsteady fluid flow relative to the solid particles, are neglected [Maxey and Riley, 1983]. We use the soft-sphere approach to particle contacts, modeling collisions and particle overlap as interactions between systems composed of springs and dashpots. In this way, the spring supplies the energy for rebound, gaining potential energy during collision and releasing post-collision; the dashpot simulates dissipation due to inelasticity. Thus, the net contact force in Eq. (2.2), in the normal direction, becomes a sum of the elastic ($F^n_{k_n}$) and viscous (F^n_η) components

$$F^n_c = F^n_{k_n} + F^n_\eta = -(k_n \delta_n + \eta_n |V^i_n - V^j_n|) \tag{2.3}$$

where scripts n in the above and subsequent equations represent parameters in the normal direction. The net contact force is used to visualize force chain magnitude, where the magnitude is the norm of the contact forces. The midpoint of a single 'link' in a force chain is the contact point between two particles, and the length of this link is the distance between the centers of the two particles. Interconnected

links of this kind constitute a force chain. The elastic contribution in Eq. (2.3) is controlled by the elastic coefficient k_n and the particle overlap in the normal direction, δ_n. The viscous contribution is a function of the dampening coefficient η_n and the relative normal velocities V_n of the i^{th} and j^{th} contacting particles. The dampening coefficient is dictated by the elastic coefficient, normal coefficient of restitution e_n, and the effective mass m_{ef} between the two colliding particles

$$\eta_n = \frac{2\sqrt{m_{ef}k_n}|ln\ e_n|}{\sqrt{\pi + ln^2\ e_n}} \tag{2.4}$$

Tangential elastic and viscous coefficients are related to their normal counterparts by a simple scale factor (i.e. $k_t = \frac{2}{5}k_n$ and $\eta_t = \frac{2}{7}\eta_n$). The minimum collision time between two particles is dictated by the elastic and viscous coefficients:

$$t_n^{col} = \pi \left(\frac{k_n}{m_{ef}} - \frac{\eta_n^2}{4m_{ef}^2} \right)^{-1/2} \tag{2.5}$$

Timesteps are set to $0.2t_n^{col}$ to resolve collisional interactions.

In the case where particles are submerged in a fluid, continuum mechanics are introduced and the fluid is governed by continuity and momentum conservation detailed in [Syamlal et al., 1993]:

$$\frac{D}{Dt}(\epsilon_f \rho_f \mathbf{u}_f) = \nabla \cdot \overline{\overline{S}}_f + \epsilon_f \rho_f \mathbf{g} - \mathbf{I}_f \tag{2.6}$$

Where D/Dt is the material time derivative, ϵ_f is the fluid volume fraction, ρ_f is the fluid density, $\mathbf{u}_f$ is the fluid velocity, and $\overline{\overline{S}}_f$ is the fluid phase stress tensor. Coupling between the continuous (fluid) and discrete (solid) phases is incorporated in the interphase momentum exchange term $\mathbf{I}_f$, which is derived from the drag force in Eq. (2.2):

$$\mathbf{I}_f^k = \frac{1}{\nu_k} \sum_{i=1}^{N_s^k} \mathbf{F}_d^{i \in k} K(\mathbf{X}_{i \in k}, \mathbf{x}_k) \tag{2.7}$$

This states that the interphase momentum exchange in the k^{th} computational cell is dictated by the particle drag force $\mathbf{F}_d^{i \in k}$ associated with the i^{th} particle residing within the cell with a volume ν_k. The particle force within the cell is modulated by the kernel $K(\mathbf{X}_{i \in k}^i, \mathbf{x_k})$, which weights the force of a particle in the k^{th} cell, located by $\mathbf{X}_{i \in k}$, to the grid node located by $\mathbf{x}_k$. This modulated drag force is then summed over all particles residing in the computational cell, N_s^k. Particle drag becomes a sum

of contributions from the fluid pressure gradient in the k^{th} cell and drag due to the relative velocity between the solid and fluid phases

$$\mathbf{F}_d^{i\in k} = -\nabla P_f(\mathbf{x}_k)\nu_s + \beta_s^k \frac{\nu_s}{\epsilon_s}\left(\mathbf{V}_f\left(\mathbf{X}_{i\in k}\right) - \mathbf{V}_i\right) \tag{2.8}$$

where $\nabla P_f(\mathbf{x}_k)$ is the cell centered fluid pressure gradient, ν_s is the volume of the solid phase particle, ϵ_s is the solid phase volume fraction, β_s^k is the momentum exchange coefficient for all solids residing in the k^{th} cell, and $\mathbf{V}_f(\mathbf{X}_{i\in k})$ is the interpolated mean fluid velocity at the particle location. Combining Eqs. (2.7) and (2.8), the momentum exchange between the fluid and solid phase becomes:

$$\mathbf{I}_f^k = -\epsilon_s \nabla P_f(\mathbf{x}_k) + \frac{1}{\nu_k}\beta_s^k \frac{\nu_s}{\epsilon_s}\left(\mathbf{V}_f\left(\mathbf{X}_{i\in k}\right) - \mathbf{V}_i\right) K(\mathbf{X}_{i\in k}, \mathbf{x}_k) \tag{2.9}$$

β_s^k is calculated using the model outlined in Gidaspow [1994]. The expression for the exchange term is dependent on the fluid volume fraction in the cell

$$\beta_s^k = \begin{cases} 150\frac{(1-\epsilon_f)^2\eta_f}{\epsilon_f d^2} + 1.75\frac{\rho_f|\mathbf{V}_f(\mathbf{X}_{i\in k})-\mathbf{V}_i|\epsilon_f}{d}, & \text{if } \epsilon_f < 0.8 \\ 0.75 C_D \frac{\epsilon_f|\mathbf{V}_f(\mathbf{X}_{i\in k})-\mathbf{V}_i|}{d}\epsilon_f^{-2.65}, & \text{if } \epsilon_f > 0.8 \end{cases} \tag{2.10}$$

where d is the particle diameter and η_f is the fluid phase viscosity. Thus, the momentum exchange scale factor is a function of solid and fluid phase properties, the relative average velocities between the solid and fluid phases, and the drag coefficient C_D, which itself is a function of the cell's particle Reynolds number Re^k, a non-dimensional number relating the ratio of fluid-inertial to viscous forces:

$$C_D = \begin{cases} \frac{24}{Re^k}\left(1 + 0.15\left(Re^k\right)^{0.687}\right), & \text{if } Re^k < 1000 \\ 0.44, & \text{if } Re^k > 1000 \end{cases} \tag{2.11}$$

This correlation between the drag coefficient and the Reynolds number works to reproduce the standard drag curve relating a sphere's drag coefficient to the Reynolds number (e.g., Bird [1960]). Note that our simulations are within the dense regime and never reach conditions such that $\epsilon_f > 0.8$.

To relate the resolved dynamics of individual particles to macroscopic flow properties we employ coarse-graining techniques (CG). CG is a computational tool to derive continuous fields from discrete data. We utilize a CG technique developed by Fullard et al. [2019] and Breard et al. [2020] following the effort of Weinhart et al. [2013] (see methods and references, therein, and Appendix A.1 for more information on parameters relevant for scaling).

2.2.2 Scaling

This study is concerned with the unit problem of relating basal forces to macroscopic characteristics of granular flows. Due to computational restraints, the simulation setup (described in Section 2.2.3) is orders of magnitude smaller than real-scaled geophysical mass flows. Nevertheless, analyzing these flows in terms of non-dimensional parameters can provide first-order constraints on the physics that govern mass flow. Though the absolute values of parameters used in our simulations differ from those of real-world particles and flows, non-dimensional parameters allow us to examine the ratios of stress states and timescales such that rudimentary conclusions on momentum transport, rheology, and the overall self-similarity in character of a range of granular flows can be attained.

First, we define the effective friction coefficient, or the ratio of shear to normal stresses, as

$$\mu = \frac{|\sigma_{xy}|}{P_s} \tag{2.12}$$

where $|\sigma_{xy}|$ is the domain integrated (coarse-grained) shear stress, and the P_s is the solids pressure (or the pressure generated by the collection of particles that acts upon itself). This friction coefficient is similar to, though is an emergent parameter of, the particle friction coefficient that is assigned to each particle (μ_p). The effective friction coefficient μ is a constitutive property defined for an entire collection of particles that is a constant of proportionality relating shear stresses to the normal stresses [MiDi, 2004, Cruz et al., 2005]. In dense granular flows, μ is itself a function of the non-dimensional parameter referred to as the inertial number:

$$I = \frac{\dot{\gamma} d}{\sqrt{P_s/\rho_s}} \tag{2.13}$$

where $\dot{\gamma}$ is the coarse-grained shear rate. The inertial number is a quantity that defines the 'inertial state' of a granular flow, which in turn has been used as a proxy for flow state or regime. This non-dimensional parameter can be seen as a ratio of the microscopic timescale for particle rearrangement under a confining pressure ($\tau_{micro} = d/\sqrt{P_s/\rho_s}$), and the timescale for macroscopic deformation as a granular bed is sheared ($\tau_{macro} = 1/\dot{\gamma}$) [MiDi, 2004, Cruz et al., 2005, Forterre and Pouliquen, 2008]. In this way, at low shear rates and high confining or solids pressures, the inertial number will be low, meaning the timescale for bulk bed deformation is large, and particle motion is relaxed via rearrangement events. This mean that the granular

'flow' is characterized by intermittent stick-slip events, rather than bulk failure of the granular bed.

Jop et al. [2006] uses the phenomenological relationship between the effective friction coefficient and inertial number to develop a generalized constitutive model for dense granular flows. This model ultimately relates the friction coefficient law $\mu(I)$ to the stress and shear-rate tensors through the use of an effective viscosity defined by $\mu(I)$. In the limit of vanishing shear rates, the model predicts that flow will only occur when the magnitude of shear stresses overcome a fictional yield criterion (e.g., $|\sigma_{xy}| > \mu P_s$). Below this, the collection of grains will behave as a rigid system. This $\mu(I)$ rheology has seen success in modeling dry granular systems and has been been extended to include dense granular suspensions (i.e., multiphase granular flows) [Boyer et al., 2011]. This extension utilizes a dimensionless parameter known as the viscous number, expressing the ratio between inertial particle stresses and viscous stresses

$$I_v = \frac{\eta_f \dot{\gamma}}{P_s} \tag{2.14}$$

Where η_f is the viscosity of the interstitial fluid. This viscous inertial number can be written as a function of the inertial number and the Stokes number St, $I_v = I^2/St$, where

$$St = \frac{\dot{\gamma} d^2 \rho_s}{\eta_f} \tag{2.15}$$

The Stokes number is a ratio between the particle timescale characterizing the decay in the particle's velocity due to drag, and the fluid timescale that describes bulk fluid deformation; when $St < 1$ particles may act as passive tracers in a background flow field. A scaling law unifying I and I_v was introduced by Trulsson et al. [2012] and written as the modified inertial number I_m by Amarsid et al. [2017]:

$$I_m = \left(\alpha I_v + I^2\right)^{1/2} = I\left(\frac{\alpha}{St} + 1\right)^{1/2} \tag{2.16}$$

where α is a constant fitting parameter typically of order 1 Amarsid et al. [2017]. When $St \to 0$, time scales are dictated by viscous forcing, thus I_m is dominated by the viscous number I_v. Conversely, when particles gain inertia, and $St \to \infty$, I_m reduces to I, signifying that dry granular processes control the system. In this study, we have opted to use the dry inertial number I, rather than the modified inertial number I_m, as our results indicate that, not only does the bulk of our simulations fall into the category where the Stokes number St is greater than one, but that it appears

that dry inertial number is sufficient in describing the quantities of interest (Figures A.32 and A.33).

Alternative non-dimensional parameters are discussed in the context of debris flows by Iverson [1997] and can be related to the inertial number I and viscous number I_v [Delannay et al., 2017]. The Savage number N_{Sav} is a dimensionless ratio expressing particle inertial stresses and stresses generated by the weight of the flow. If it is assumed that hydrostatic forces are driven by the the solids pressure P_s, N_{Sav} is simply the square of I:

$$N_{Sav} = \frac{\rho_s \dot{\gamma}^2 d^2}{(\rho_s - \rho_f) g H} = \sqrt{\frac{\dot{\gamma}^2 d^2 \rho_s}{P_s}} = I^2 \tag{2.17}$$

Where ρ_f is the density of the fluid phase (if present), g is the gravitational constant, and H is the thickness of the granular flow. Large-scale sand gravel debris-flow flume experiments conducted by the USGS have estimated values of $N_{sav} \sim 0.1$ [Iverson, 1997]. Similarly, the viscous number I_v and inertial number I can be related to the Bagnold number N_{Bag}

$$N_{Bag} = \frac{\Phi \rho_s \dot{\gamma} d^2}{(1 - \Phi)\eta_f \dot{\gamma}} \sim \frac{I^2}{I_v} = \frac{\dot{\gamma} d^2 \rho_s}{\eta_f} \tag{2.18}$$

Where Φ is the concentration, or solids volume fraction, of particles. The Bagnold number N_{Bag}, is similar to the viscous number I_v in that is expresses the ratio of particle inertial stress to viscous fluid stresses. N_{Bag} estimates for large-scale debris-flow flume experiments are on the order of $\sim 10^2$ [Iverson, 1997]. Table 1 expresses the range of non-dimensional parameters for our simulations.

2.2.3 Simulation Setup

We perform two classes of simulations in disparate configurations: monodisperse plane-shear and monodisperse inclined-slope flows. Table 1 provides a summary of simulation parameters.

In plane-shear configurations, a bed of particles is confined between two plates made frictional and bumpy, being composed of particles that comprise the bed (Figure 2(b-c)): the lower plate is made static and acts as a force plate (with an RMS surface roughness $S_a \approx 0.6d$; Appendix A.3) recording particle forces (see Section 2.2.4); the top plate imposes a constant confining pressure and translational velocity, shearing the bed of grains and initiating flow. The top plate is rigid and contains particles detached downwards from the main body of the plate (Figure 2c). This keeps the flow particles from reaching crystallized states. We keep a constant confining pressure

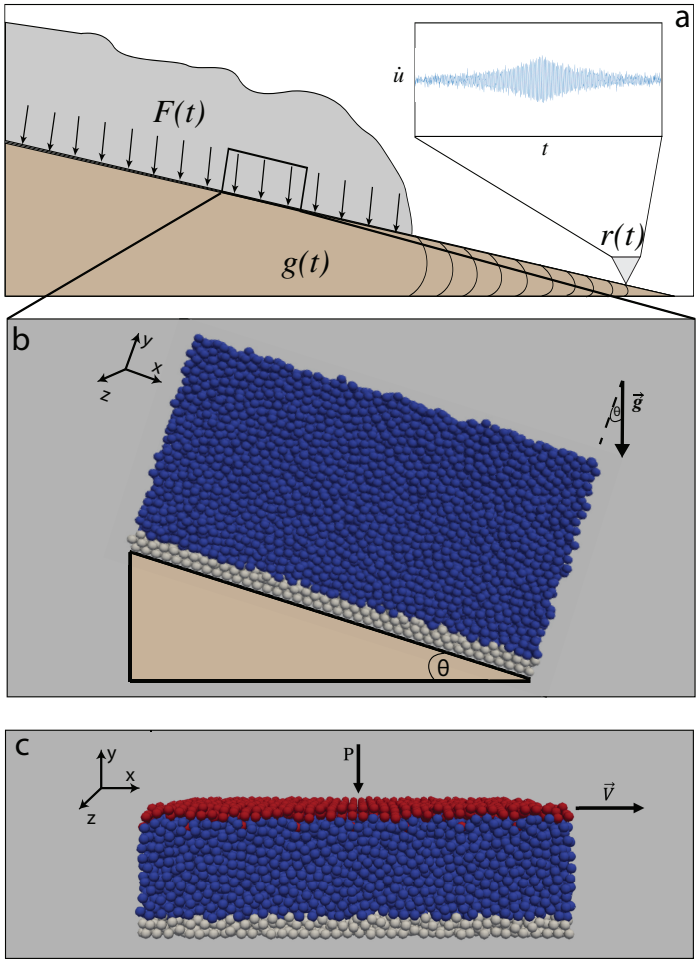

Figure 2. (a) Cartoon depicting radiation of elastic energy to receiver via forces exerted by the flow on the substrate and (b-c) renderings of simulation configurations addressing the unit problem of bed forces exerted by granular flows: (b) inclined-slope flow where gravity is rotated by an angle θ to simulate gravitational forces on a slope; (c) plane-shear configuration, where red particles act as a coherent plate, imposing a constant confining pressure and translational velocity on the blue particles. Gray particles on the bottom of the Y-Z plane act as a static rough and frictional 'force plate'.

of 2000 Pa, allowing the height of the bed to evolve due to Reynolds dilation. The relatively low confining pressure, compared to meter scale geophysical flows, will have an effect on the inertial number reached at a given shear rate (see denominator of Eq. 2.13). Nevertheless the physical processes at a given flow state described by the inertial number will remain the same. Periodic boundary conditions are imposed in the stream (x) and span-wise (z) directions, with both directions having dimensions

equal to $40d$, this is chosen to ensure that simulation dimensions are larger than contact networks that occur in low shearing conditions [Sun et al., 2010]. In this configuration, we conduct two categories of simulations, pure granular flows (particles sheared in a vacuum) and flows submerged in two types of fluids: one with a density of 1000 kg/m^3 and viscosity 8.90×10^{-4} $Pa\ s$, and a more viscous liquid with the same density and a viscosity of 0.01 $Pa\ s$. The more viscous liquid was chosen to be an order of magnitude greater than water due to the viscosity of sediment-laden water in debris flow mixtures being 10 to 100 times greater than water [Iverson, 1997]. Within these two categories (i.e. fluid submerged and dry granular flow), we run two sets of simulations, changing the bed composition from a monodipserse composition of 500 μm to a composition of 5 mm particles, while keeping the density constant at 1050 kg/m^3. This density value provides a slight negative buoyancy in the presence of the interstitial fluid, and is motivated by the density of volcanic tephra [Shipley and Sarna-Wojcicki, 1993]. We vary the top plate velocity such that the simulations span global shear rates from $10^{-2} - 10^3$ Hz, developing creeping to collisional granular flows. Particle friction is held constant across the simulations at $\mu_p = 0.53$.

Inclined plane simulated-flow configurations are conducted similarly, being composed of monodipserse beds placed on top of a frictional and bumpy (force) plate. The bed of particles is first allowed to settle under gravity on a horizontal plane. Then, the gravity vector is rotated to an angle θ such that $\theta > \theta_s$, where θ_s is the angle of repose, and the configuration is destabilized. After bed failure, the gravity vector is either rotated to greater values, or decreased below the angle of repose dictated by particle friction, utilizing the hysteretic nature of granular materials [Pouliquen, 1999]. In this way, inclined-slope simulations reach shear rates from $\sim 10^{-1} - 10^2$ Hz. In these configurations, we maintain a minimum bed height of $20d$, avoiding scale effects for thin flows [Pouliquen, 1999].

Table 1. Summary of simulation parameters.

parameter	*variable*	*value*
Solid Parameters		
diameter[1] [m]	d	$0.005,\ 0.0005$
density $[kg\ m^{-3}]$	ρ_s	1050
elastic coeff. $[Pa\ m]$	k_n	$(2 \times 10^8)d$
angle of repose [°]	θ_s	≈ 20
particle friction coeff.	μ_p	0.53
restitution coeff.	e_n	0.6
Fluid Parameters		
density $[kg\ m^{-3}]$	ρ_f	1000
viscosity[1,2] $[Pa\ s]$	η_f	$8.9 \times 10^{-4},\ 10^{-2}$
Simulation Parameters		
domain size $[m]$	$X \times Y \times Z$	$40d \times \geq 20d \times 40d$
confining pressure[3] $[Pa]$	P_p	2000
top plate velocities[1,3] $[ms^{-1}]$	V_p	$0.0001 - 16$
inclination angle[1,4] [°]	θ	$20.5 - 28$
Numerical Parameters		
DEM solver timestep $[s]$	dt_s	$\frac{\pi}{50}\left(\frac{k_n}{m_s} - \frac{\eta_n^2}{4m_s^2}\right)^{-1/2}$
fluid solver timestep[2] $[s]$	dt_f	$(2 \times 10^{-2})d$
Non-dimensional Parameters		*simulation range*
Inertial Number	I	$10^{-4} - 10^0$
Viscous Number[2]	I_v	$10^{-9} - 10^{-2}$
Stokes Number[2]	St	$10^{-3} - 10^3$
Savage Number	N_{Sav}	$10^{-9} - 10^1$
Bagnold Number[2]	N_{Bag}	$10^{-3} - 10^4$

[1]Parameter takes on one of the values listed for a single simulation
[2]Parameter relevant when interstitial fluid is present
[3]Parameter for plane-shear configuration
[4]Parameter for inclined-slope flows

2.2.4 Wall Analyses

To link macroscopic flow properties to forcings exerted on the bottom boundary, we record the forces exerted by all particles that are in contact with the bottom rough static plate. In this way, the bottom plate acts as a force plate. We shear the bed of grains until the system reaches a steady state (Figure A.35), and at this point we record forces at this bottom boundary with a frequency of 100 kHz across all simulations. Particle forces are summed across the entire plate, acknowledging that the frequency of this forcing is a function of the size of the numerical force plate [Iverson, 1997, Jalali et al., 2006]: decreasing the area in which particle forces are summed increases the frequency of forcing by the factor at which the plate dimensions are reduced (see Section 2.4.3 for observations and discussion on this effect). From these plate measurements, we calculate the power spectral density (PSD)

$$P(f) = \frac{N}{\Delta f}|\tilde{F}(f)|^2 \tag{2.19}$$

where $\tilde{F}(f)$ is the Fourier transform of the total forcing time-series on the lower plate boundary, N is the number of discrete observations (length of the time-series), and Δf is the sampling frequency. Arran et al. [2021] uses the PSD as a measure of the squared fluctuating force. Similarly, we express the fluctuating force as an integrated PSD and normalize it by the time averaged total force (total sum of individual forces) exerted on the bottom plate, squared

$$\Lambda = \frac{\int^{f_{ny}} P(f)df}{\langle F(t)\rangle^2} \tag{2.20}$$

where the upper bound of integration is the Nyquist frequency and angled brackets denote time averaging. Effectively, Eq. (3.13) allows us to examine how the bandwidth of forcing spectra changes with flow state, as well as the amplitude of forcing fluctuations relative to the steady-state time-averaged forcing measured by our force plate. Normalization helps encapsulating any magnitude effects that correspond to the bed's weight as well as the momentum transferred from impacts that are fundamentally a function of particle size [Tsuji et al., 1992, Yohannes et al., 2012]. The amplitude spectrum of the force-plate time series is also used to calculate the mean frequency of the forcing [Vinningland et al., 2007, Farin et al., 2015]

$$\bar{f} = \sum \frac{\tilde{A}[f_i] f_i}{\sum \tilde{A}[f_i]} \tag{2.21}$$

where $\tilde{A}$ is the discrete amplitude spectrum. Forces and velocities at the force plate are used to calculate parameters similar to those described in Section 2.2.2. The effective wall friction coefficient μ_w is the ratio of the time averaged sum of basal forces in the stream-wise and plate-normal directions [Artoni and Richard, 2015]

$$\mu_w = \frac{\langle F_x(t) \rangle}{\langle F_y(t) \rangle} \tag{2.22}$$

Similarly, we compare the CG'd granular (the granular temperature averaged over the entire flow) temperature to the granular temperature at the bottom force-plate wall, defined as the time and spatially averaged mean squared velocity fluctuation of particles in contact with the bottom plate (thus, slip velocities)

$$T_i^w = \left\langle (v_i^w - V_i^w)^2 \right\rangle \tag{2.23}$$

Where T_i^w is the wall granular temperature in the i^{th} direction, v_i^w is the wall-averaged instantaneous velocity in the i^{th} direction, and V_i^w is the time and wall averaged slip velocity in the i^{th} direction. Note, as with all parameters defined at the force plate, uncertainty increases with shear rate, as the total number of particles in contact with the bottom plate at write-out decreases.

2.3 Results

2.3.1 Granular Rheology

The rheology of granular flows and concentrated suspensions is well established with empirical constitutive laws taking the form $\mu(I)$ and $\Phi(I)$, stating that the effective friction coefficient μ and the solids volume concentration Φ can be predicted by the inertial number I, with similar laws being expressed with the modified inertial number I_m [Jop et al., 2006, Amarsid et al., 2017]. Utilizing CG, we have derived bed averaged fields for the stress tensor and concentration, recovering these scaling relationships for monodisperse flows with and without an interstitial fluid phase (Figure 3). We have opted to plot data using the dry inertial number I, rather than using I_m, for reasons outlined in Appendix A.2.

In Figure 3a, we observe regimes in $\mu(I)$ space that have been observed by previous efforts [MiDi, 2004, Cruz et al., 2005, Forterre and Pouliquen, 2008, DeGiuli

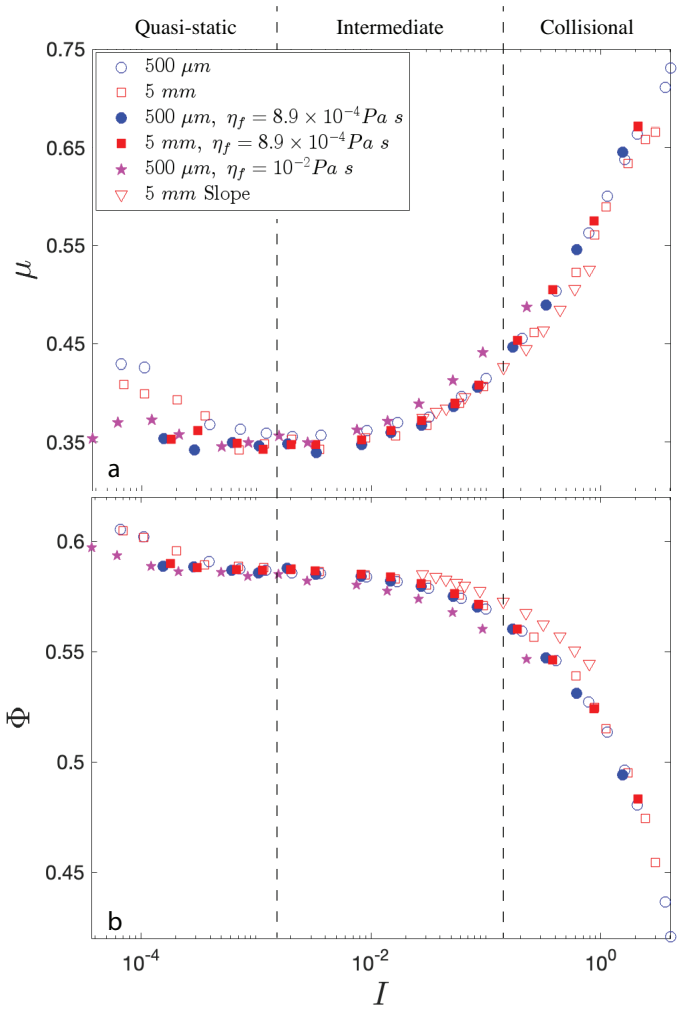

Figure 3. Granular rheology described by (a) the effective friction coefficient μ and (b) the solids concentration Φ, as a function of inertial number I, derived from coarse-graining discrete data. Vertical dashed lines outline the three regimes detailed in the text.

and Wyart, 2017, Breard et al., 2020, 2024]. First, we identify a velocity-weakening regime when $I < 10^{-3}$. Though inertial numbers in this range are most commonly referred to as the quasi-static regime (e.g., MiDi [2004], Breard et al. [2020]), where μ stays constant with increases in shear rate, we observe behavior that reflects non-monotonic scaling between μ and I. This has been posited to arise from endogenous noise generated in low shear conditions [DeGiuli and Wyart, 2017]. Here, velocity weakening is most prevalent in simulations conducted in the absence of a fluid phase. As non-monotonic $\mu(I)$ scaling may be a special case of granular flows that

are characterized by intermittence (i.e., stick-slip flowing behavior; e.g., Baldassarri et al. [2019]), we have opted to express this regime as concomitant with the quasi-static regime. Moreover, as $I \rightarrow 10^{-3}$, μ reaches a relatively constant value, which is characteristic of the quasi-static regime. Similarly, at this point, the particle concentration maintains a constant value (Figure 3b). Effective friction begins to exhibit rate dependence at inertial numbers between 10^{-3} and 10^{-2}, signifying the transition into what is referred to as the intermediate regime. Here, the flowing bed of grains behave phenomenologically like a liquid; the granular bed is no longer able to support itself under shear loads, resulting in continuous deformation under shear. In the intermediate regime, particles remain in prolonged contact with one another, forming an evolving contact (force-chain) network that rotates, breaks, and reforms itself in time [Majmudar and Behringer, 2005, Forterre and Pouliquen, 2008]. In this regime, the particle concentration begins to display dilatancy, or decreases in particle concentration with increasing shear rate (Figure 3b). Finally, in the limit when $I > 10^{-1}$, the flow enters into the collisional regime (also known as the inertial regime). In this limit, the bed dilates rapidly, prolonged contacts are reduced, and binary particle collisons become the primary mechanism for momentum transfer [MiDi, 2004, Cruz et al., 2005, Forterre and Pouliquen, 2008].

In conjunction with the ratio of stresses (μ) and concentration (Φ), we can help classify the internal structure of our flows using granular temperature. Figure 4 depicts non-dimensional isotropic granular temperature Θ ($\Theta = \rho_s T P_s^{-1}$) as a function of I, coarse-grained as a bed-averaged quantity (Θ) and wall-averaged (Θ_w)—taking the average granular temperature of all particles in contact with the force plate (Figures 4a and 4b, respectively). Both measures of granular temperature display near-linear log-log scaling with I, with data points collapsing to a single curve, showing that this relationship is independent of particle size, the presence of a liquid phase, and changes in flow configuration. This suggests that the fluctuating kinetic energy of particles at the base of the flow, those transferring flow energy to the force plate, can be described by the total bed averaged inertial state I (Figure 4b).

Granular temperature is commonly assumed to be isotropic in many approaches that utilize kinetic theory applied to rapid granular flows (e.g., Johnson and Jackson [1987], Syamlal et al. [1993], Berzi et al. [2020]. Nevertheless, the anisotropic nature of granular temperature has been acknowledged rather early in the history

of granular kinetic theory (e.g., Campbell [1989]). To show this, we plot the ratio of the stream-wise granular temperature to the component normal to the bottom plate (Figure 4c). The degree of granular temperature anisotropy gives insight into how momentum is communicated and advected through the system, with isotropic quantities corresponding to fluctuations that arise due to particle contacts, and anisotropy in the stream-wise direction resulting from particle motion normal to shear, likely driven by particle-particle collisions and deflections [Campbell, 2006]. In general terms, when $I < 10^{-3}$, granular temperature is anisotropic in the y-direction (normal to the bottom plate); as $I \rightarrow 10^{-1}$, the stream-wise component begins to exceed the vertical component (Figure 4c). Note that the viscosity of the interstitial fluid phase plays a large role in this behavior; for example, simulations conducted in a viscous fluid show that the stream-wise component increases to over 20% of the y-normal component when $I \approx 0.1$, where the water submerged and dry flows experience a similar increase when $I \approx 0.8$ and $I \approx 1$, respectively. The directionality of granular temperature seems to be related to the regimes described by μ and Φ in Figure 3: anisotropy in the y-direction correlates with quasi-static regime when $I < 10^{-3}$ and μ decreases with increasing shear rates, isotropy occurs primarily in the quasi-static and intermediate regimes, and granular temperature becomes anisotropic in the stream-wise direction as flows dilate and approach the collisional inertial regime.

Figures 3 and 4 show that granular flow rheology and internal energy fluctuations, averaged over the entire flow and at the force plate, scale with a macroscopic description of flow inertial state. We can continue to explore the relationship between averaged flow states and basal interactions by examining the effective friction coefficient at the force plate, or effective wall friction, μ_w (Figure 5). μ_w scales very similarly to the bed-averaged friction coefficient, but with much more spread: the general trend of friction decreasing at low inertial states, transitioning to a relatively constant value, then increasing with increases in I, is maintained. Nevertheless, there is much more spread amongst the simulations, showing that changing the flow configuration, and including the presence of an interstitial fluid, causes deviations away from a universal $mu_w(I)$ scaling. Kim and Kamrin [2020] suggest that the friction coefficient rescaled by non-dimensional granular temperature Θ helps collapse variability across flow configurations. Following this, Fig 5b depicts their suggested scaling, but we instead use quantities defined at the force plate. This shows that

variability in the ratio of wall stresses, tracked by the flow-averaged inertial number, is effectively balanced by energy fluctuations at the bottom boundary.

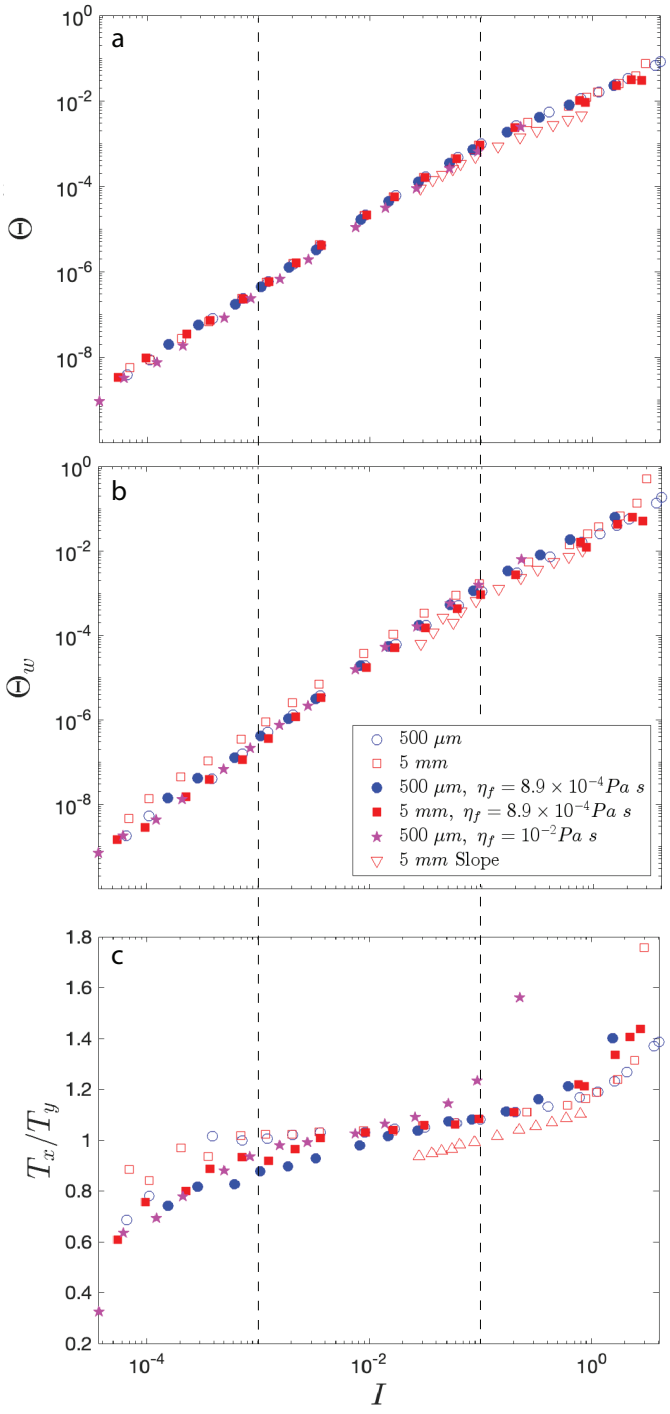

Figure 4. (a) Flow-averaged—coarse-grained—non-dimensional granular temperature Θ, (b) wall-averaged non-dimensional granular temperature at the force plate, and (c) the ratio of stream-wise and span-wise flow-averaged granular temperature as a function of inertial number I. Vertical dashed lines show the three inertial regimes: quasi-static $I < 10^{-3}$, intermediate $10^{-3} < I < 10^{-1}$, and collisional $I > 10^{-1}$.

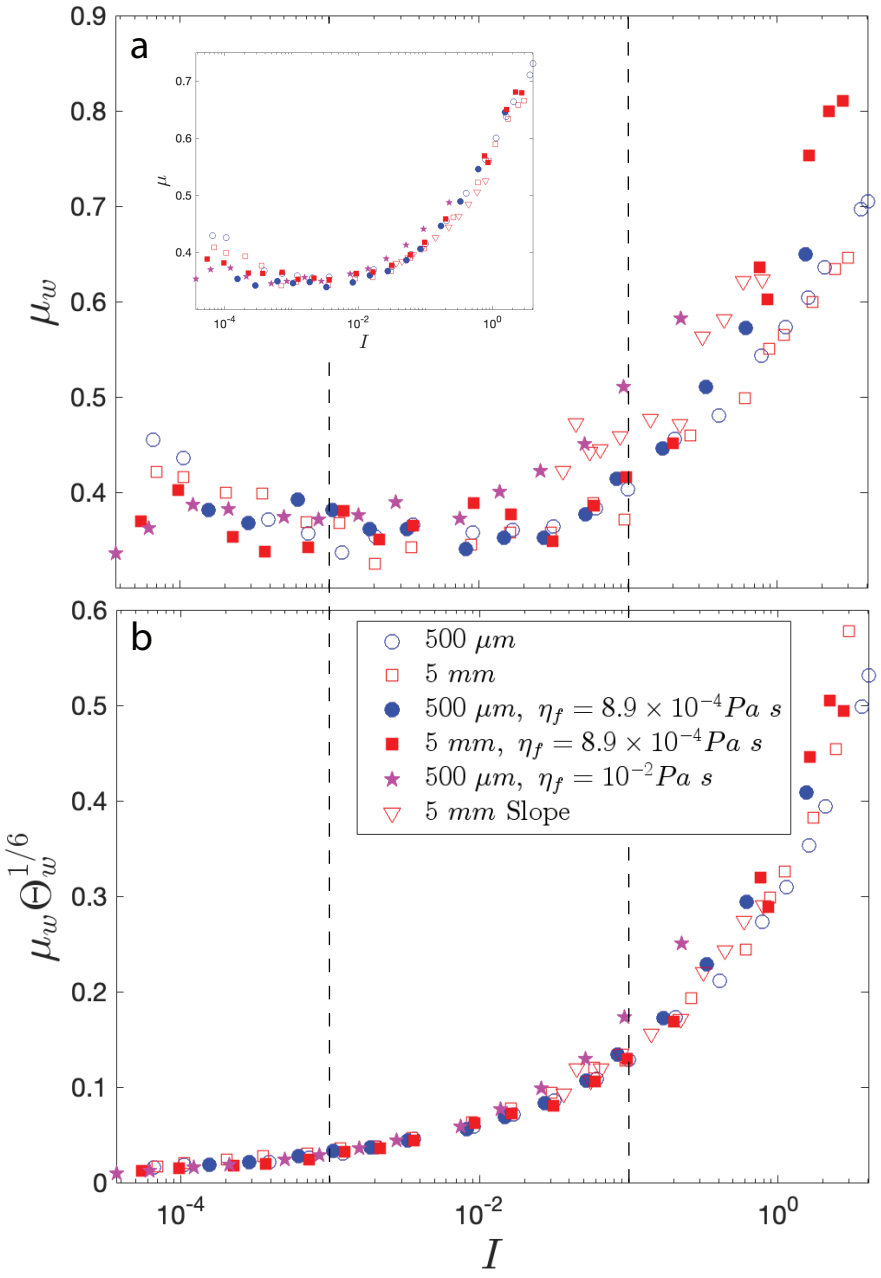

Figure 5. (a) Wall-averaged (bottom boundary flow-plate interface) effective friction coefficient μ_w, with inset showing the bed-averaged friction coefficient and (b) wall-averged friction coefficient scaled by the wall-averaged non-dimensional granular temperature Θ_w, proposed by Kim and Kamrin [2020], as a function of inertial number I. Vertical dashed lines demarcate the quasi-static, intermediate, and collisional inertial regimes

2.3.2 Wall forces

Wall forces (or basal stresses) are how geophysical mass flows effectively communicate flow momentum to the earth. Encoded in this exchange is an energy cascade that converts flow driving energy to shear work. This work is ultimately dissipated through particle-particle and particle-boundary interactions, as well as frictional heating [Iverson, 1997]. To this end, we will examine how simulated wall forces—or basal forces exerted by the flow on to the rough and static bottom plate—fluctuate, using the power spectral density (PSD) of the basal forcing time series. These spectra will be used to relate the power of these fluctuations back to macroscopic rheologic behavior observed in Section 3.3.1.

Figure 6a-c show the root-mean-square PSDs derived from the sum of wall forces measured by the force plate for dry simulations containing 500 μm particles, 5 mm particles, and simulations with 500 μm particles submerged in a viscous fluid (Figures 6a, 6b and 6c, respectively), with each spectrum colored by coarse-grained inertial number I. As I increases, the PSD for all simulations begins to lift, transitioning from a relatively constant linear decrease in power with frequency at low inertial states, to a near-flat response, up to a corner frequency, when $I \sim 1$. PSDs have been scaled to account for changes in the size of the simulated-flow configuration and the subsequent effect on the absolute quantities measured in the PSD. We scale by the plate area, using the common assumption that basal forces are random and uncorrelated, such that the amplitude spectra of these forces will scale with the square root of the number of forcing locations (e.g., Tsai et al. [2012], Farin et al. [2019], Allstadt et al. [2020]). Nevertheless, we must note that the assumption of uncorrelated forcing breaks down in inertial states where $I < 10^{-1}$, when forces are correlated in space, and definite length scales are intrinsically related to flow rheology [Lois et al., 2007, Ge et al., 2024].

Figures 6d and 6e show the mean frequency $\bar{f}$ of each simulation, and the mean frequency scaled by the particle deformation timescale τ_p, a function of particle size, density, and normal elastic coefficient:

$$\tau_p = \left(\frac{d}{\sqrt{k_n / \rho_s d}} \right) \tag{2.24}$$

Figure 6d shows that the mean frequency is a monotonic increasing function of I, ranging from less than 10^{-3} Hz to slightly greater than 10^{3} Hz, depending on particle size. This reflects the fact that the character of the PSDs change with inertial number:

as I increases, more power is relegated to higher frequencies, causing the spectra to lift from the log-log linear decay (Figure 6a-c). The particle size dependence in $\bar{f}$ is completely captured by τ_p thus, implicitly, particle scale properties such as particle size and and elastic coefficient k_n (Figure 6e). Meaning as particle size decreases by an order of magnitude, the mean frequency measured at a given inertial number will increase by an order of magnitude. This results in the PSDs of the 500 μm flows being shifted to the right in power-frequency space relative to the 5 mm flows (Figures 6a and 6b). This behavior is similarly exhibited in Figure 6f where the corner frequency f_c (defined as the frequency at which the signal has dropped below 50% of the mean power) is shown as a function of inertial number. At low inertial numbers ($10^{-4} < I < 10^{-2}$) the corner frequency f_c of each configuration seems to be dictated by particle size (i.e., f_c values differ by an order of magnitude when the particle size changes by an order of magnitude). Nevertheless, as I increases, the two curves that were once dictated by particle size meet just as $I > 10^{-1}$, meaning that once the flows enter into the collisional regime, the corner frequency is controlled solely by the inertial state of the flow (Figure 6f). Note that the concavity of the curves shown in Figures 6d-f change as the inertial number approaches, and becomes greater than, 10^{-2}, providing evidence that changes in flow regime, as the flow enters into the intermediate inertial state, is effectively captured in forces recorded by our numerical force plate.

This study is in part motivated by the ability of granular flows to radiate elastic energy that can be observed in real-time in the form of seismic signals (see Allstadt et al., 2018 for a review on signals used to observe geophysical mass flows). A static forcing will not generate an observable signal (i.e., if one merely stands still next to a seismometer, no ground movement will be recorded). Therefore, we are concerned with the basal (wall) force fluctuations in-time. To this end, we plot the non-dimensional integral of the simulated PSDs Λ—as defined in Eq. (3.13)—allowing a glimpse at how the variance in the bed-force time series (measured by the PSD), and the binning of power in frequency space, changes with changes in inertial state (Figure 7a-c). Eq. (3.13) is defined as the integral over the PSD, and in Figures 7(a-c) we show the effect the lower bounds of integration has on Λ (always excluding the zero-frequency mean): Fig 7a shows Λ_1, the integral from 1 Hz to f_{ny}; Fig 7b shows Λ_2, the integral from 10 Hz to f_{ny}; and finally, Fig 7c shows Λ as function of I, with the integral having variable lower bounds of integration that is dictated

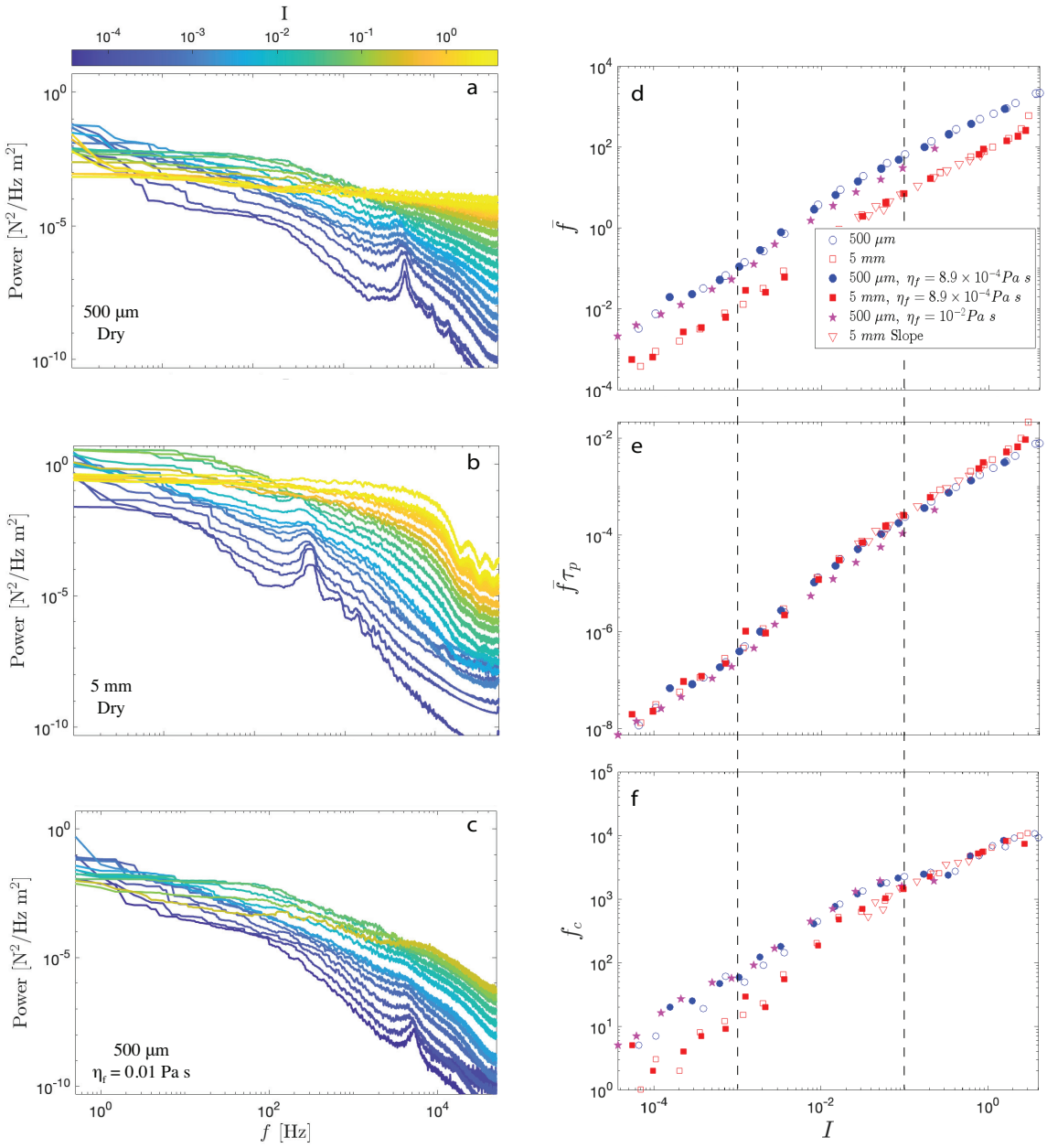

Figure 6. (a-c) RMS basal-force power spectral densities (colored by inertial number) for dry simulations with 500 μm (a) and 5 mm particles (b), and simulations with an interstitial viscous fluid with 500 μm particles (c).The right column depicts (d) mean frequency $\bar{f}$ in Hz of the forcing spectra, (e) $\bar{f}$ rescaled by the particle response timescale τ_p , and (f) corner frequency f_c as a function inertial number I. Veritical dashed line in (d-f) depict the three inertial regimes: quasi-static, intermediate, and collisional.

by the particle size: 10 Hz for simulations using 500 μm particles and 1 Hz for simulations using 5 mm particles. Figure 7d depicts this choice in Λ (i.e., lower bounds of integration dictated by particle size), as a function of the solid volume concentration Φ. We have chosen to use this definition of Λ as Figure 6 shows that, at equivalent inertial states, the relative binning of power in frequency space is shifted by an order of magnitude when the particle size changes by an order of magnitude. Thus, as we are concerned with how basal forces record bulk rheology, rather than effects that are dictated by particle size, we have opted to change the lower bounds of integration based on particle size to reflect the relative decrease in high frequency energy when particle size increases. Here, we are establishing a theoretical framework for what flow information can be effectively encoded in basal forcing signals, future work is needed to examine how this can be generalized to polydipserse flows.

Regardless of the bounds of integration, and when the zero frequency mean is excluded from the integral, the character of the Λ vs I curves remain the same: under plane-shear conditions, spread in Λ lessens as I approaches and becomes greater than 10^{-2}, or as flows are well within the intermediate regime described in Section 3.3.1. This scaling persists up until the threshold of the inertial collisional regime, where $I \sim 10^{-1}$. Here, Λ briefly shifts from an monotonic increasing function of I, and decreases with I, until finally increasing again as a log-log linear function as $I > 10^{-1}$. Previous work has observed a similar correlation between the integral of the PSD and an inertial number estimate [Arran et al., 2021]. Here we extend this view to a much larger range of inertial states, analyzing this over a wider frequency band and comparing it against an inertial number that is estimated via our coarse-grained stress tensor. Further, we observe that Λ is a strong function of solid concentration Φ, with a shift in scaling behavior when $\Phi = \Phi_c \approx 0.57$ (Figure 7e). A related correlation has been observed in transient flume experiments utilizing sediment-water mixtures [Piantini et al., 2023]. Importantly, Figure 7e shows a strong functional connection between basal forcing and flow concentration, an important parameter for unifying non-local and local rheologies observed in disparate granular systems [Breard et al., 2024].

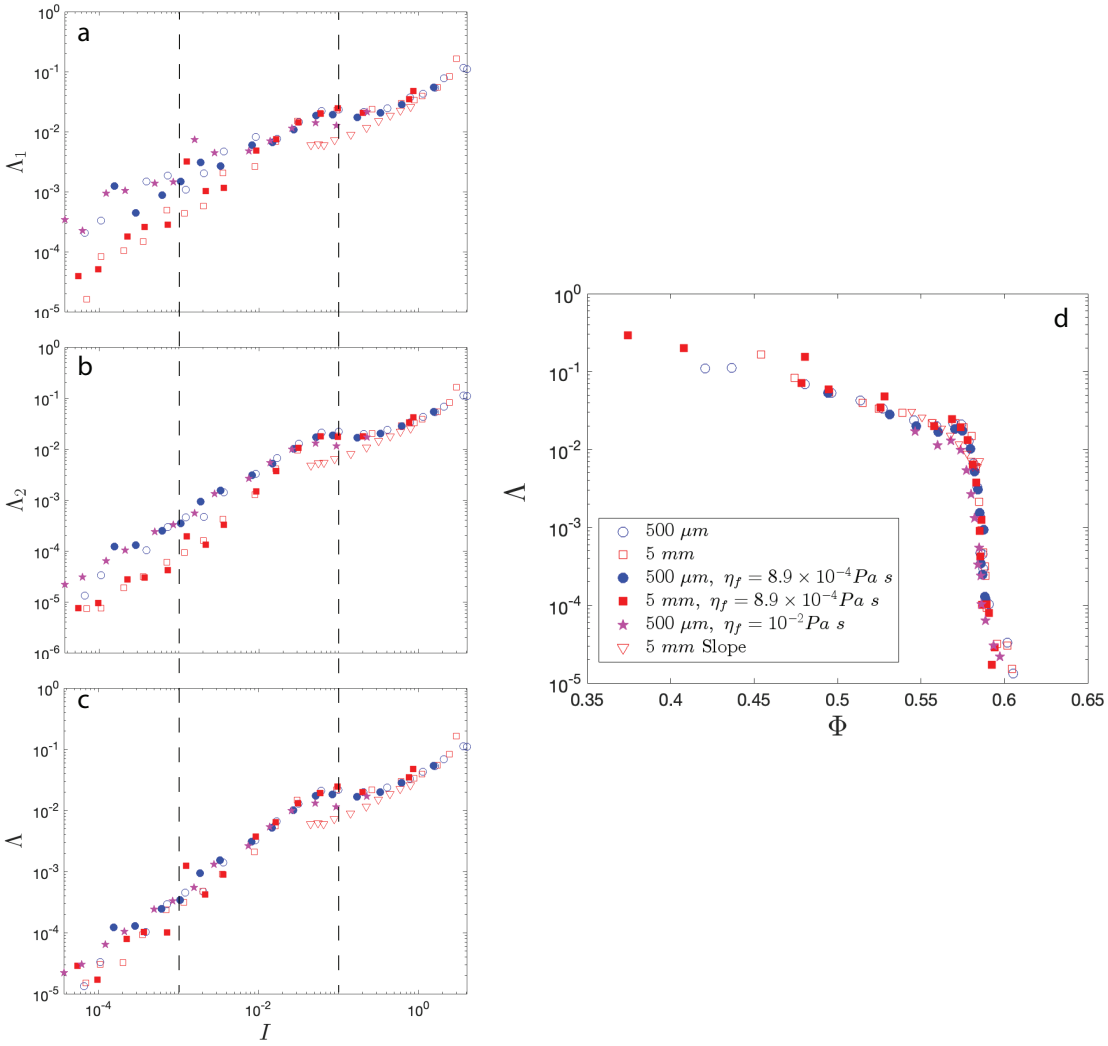

Figure 7. (a-c) Non-dimensional forcing fluctuations Λ as a function of inertial number I, with vertical dashed lines inertial regimes, and (d) as a function of particle concentration Φ. (a-c) show the effect of changing the bounds of integration in Eq. (3.13): Λ_1 an integral with the lower bound being 1 Hz and the the upper being f_{ny} (a), Λ_2 with a lower bound being 10 Hz and the upper being f_{ny} (b), and Λ showing the integral with variable lower bounds dictated by particle size, 1 Hz for 5 mm particles and 10 Hz for 500 μm particles (c). (d) Depicts Λ (variable lower bounds, c) as a function solid particle fraction Φ, with critical shift in scaling occurring at $\Phi_c \approx 0.57$

2.4 Discussion

Geophysical surface flows are complex phenomena that pose challenges to life and property. Near-field and along-channel seismometers provide indirect data related to these events, having potential use as early warning devices and flow monitors. Nevertheless, inverting seismic signals generated by surface mass flows is made difficult by site specificity, and a lack of an observational framework that relates basal forces to bulk flow properties. While phenomena such as debris flows, lahars, and pyroclastic density currents are highly complex and differ greatly in phenomelogical expression, they share an underlying nature of multiphase, in the case of non-negligible fluid-drag, granular mixtures [Iverson, 1997, Delannay et al., 2017, Lube et al., 2020]. While the simulations produced in this study are highly idealized monodisperse flows, composed of perfect spheres in simple-shear and inclined-slope configurations that have attained steady state, we believe these simulations capture the first order effects of granular-stresses exerted onto the boundary. In this way, we seek to relate the rich granular rheology described by, e.g., MiDi [2004], Cruz et al. [2005], Forterre and Pouliquen [2008], and Boyer et al. [2011] to basal tractions generated by geophysical granular flows. Our data suggests that bulk flow properties, such as inertial state, can effectively be encoded in forces transmitted to the boundaries. Further, a phase space defined by the integral of basal forcing power spectra and inertial number demarcates four regimes that hold a relation to flow regimes describing the states of granular matter described in Section 3.3.1. This relationship may be leveraged to model basal forces via a sub-grid parameterization that can be used in models that simulate flows on real-world scales, but whose resolution precludes them from directly capturing granular flow-boundary stresses. Future efforts can continue to paint a fuller picture of bulk flow rheology and basal forces, diverging from the ideal explored here, and considering broader particle size distributions, dilute particle concentrations, and non-spherical particles.

Below, we will begin our discussion by considering granular temperature as a measure of internal fluctuating kinetic energy, originating from shear-work and flow driving forces. We will examine how granular temperature changes across inertial space, as well as how it is affected by flow configuration. We will then consider how these changes are related to particle-scale contacts, ultimately leading to the emergent flow-scale evolution of continuous fields describing our flows. This will allow us to

link observations of bulk granular rheology described in Section 3.3.1 to basal forcing spectra described in Section 2.3.2.

2.4.1 Fluctuating energy generated through shear work, and enhancement of anisotropy through fluid-solid coupling

Granular temperature is a measure of velocity fluctuations that has been used widely through the development of granular kinetic theory. This temperature is traditionally used to infer pressure, shear stresses, and viscosity in high-energy, dilute systems [Lun et al., 1984, Johnson and Jackson, 1987]. Granular temperature may play an important role governing the runout of natural granular flows [Campbell, 1989]. For example, granular temperature is observed to concentrate in dilute regions below dense cores of high speed unidirectional flows, reducing the effective basal friction with increasing mass [Brodu et al., 2015]. Granular temperature, when thought of as the fluctuating energy of a particle, is an integral part of the energy cascade inherent to granular flows as dissipative systems. In this cascade, flow driving energy is converted into macroscopic kinetic energy, as described by the mean velocity, which in turn drives velocity fluctuations of individual grains. These velocity fluctuations lead to dissipative interactions, closing the cascade of energy loss to irrecoverable particle deformation and frictional heating [Campbell, 2006]. Here, we report granular temperature as derived from the coarse-grained kinetic stress tensor, a continuous field originating from the direct measure of discrete particle velocity fluctuations.

In these simulations, granular temperature is produced through shear work and particle-particle interactions—rather than boundary layer effects resulting in wake structures contributing to kinetic energy fluctuations [Mehrabadi et al., 2015]. Figures 4a,b show that, when treated as an isotropic quantity, even when fluid drag outpaces particle inertia, i.e., when $St < 1$ (Figure A.32), non-dimensional granular temperature Θ is well parameterized by the dry inertial number I. This view changes in light of Figure 4c, which shows that the degree of anisotropy varies with I and interstitial fluid composition. Anisotropy in granular temperature has in the past been related as a measure of anisotropy in the transmission of momentum, as well as the mode of granular temperature production, i.e., through particle-particle interactions or shear work and advection through velocity gradients [Campbell, 2006]. From the previously defined intermediate regime up to the collisional inertial limit (or when $10^{-3} < I < 10^{-1}$), macroscopically defined granular temperature is roughly isotropic,

suggesting that this variable is maintained through particle-particle interactions, leading to an equal partitioning of fluctuating energy in three dimensions. As $I \rightarrow 10^{-1}$, granular temperature becomes anisotropic in the x direction, suggesting that temperature production becomes dominated by velocity fluctuations arising from particles advecting/deflecting normal to the velocity gradient. As shear induced velocity gradients develop, random particle motion normal to the gradient can enhance the generation of granular temperature; this is known as the streaming effect [Campbell, 2006]. The streaming effect causes granular temperature to be anisotropic in the shearing direction. Since viscous forces contribute to particle-shearing, the inertial number at which this anisotropy occurs is a function of the presence of, and viscosity of, the interstitial liquid. Note that the dry granular simulations are lacking these viscous shear contributions, therefore simulations involving a liquid phase reach anisotropic conditions at lower inertial numbers, compared to the simulations without a liquid phase (Figure 4c). At the low inertial number limit, when $I < 10^{-3}$, granular temperature is anisotropic in the direction normal to the bottom boundary. This occurs when the effective friction coefficient μ and particle concentration Φ decrease with I (Figure 3). With this in mind, anisotropy at these low inertial numbers can be linked to particle reorganization; particles mount those that reside in layers lower and adjacent to them, sliding and falling back down under the force of the top plate's confining pressure [DeGiuli and Wyart, 2017]. Moreover, bed spanning force chains in this low inertial number regime are long lived, but susceptible to buckling events, causing motion normal to the shearing plane during slip events [Tordesillas et al., 2011]. Individual contact forces further reflect this directional dependence on inertial number (Figure A.36).

The differences in the two modes of granular temperature production (particle-particle interactions or shear induced 'heating') can also be indicated through the relationship between granular temperature and inertial number. Figure 4 shows a direct relationship between inertial number and granular temperature rescaled by the solids pressure and the particle density. Rescaling is required for all of the simulations to collapse to a master curve. The relationship between granular temperature and inertial number is sensitive to the solids pressure and density. Thus, the absolute value of granular temperature is a function of flow configuration: the inclined-slope flow simulations reach granular temperatures nearly an order of magnitude less than that of a shear-cell simulation at an equivalent inertial number (Figure A.37). We relate

this decrease to the fact that the inclined-slope simulations do not experience the same magnitude of shear, suggesting that the solids pressure corrects for the lack of shear work provided to generate granular temperature. This is similar to the effect produced by rescaling the coarse-grained shear rate by the timescale of particle rearrangement, thus giving equivalent inertial numbers across flow configurations. Non-dimensional granular temperature can help provide a link across not only various flow geometries [Kim and Kamrin, 2020] but granular matter under disparate confining pressures. This is important for evaluating bed forces as solids pressures may vary significantly in natural flows interacting with complex topography [Benage et al., 2016].

2.4.2 Basal forces record granular phase transitions

Previous laboratory experiments have constrained a correlation between I and an estimate of the variance in basal forces (Λ) for inclined plane flows at high inertial numbers (i.e., $I > 10^{-1}$; Arran et al. [2021]). Here, we expand this by performing analysis that probes a wider range of inertial states, with I spanning from $10^{-4} - 10^{0}$. With this expansion, we are able to demarcate distinct flow regimes by correlating changes in Λ with macroscopic quantities derived from coarse-graining procedures. Figure 7 shows that there are distinct changes in the nature of how Λ scales with inertial number, most notably, as the flow transitions from the intermediate, liquid-like flow regime, to the collisional gas-like flow regime. To the author's knowledge, this is a newly discovered regime that expresses itself in the transmission of flow driving forces into boundary stresses. Therefore, we will describe this regime in detail before considering the relationship between Λ and I in the three other previously defined flow regimes (i.e., the quasi-static, intermediate, and collisional regimes).

In the shear-cell simulations, as $I \rightarrow 10^{-1}$, Λ ceases its near constant increase with I, plateauing then dropping slightly just as $I > 10^{-1}$ (Figure 7c). This is, to an extent, mirrored by the inclined-slope simulations: Λ stays relatively constant with increasing shear rates when $10^{-2} < I < 10^{-1}$, then recovers the scaling behavior observed by the shear-cell simulations. This shift is corroborated in Figure 7d which depicts a critical value of solid concentration $\Phi_c \approx 0.57$ above which Λ decreases rapidly from a local minimum. At concentrations greater than Φ_c, the packing fraction (or concentration of solid particles) begins to inhibit strain [Zhang and Kamrin, 2017]. This is analogous to a critical volume fraction that defines a glass-like transition in which the kinetic properties of a liquid are diminished as the liquid is undercooled and avoids crystallization [Cohen and Turnbull, 1959]. Moreover, a similar critical

value of Φ is observed in dense suspensions, below which the rheology of the system is controlled by the Stokes number of the solids phase, and above which is a contact dominated regime that is rate-independent up to a critical shear rate [Ness and Sun, 2015].

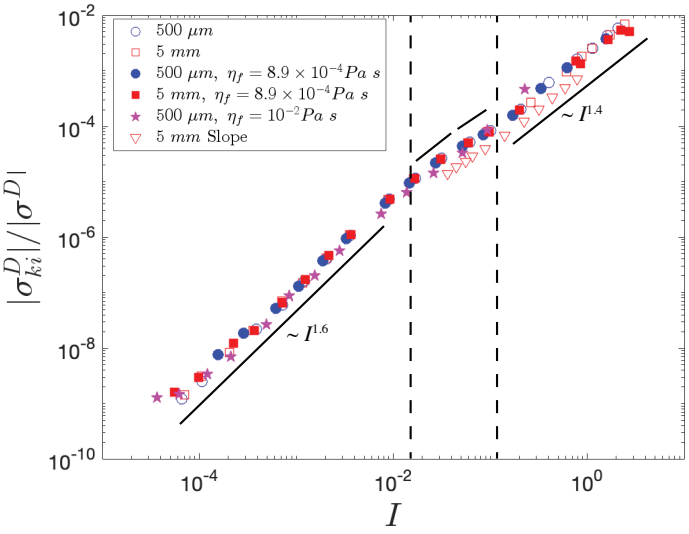

Figure 8. Ratio of the magnitude of deviatoric kinetic stress to the magnitude of total deviatoric stress ($\sigma^D = \sigma^D_c + \sigma^D_{ki}$, where σ^D_c is the deviatoric contact stress and σ^D_k is the deviatoric kinetic stresses) as a function of inertial number I. Vertical dashed lines demarcate when the concavity of the scaling relationship changes, transitioning from a log-log linear scaling that goes as $I^{1.6}$ (solid line from $10^{-4} < I < 10^{-2}$) to $I^{1.4}$ (solid line from $10^{-1} < I < 10^{0}$).

The plateau in Λ that occurs at this glass-like transition (i.e. when $10^{-2} < I < 10^{-1}$ and $\Phi(I) \to \Phi_c$; Figures 7d,e) is accompanied by a decrease in the rate of change in the ratio of the magnitude of the deviatoric kinetic and total stresses (σ^D_{ki} and σ^D, respectively; Figure 8). As $I > 10^{-2}$, $|\sigma^D_{ki}|/|\sigma^D|$ becomes concave, suggesting a decrease in the rate at which kinetic stresses balance out shear-work with increasing I. This is reflected in the exponent to which the ratio scales with inertial number: when $I < 10^{-2}$, the ratio scales linearly in log-log space as $I^{1.6}$, when $I > 10^{-1}$ the ratio scales as $I^{1.4}$ (Figure 8). In the state where $10^{-2} < I < 10^{-1}$, the internal contact network is significantly altered, and the granular bed begins to dilate (Figure 3b). As this happens, the density and length of force chains decrease at the highest observable rate (Figure 9). When $I < 10^{-1}$, force chains with magnitudes greater than two times the granular bed's weight propagate through the entirety of the domain

(Fig 9a). When $I \sim 10^{-1}$, contact forces are still correlated in space, but they are not as abundant (Fig 9b). This behaviour can be further evidenced by the decrease in the average coordination number $\bar{Z}$, or the average number of neighbor-contacts a single particle has, as a function of I (Figure 9b, inset). Thus, we suggest that shear work is consumed by the process of bed dilation, destroying aspects of the force-chain network during the 'phase' transition from a contact dominated liquid-like granular phase, to a collisional gas-like flow (or, in other terms, as the flow transitions from the intermediate regime to the collisional regime). This process effectively inserts itself into the dissipative cascade of flow driving energy being converted into particle-scale energy fluctuations, which will ultimately be dissipated through irrecoverable deformation, frictional heating, and acoustic emissions [Siman-Tov and Brodsky, 2021].

Figure 10 summarizes our data with an annotated $\Lambda(I)$ phase space (from Figure 7c). With this we can observe how changes in $\Lambda(I)$ are accompanied with transitions in and out of granular flow regimes. The first regime is defined when $I < 10^{-3}$, aligning with the quasi-static regime that is described in the literature, and is characterized by many high magnitude, domain spanning, force chains (Figure 10a). Rheologically, this regime is concomitant with a decrease in apparent friction coefficient with increasing shear rates, both as a bed-averaged coarse-grained quantity and at the wall (Figures 3a and 5a, respectively). This decrease in the ratio of stresses is also accompanied by a slight decrease in particle concentration (Figure 3b) and has been observed elsewhere, being attributed to endogenous vibrations coaxing particles to slip as they are near failure [DeGiuli and Wyart, 2017]. This is supported by the fact that granular temperature is dominant in the vertical direction (Figure 4c), thus individual particle motion, 'noise', works to dilate the bed of grains, decreasing the number of particles in static contact. This likely works in tandem with top plate motion stretching and rotating the long-lived force chains in the system, causing them to buckle and the bed to dilate [Tordesillas et al., 2011]. We suggest that basal forces in this regime represent the diffusion of reordering events down to the base of the domain as shear-stresses generated by the top plate drive intermittent slip events [Cruz et al., 2005]. $\Lambda(I)$ scaling in this regime shows higher degrees of dispersion about a general increasing log-linear trend, with an apparent particle size dependency. This shows that, in this framework, there remains particle scale effects that are due to the sensitivity of our results to spectral resolution: the mean frequency

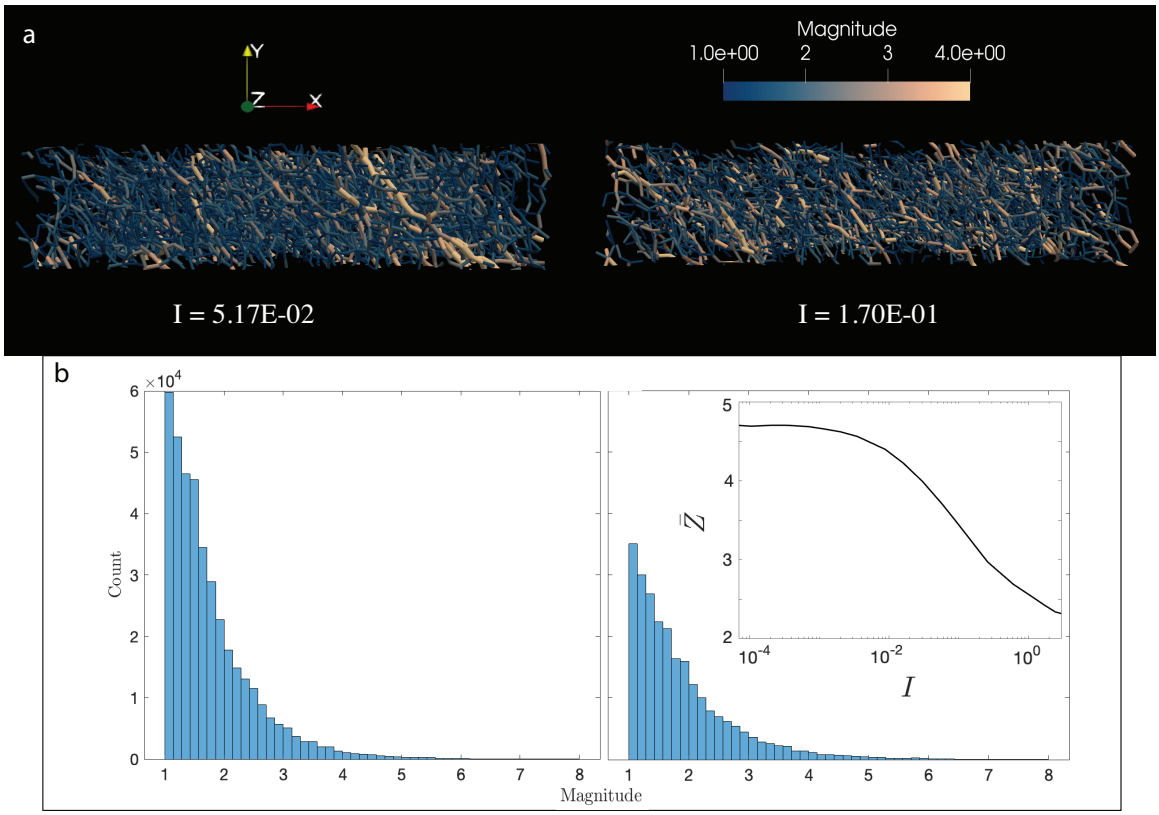

Figure 9. (a) Visualization of force chains whose magnitude is non-dimensionalized by the average contact force for shear-cell simulations with $I \sim 10^{-2}$ (left) and $I \sim 10^{-1}$ (right). Here, each contacting pair of particles is represented by a tube whose color and radius is scaled by the contact force normalized by the bed's weight. (b) Histograms of contact forces showing number of contacts binned via the non-dimensional magnitude. Inset: Time averaged coordination number $\bar{Z}$ as a function of I.

of the bed forcing signal is a function of I (Figure 6d), thus more energy is binned in lower frequencies with decreasing I. The lowest resolvable frequency is dictated by the length of the time-series N and the sampling frequency f_s ($\Delta f = f_s/N$), these do not change across simulations and particle size ($f_s = 100$ kHz and $N = 100000$). Thus, in this regime, particle size has a control on the frequency bands basal forcing power is relegated to, matching the fact that low inertial numbers signify when the time scale for particle rearrangements (function of particle size and confining pressure) dominates the kinematics of the system [MiDi, 2004].

The second regime is characterized by $10^{-3} < I < 10^{-2}$ (Figure 10b). Here, the bed of grains is characterized by continuous deformation and aligns with the

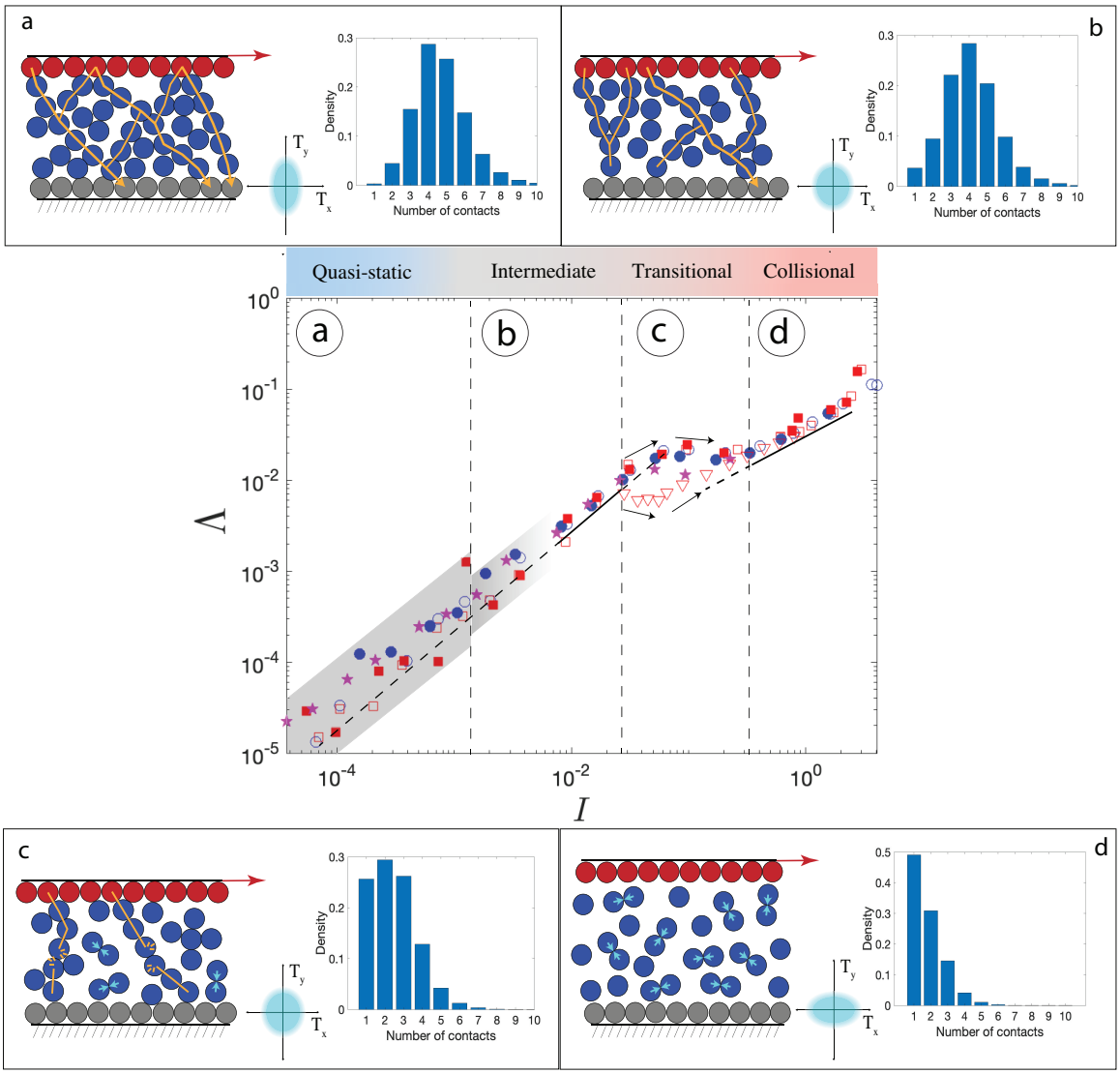

Figure 10. Annotated Figure 7d, highlighting four regimes spanned by Λ, with bar charts showing the probability density of the number of particle contacts, and an axis representing the x and y components of granular temperature, where the cyan field qualitatively depicts the degree of anisotropy in that regime. Vertical dashed lines show regimes that are resolved by basal forces. (a) Force-chain dominated regime where $\Lambda \sim I$. High magnitude domain spanning force chains cage particles; unsteady particle fluctuations, predominantly in the y-direction, disrupt the otherwise static architecture, weakening μ. (b) Intermediate regime where linear log-log scaling persists and strengthens to the point of data collapse as bed deformation becomes continuous. (c) Transitional regime analogous to a latent heat-energy required to break force chains. (d) Collisional regime where binary particle collisions are the dominant mode of particle-particle and particle-wall interactions.

aforementioned intermediate regime. In this regime, basal forcing is less controlled by particle scale parameters, but instead by the global kinematics of the system represented by the inertial number: linear log-log scaling persists, and is accompanied by the collapse of data points from disparate particle size simulations onto a single curve. Therefore, less scatter in the log-log linear $\Lambda(I)$ scaling marks the transition from quasi-static behaviour to continuous deformation of particles that remain in prolonged contact with one another. This is supported by the development of isotropic granular temperature, suggesting that energy fluctuations are controlled by those prolonged particle contacts (Campbell, 2006; Figure 4c).

Increasing shear rates leads to a transitional regime where $10^{-2} < I < 10^{-1}$ (Figure 10c). In past studies, this regime is included within the liquid-like intermediate regime. In this regime, the apparent coefficient of friction increases monotonically (Figure 3a), the particle concentration decreases rapidly (Figure 3b) and granular temperature remains isotropic in the absence of a viscous interstitial fluid (Figure 4c). This aligns with previous definitions of the intermediate inertial regime [Breard et al., 2020, 2024]. Nevertheless, as explained above, the scaling of basal force fluctuations with I diverges from the log-log linear scaling observed elsewhere in the phase space. This transitional regime is reminiscent of latent heat of vaporization required to disrupt inter-molecular forces during the phase change from a liquid to a gas, thus leading to a dual existence interval where both domain spanning force chains and particle collisions contribute to forces recorded by the force plate. This interval exists until flow driving energy starts to become consumed by the dilation of the granular bed with increasing shear-work. Importantly, this regime contains the lowest I values of the free surface inclined-slope flows, and Λ measured in these simulations are displaced from the magnitude of values recorded in the shear-cell configurations, though general trends are maintained.

The last regime spanned by our data reflects the inertial state transitioning into the gas-like collisional regime (Figure 10d). In the limit where $I > 10^{-1}$, basal forces become noise-like, with a near flat spectral response across a wide band of frequencies (Fig 6a-c). Here, granular temperature becomes anisotropic in the stream-wise direction, suggesting the development of kinetic energy fluctuations through collisions and particle movement in the direction of shear-induced velocity gradients (Campbell, 2006; Figure 4e-f). $\Lambda(I)$ scaling shows a collapse across particle sizes and configurations. This change in scaling behavior is mirrored by the scaling of

Λ with Φ: as $\Phi < 0.57$ (exemplary of simulations with $I > 10^{-1}$; Figure 3b) the $\Lambda(\Phi)$ scaling curves kinks, and the rate at which Λ increases with decreasing solid concentration decreases. It is notable that in this regime, Λ measured in the inclined-slope configurations joins the scaling curve of the shear-cell simulations. Thus, this transition suggests that as flow driving energy is used to dilate the flowing grains, preparation effects (or those effects that are configuration-dependent) occurring near the max packing volume fraction (e.g. Josserand et al. [2000]) no longer play a strong role in fluctuating forces recorded at the base of the flow. This hints that structural memory is stored in elastic contacts in the form of the contact structures, and that this memory is erased as the flow enters into the collisional inertial gas-like regime.

2.4.3 Towards real-scaled geophysical flows

Geophysical mass flows can exhibit a wide range of inertial states, solid volume fractions, and can have interstitial fluid viscosities that span orders of magnitude. To visualize this, we sketch a three-dimensional space spanned by inertial number I, solid concentration Φ, and Stokes number St, using typical values for velocity, flow height, particle density, fluid viscosity, solid concentration, and particle size to calculate the non-dimensional parameters (Iverson [1997], Iverson and Denlinger [2001], Roche [2012], Delannay et al. [2017], Breard et al. [2023], Figure 11). Debris flows can span from the intermediate to collisional inertial regime, while having solid particle fractions that are on the order of 0.8-0.2. This reflects the fact that they can display behavior akin to highly frictional concentrated flows or very dilute muddy-water flows. Similarly, pyroclastic density currents can encompass a broad range of particle concentrations, spanning many orders of magnitude, from dusty-gas-like surges to highly concentrated flows that are exemplified by the dense basal undercurrents of pyroclastic density currents. In Figure 11, we have plotted dimensionless values for dense pyroclastic density currents known as pyroclastic flows, acknowledging that if we considered dilute pyroclastic density currents (known as surges), the shaded field representing these endmembers would extend far beyond what is sketched in the figure.

Between debris flows and pyroclastic flows, characteristic particle size can span from $10^{-6} - 1\ m$. Similarly, the viscosity of the interstitial fluid spans many orders of magnitude, with fluid compositions ranging from air (in the case of pyroclastic flows), with a viscosity of $\sim 10^{-5}\ Pa\ s$, to muddy water (in the case of debris flows), which can have a viscosity of $\sim 10^{-1}\ Pa\ s$ [Iverson, 1997, Roche, 2012]. Thus, the

Stokes number St, or the ratio of particle-inertial and fluid stresses, ranges from fluid stress dominated regimes (i.e., $St << 1$), to the end member where particle-inertia outpaces viscous fluid stresses (i.e., $St >> 1$). Though the interstitial fluid viscosity of debris flows can be in excess of 100 times greater than water, typical values for debris flow height, characteristic particle size, and velocity suggest that under many conditions particle inertia overcomes viscous stresses. Conversely, the dilute, fines-enriched, endmembers of pyroclastic flows can exhibit Stokes numbers such that fluid stresses arising from relatively low fluid viscosities can overcome solid particle inertia. Nevertheless, there is much overlap in this three dimensional space between intermediate to dilute debris flows and the highly concentrated endmember of pyroclastic flows. With these disparate phenomena, we have plotted a field representing the values our simulations, showing that our data falls within the debris flow field, and within the field representing the most concentrated pyroclastic flows. With our discrete element simulations, we probe within this space conditions where fluid stresses are significant, while, as the prescribed top-plate velocity increases, conditions reach a point where particle-inertia outweighs fluid stresses, the inertial number increases, and the granular bed dilates, placing our data closer to conditions that align with highly inertial debris flows and concentrated pyroclastic flows.

Figure 11 shows that our simulations achieve conditions that align with real-world flow conditions described by their typical inertial numbers, particle concentrations, and Stokes numbers. With the basal force data derived from these simulations, we can provide a first-order look into how basal-forcing power is binned in frequency space for an idealized flow on the scale of real-world flows. Here we examine a flow that develops from a pile of grains that exhibits solid-like properties, to a highly energetic continuous-flowing medium that is characterized by binary, gas-like, particle collisions. To do this, we will consider a hypothetical system with a footprint of 4 m^2. We will leverage the theoretical assumption that particle forces exerted onto the numerical force plate are uncorrelated. This assumption implies individual particle forces occur randomly, such that the shape of the forcing spectrum does not depend on the sum-total of individual particle forces, while the amplitude scales linearly with the square-root of the number of total forces [Tsai et al., 2012]. Thus, we can scale our observed PSDs to the scale of geophysical flows via:

$$P_{sc}(f) = \frac{A_p}{A_0} P(f) \tag{2.25}$$

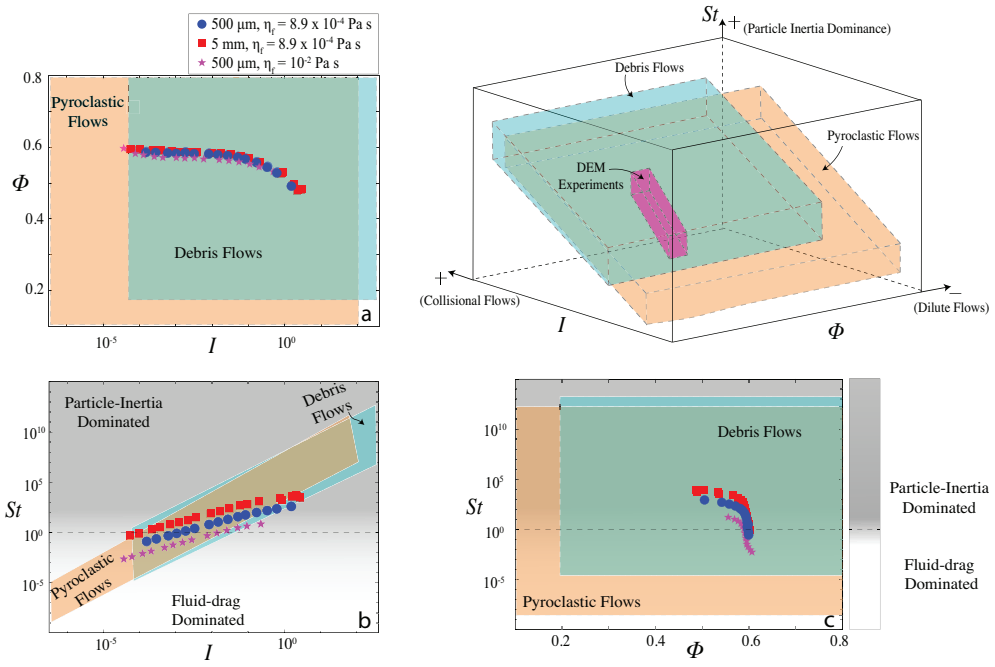

Figure 11. Inertial number I, solid particle concentration Φ, and Stokes number St space. Shaded fields represent typical values for debris flows and pyroclastic flows, taken from Iverson [1997], Iverson and Denlinger [2001], Roche [2012], Delannay et al. [2017], Breard et al. [2023], as well as data from discrete element method (DEM) simulations reported here. (a-c) Display 2-D phase spaces within this three-dimensional system.

where $P_{sc}(f)$ is the scaled PSD, A_p is the area of our hypothetical force plate (4 m^2) and A_0 is the original area of the numerical force plate (we use the 5 mm shear-cell simulations, therefore $A_0 = (40d)^2 = 0.04\ m^2$). We note that the assumption of uncorrelated forcings breaks down in flows that span inertial states from $10^{-4} < I < 10^{-1}$, or where we observe long-range forces correlated in space (e.g., Figure 9). Nevertheless, Figure 12a shows that the effect of decreasing a force plate's footprint has on the mean frequency $\bar{f}$ can be captured by scaling $\bar{f}$ by the area over which individual particle forces are summed (i.e., the force plate's area). Similarly, Figure 12b shows the RMS of PSDs measured during a 5 mm shear-cell simulation (where $I \approx 10^{-2}$); when scaled by the numerical force plate area the general shape of the power spectrum does not change, though there are plate length-scale effect in frequencies less than 10^3 Hz (these scale effects are absent when $I > 10^{-1}$, Figure A.38).

Using these scaled PSDs, we depict a spectrogram derived from our 5 mm steady-state dry shear-cell simulations (Figure 12). Note that this spectrogram is a stacking of 20 steady-state simulations, and represents an ideal; though the flow's inertial state appears to evolve in time, the data at every point in this figure represents basal forces from a steady developed flow. In this scenario, peak frequencies are well below 10 Hz up to an inertial state of $I \sim 10^{-2}$. This suggests that if all the basal forcing energy is radiated as seismic energy (i.e., simplifying Eq. 2.1 such that the detectable seismic signal does not depend on the green's function), the 5 Hz nodal sesimometers used by, for example, Allstadt et al. [2020] may not be able to detect signals generated by flows with inertial states less than $I < 10^{-2}$. This has implications for monitoring the incipient stages of flow, when flow is defined by unsteady particle rearrangements ($10^{-4} < I < 10^{-3}$), and the beginning phase of continuous motion when shear loads are no longer supported ($10^{-3} < I < 10^{-2}$). At this stage, broadband seismometers may be needed to detect these events, if noise does not saturate the signal. Once the bed weakens and develops into a rapid liquid-like flow, where prolonged particle contacts are maintained while flow deformation is continuous ($I > 10^{-2}$), the frequency content broadens and signals will likely be detectable by nodal deployments.

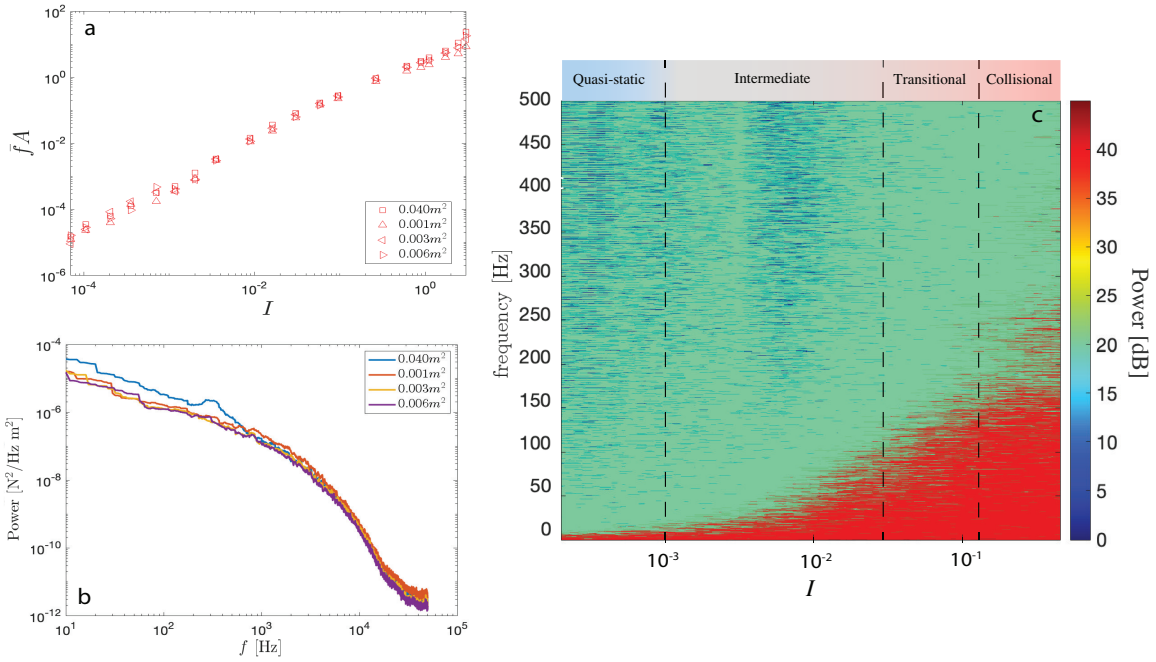

Figure 12. (a) Mean frequency $\bar{f}$ of 5 mm dry granular flow simulations, with variable simulated force plate sizes, scaled by the area of the force plate A, with areas equal to $0.001m^2$, $0.003m^2$, $0.006m^2$, and $0.04m^2$, as a function of inertial number I; (b) RMS power spectral density of basal forces derived from a dry granular flow simulation with 5 mm particle and $I \sim 10^{-2}$, with curves showing the effect of changing the force plate size; (c) spectrogram of an idealized flow with inertial states such that $10^{-4} < I < 1$, with a footprint on the order of 1 m^2. Dashed lines indicate regimes resolved through bed force fluctuations (Figure 10).

2.5 Conclusions

Here we have recorded basal forces generated during dry and submerged granular flow simulations—in plane-shear and inclined-slope flow configurations—with the aim to correlate these signals to descriptions of the flows derived from coarse-graining procedures. Utilizing both rheological and kinematic data from these simulations, we can describe four regimes, three of which have been been previously defined by granular physicists (e.g., MiDi [2004]), and fourth regime that represents the transition from a liquid-like flow, characteristic of the intermediate inertial regime, to a gas-like collisional flow, defined by the collisional inertial regime (Figure 10). Therefore, our data suggests that macroscopic rheological properties of granular flows are effectively encoded in forces exerted by the flow onto a simulated force plate. The four regimes are: (I) a solid-like regime that is characterized by the quasi-

static inertial regime ($I < 10^{-3}$), here there are long-lived force chain structures that span the entire flow domain, fluctuating basal forces are controlled by particle-scale parameters (i.e. size and hardness), granular temperature is anisotropic in the vertical axis which likely reflects endogenous noise generation as the stress-state (i.e., effective friction coefficient) decreases with increasing shear rates (velocity weakening); (II) an intermediate regime that corresponds to the intermediate liquid-like inertial regime, at this state the bed of particles deforms continuously, force chains build and break rapidly, the measure of total basal force fluctuations begins to collapse when expressed as a function of I, and granular temperature becomes isotropic reflecting particle contacts being the primary mode of granular temperature production; (III) a transitional regime that occurs in the canonical liquid-like inertial regime, showcasing a disruption in the conversion of flow driving energy into basal forcing as the flow transitions from the liquid-like to the collisional gas-like inertial state leading to a dual existence interval where boundary forcings are a function of both domain spanning force chains and individual particle impacts until the bed sufficiently dilates and the contact network is destroyed; and finally (IV) a regime characterized by the collisional inertial regime ($I > 10^{-1}$). The inability for the flow to maintain prolonged and long range force chains, which ultimately leads to a data collapses in $\Lambda(I)$ space, suggests that regardless of flow configuration, the fluctuating basal forces are a function of inertial number. In summary, Figure 10 suggests that basal tractions are well parameterized by kinematic quantities.

We have shown that basal forces can encode detailed information about the dynamics of dry and submerged granular flows. Moreover, by examining the forces exerted on the force plate, we can delimit a transitional regime that is otherwise imperceptible in the typical $\mu(I)$ and $\Phi(I)$ rheology. Importantly, this effort provides a test bed that allows us to understand what rheological and kinematic data can potentially be extracted from these signals. Future work can utilize this understanding when analyzing forcing signals from well instrumented debris-flow channels and large-scale experiments (the reader is referred to McCoy et al. [2013], Allstadt et al. [2020]). Further, the relationship between macroscopic rheological descriptions and basal forces can be leveraged into the development of sub-grid models of basal stresses. These models can be utilized in three-dimensional and depth-averaged models that can simulate flows on real-world scales, but whose resolution and derivation cannot accurately depict granular stresses that lead to substrate erosion and seismicity.

Moreover, our data provides a clue as to how inverted basal tractions from seismic signals generated by debris flows may be used to elucidate dynamical and rheological information about a given flow, providing another tool for probing these complex and dangerous phenomena.

CHAPTER III
THE ROLE OF BASAL ROUGHNESS AND ASSEMBLAGE GRAIN-SIZE DISTRIBUTION IN SHAPING GRANULAR RHEOLOGY AND BASAL-FORCE SIGNALS

From *P. Zrelak, E. Breard, and J. Dufek. The role of basal roughness and assemblage grain-size distribution in shaping granular rheology and basal-force signals. Journal of geophysical research. Earth surface. (In Review).*

3.1 Intro

Geophysical flows composed of mixtures of discrete solid particles and a fluid phase play a key role in shaping the landscape and present significant hazards to life and infrastructure. These flows span a broad spectrum, from fully dry conditions to wet and saturated states. Despite this diversity, they share a unifying feature: their rheology is strongly governed by the relative concentration of particles and fluid, as well as the dynamic coupling between the two phases [Andreotti et al., 2013, Delannay et al., 2017, Jerolmack and Daniels, 2019, Lube et al., 2020]. Many mass transport processes, such as debris flows, landslides, rock falls, and concentrated pyroclastic density currents can be classified as dense granular flows or dense granular suspensions. These concentrated flows, like many geophysical flows regardless of the solid particle concentration, have the ability to produce seismic signals that can radiate significant distances from the flows themselves [Allstadt et al., 2018]. This provides a unique opportunity to use remotely detected signals as an indirect probe of internal dynamics, a powerful tool for monitoring flow conditions to not only enact hazard responses, but also to learn more about the properties of these enigmatic phenomena. To achieve this end, there must be an understanding of the link between flow properties and the source function represented by basal tractions imparted by the flow onto the substrate. This link is essential not only for interpreting geophysical signals to infer flow dynamics, but also for understanding a flow's ability to erode the landscape and how energy is transferred and dissipated. A significant portion of this energy loss occurs through boundary stresses, which are critical for accurately modeling the energy cascade from flow-driving work to boundary interactions [Iverson, 1997]. Here we build on our previous effort where we leverage discrete element methods (DEM), solving the equations of motions explicitly for each particle within the system, to examine the link between bulk flow properties and basal-force signals

[Zrelak et al., 2024]. In this paper, we will explore how changing basal roughness conditions and grain-size distributions affect observed basal-force signals, and perform a simple one-dimensional (1-D) surface-wave propagation exercise to examine what information about the flow survives propagation through a uniform medium.

The challenge in understanding dense granular flows lies in the contrasting properties of their components: the solid particles are incompressible, while the interstitial fluid is compressible. This contrast increases the apparent viscosity of the mixture. Einstein posited that this is due to the particles' rigidity within the background flow field, increasing the dissipation of energy, thereby stating that the apparent viscosity is linearly dependent on the solid particle concentration [Einstein, 1906, 1911]. Einstein's linear viscosity relationship does not hold in concentrated flows, where the frequent contacts between particles requires consideration of both hydrodynamic interactions and direct particle-particle forces [Boyer et al., 2011]. In recent decades, a paradigm has emerged suggesting that the rheology of concentrated granular flows can be expressed as a function of a dimensionless shear rate. In the dry case (or where hydrostatic forces play a minor role in governing contact dynamics and momentum transport) the effective friction coefficient $\mu = \tau/P$—or the ratio of shear and normal stresses—is expressed as a function of the inertial number $I = d\dot{\gamma}\left(P/\rho_s\right)^{-1/2}$, where ρ_s is the solid particle density, d is the particle diameter, and $\dot{\gamma}$ is the shear rate [MiDi, 2004, Cruz et al., 2005, Forterre and Pouliquen, 2008]. This is commonly referred to as the $\mu(I)$ rheology. The inertial number I is commonly used to describe the phenomenological state of granular flows (e.g., [Forterre and Pouliquen, 2008, Breard et al., 2020]). For example, when $I < 10^{-3}$, granular assemblages are predominantly in a creeping state, and bulk flow is often characterized by stick-slip-like processes where the assemblage yields and rapidly reorganizes itself into a more stable configuration [Cruz et al., 2005]. In this solid-like regime the effective friction coefficient μ and solids concentration Φ stays relatively constant with increasing shear-rates. As the inertial numbers reach values of $10^{-3} < I < 10^{-1}$, a critical-state change occurs and the assemblages fully yield under increasing shear loads. In this regime the granular material undergoes continuous plastic deformation. This regime is often analogized as a liquid-like state, where particle contacts are friction-like, and forces are correlated in space, with these correlations often being evidenced by dynamic force-chain networks [Majmudar and Behringer, 2005, Estep and Dufek, 2012]. Finally, as $I > 10^{-1}$ the flow dilates and enters into a gas-like collisional regime, where internal

momentum is transported via particle-particle collisions. A similar formulation can be used to describe the rheology of viscous suspensions, where the effective friction coefficient becomes a function of the viscous number $I_v = \eta_f \dot{\gamma}/P$ where η_f is the fluid viscosity [Boyer et al., 2011]. By assuming additive stress scales by I or I_v, the rheology of dry granular flows and dense suspensions is unified by expressing both the solids concentration Φ and the effective friction coefficient μ as a function of $I_v + \alpha_{\Phi/\mu} I^2$, where the coefficients $\alpha_{\mu/\phi}$ represent the transition from a psuedo-Newtonian mixture to a Bagnoldian regime where inter-particle stresses results in dispersive pressures that play a role in determining the mixture's shear resistance [Bagnold, 1954, Trulsson et al., 2012, Amarsid et al., 2017, Guazzelli, 2024].

I and I_v can be related to geophysical flows by using them to express alternative dimensionless numbers that Iverson [1997] uses to analyze debris-flow physics. Namely, the Savage number, which expresses the ratio of the particles' inertia to the bulk weight, $N_{Sav} \sim I^2$, and the Bagnold number, the ratio of inertial granular shear stresses to viscous shear stresses, $N_{Bag} \sim I^2/I_v$ [Delannay et al., 2017]. These numbers are most readily calculated for controlled experiments, for example those conducted by the USGS, which have estimated values $N_{Sav} \sim 10^{-1}$ and $N_{Bag} \sim 10^2$. In our previous effort, we linked the non-dimensional variance of the basal-force signal Λ to globally defined flow parameters in both dry and liquid-immersed monodisperse granular flows in inclined-plane and plane-shear configurations [Zrelak et al., 2024]. We found that even when Stokes numbers $St = \dot{\gamma} d^2 \rho_s / \eta_f$ where less than one (or when N_{Bag} was as low as 10^{-3}), Λ scaled well with the inertial number I. This suggests that in concentrated granular flows granular inertial forces, regardless of the drag enacted on the particles, can accurately describe the basal-force distribution. Moreover, we showed that the basal forces record something akin to a phase transition as flows exited the intermediate regime and entered into the gas-like collisional regime, or when $10^{-2} < I < 10^{-1}$. In this transitional regime flow driving energy is consumed to dilate the granular assemblage, destroying the contact network and with it internal force correlations. This is significant because it shows that basal forces can be used to analyze the partitioning of flow driving energy in the bulk, and highlights processes that are not evidenced by classic rheological analysis.

Here we extend our previous effort to consider how changing basal roughness conditions and grain-size distributions affect observed basal-force signals. We conduct two suites of numerical simulations: type S1 simulations testing basal roughness

effects, and type S2 testing grain-size distribution effects (Figures 13 and 14). By varying basal roughness, we consider how both bulk rheology and basal forces might be affected as channel roughness changes. Natural flows traverse a wide variety of substrates as, for example, debris-flow bed-rock channels become filled with deposited material (e.g., [Kean et al., 2015]), or as subsequent pyroclastic density currents traverse drained channels with fine-grain linings (e.g., Kokelaar et al. [2014], and references therein). Similarly, by varying the grain-size distribution we are acknowledging that natural flows may have grain-size distributions and degree of sorting that may vary as a flow propagates. For example, a rock fall or the incipient stage of a concentrated pyroclastic density current (PDC) may have a relatively narrow grain-size distribution, but as the flow traverses down-slope, fragmentation will commonly lead to bimodal distributions (e.g., Dufek and Manga [2008], Breard et al. [2023]). Whereas debris-flows and lahars, for example, can have very wide grain-size distributions with particles ranging from sand to boulder-sized based on their energy and sediment available [Vallance and Iverson, 2015]. We acknowledge the basal roughnesses and particle-size distributions that we examine are limited compared to their natural counterparts. Nevertheless, we believe that this is a necessary first-order analysis to examine how varying these conditions affect both bulk flow dynamics and basal-force signals.

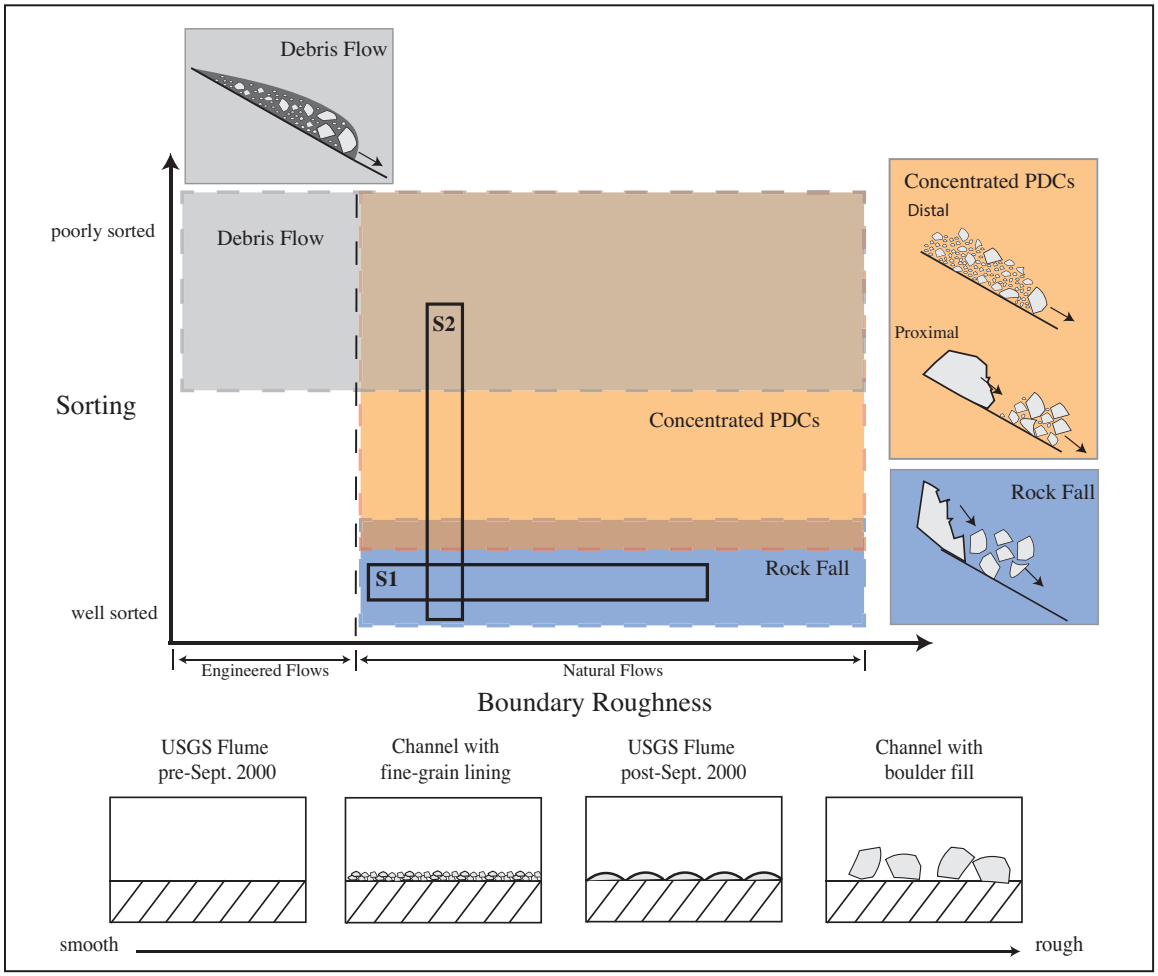

Figure 13. Relative sorting vs. basal roughness space spanned by disparate flows with boxes indicating the part of this space our type S1 and type S2 simulations are probing. Example sketches of relative boundary roughness exemplified by: the broom-finished concrete USGS flume (pre-September 2000, Logan et al. [2018]), pyroclastic flow channels with fine-grain lining [Kokelaar et al., 2014], roughness elements placed in the USGS flume [Iverson et al., 2010], and a natural channel with boulder fill.

3.2 Methods

We employ discrete element methods in computational fluid dynamics (DEM-CFD) using the U.S. Department of Energy's open-source software MFiX-DEM to model granular flows in simple shear configurations [Garg et al., 2012]. Within this framework, each particle's position and velocity is explicitly resolved via Newton's equations of motion

$$\frac{d\mathbf{X}^{(i)}(t)}{dt} = \mathbf{V}^{(i)}(t) \tag{3.1}$$

$$m^{(i)}\frac{d\mathbf{V}(t)}{dt} = \mathbf{F}_T^{(i)} = m^{(i)}\mathbf{g} + \mathbf{F}_d^{(i\in k,m)}(t) + \mathbf{F}_c^{(i)}(t) \tag{3.2}$$

$$M^{(i)}\frac{d\omega^{(i)}(t)}{dt} = \tau^{(i)} \tag{3.3}$$

where $\mathbf{X}^{(i)}(t)$ is the i^{th} particle's position, $\mathbf{V}^{(i)}(t)$ and $\omega^{(i)}(t)$ are its linear and angular velocities, $m^{(i)}$ is the particle's mass, $M^{(i)}$ is its moment of inertia, $\tau^{(i)}$ and $\mathbf{F}_T^{(i)}$ are the sum of all torques and forces acting on the particle, $\mathbf{F}_d^{(i\in k,m)}(t)$ is the drag acting on the i^{th} particle residing in the k^{th} computational cell belonging to the m^{th} solid phase, $\mathbf{F}_c^{(i)}(t)$ is the net force acting on the i^{th} particle resulting from contacts with other particles, and $\mathbf{g}$ is gravity. We model these granular systems as pure gravity-free granular flows, meaning that we do not consider fluid drag (resulting from pressure gradients and viscous forces) acting on the particles. Thus, $\mathbf{F}_d^{(i\in k,m)}(t)$ in Eq. 3.2 is neglected. This is based on the assumption that fluid drag has a negligible effect on granular basal forces in dense granular flows, which aligns with results from our previous study [Zrelak et al., 2024].

Particle contacts are modeled using the soft-sphere approach, meaning that particles may have prolonged multi-particle contacts. The soft-sphere approach allows for particles to overlap, with the overlap being modeled as a linear system of springs and dashpots in both the normal and tangential directions. Springs represent the elastic rebound of colliding particles, while dashpots model the dissipation of kinetic energy. Elastic rebound is ultimately dictated by the elastic coefficient k_n (with the subscript n denoting normal contacts), while dissipation is controlled by the dampening coefficient η_n, which is a function of the restitution coefficient e_n, the effective mass of the contacting particles m_{eff}, and k_n. The tangential elastic coefficient is taken as $k_t = 0.2k_n$ and the tangential dissipation coefficient is $\eta_t = 0.5\eta_n$. More details about MFiX's numerical techniques and validation exercises can be seen in [Syamlal, 1998, Li et al., 2012]. Table 2 details particle parameters.

3.2.1 Simulation setup

Previous efforts show that dry and liquid-submerged granular flows in plane-shear and inclined-plane configurations follow $\mu(I)$ rheology and, as a consequence, the ratio of fluctuating to mean basal stresses scale with the bulk flow properties [Breard et al., 2023, Zrelak et al., 2024]. Here we perform similar simulations of granular flows in plane-shear configurations. Particles are placed between a rough top and bottom plate composed of glued particles within periodic boundaries in the x (streamwise) and z

(spanwise) directions (see Figures 14b and 15 for examples of flow configurations). The top plate shears the particle assemblage with a prescribed translational velocity, while adjusting its vertical height to maintain a constant confining pressure of 2 kPa. The bottom plate is held static and acts as a force plate, where once the flow has reached a steady state, we record the sum of contact forces acting on the plate. This static plate is composed in one of two ways described in Section 3.2.1.1 to test how varying roughness affects bulk rheology and the basal-force signal. We run two types of dry granular-flow simulations with each simulation type contains up to 20 model runs, with top plate velocities ranging from 0.0005 ms^{-1} up to 24 ms^{-1}. Figure 14 shows the organization of simulations into the two types, depicting the various rough plates (Figure 14a) and granular assemblages (Figure 14b). Figure 15 shows an example rendering of type S2 simulations in their final state ($t = 25$ s), with the foreground depicting the force-chain network and the background the showing particle positions. Table 2 gives a summary of simulation parameters.

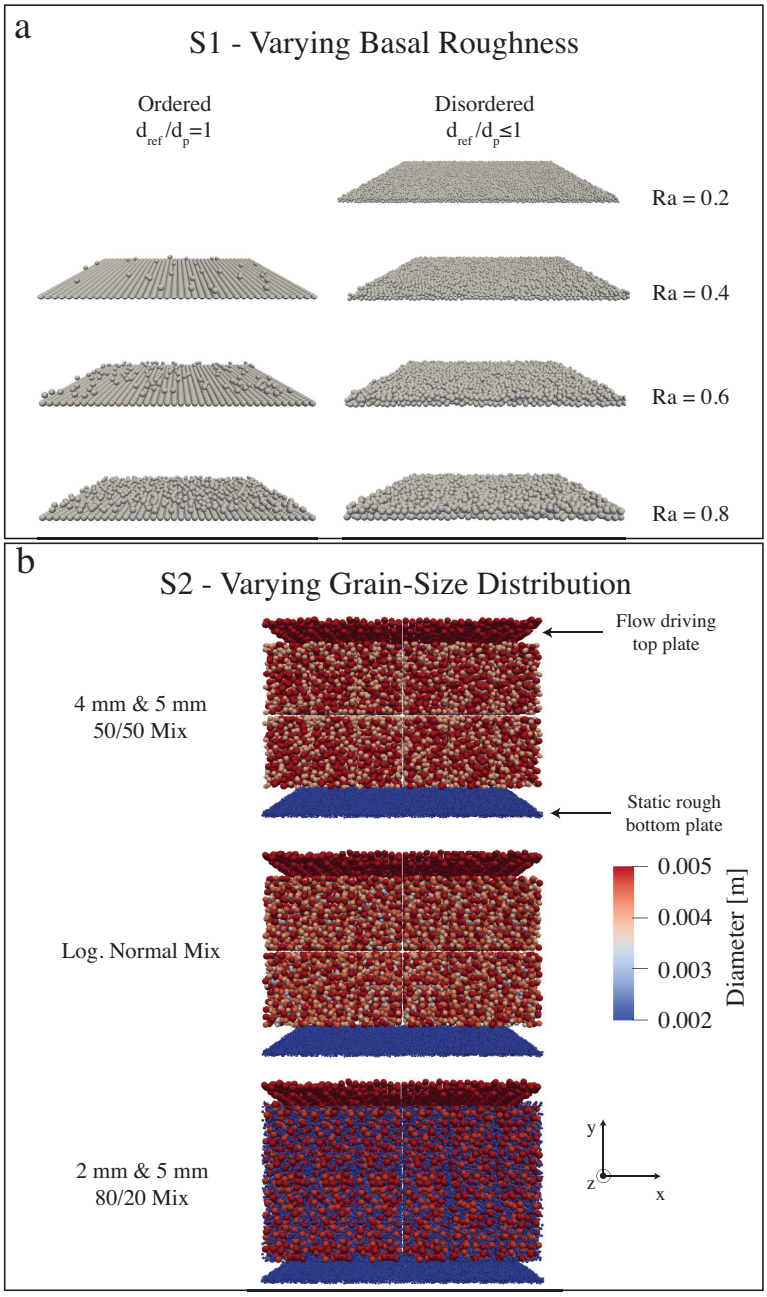

Figure 14. Visualization of simulation types and their variation. (a) Rough static base plates used in type S1 simulations separated into ordered ($d_{ref}/d_p = 1$) and disordered ($d_{ref}/d_p \leq 1$) configurations. (b) Visualizations of particle assemblages used in type S2 simulations with top flow driving plates and static rough plates shown in red and blue, respectively.

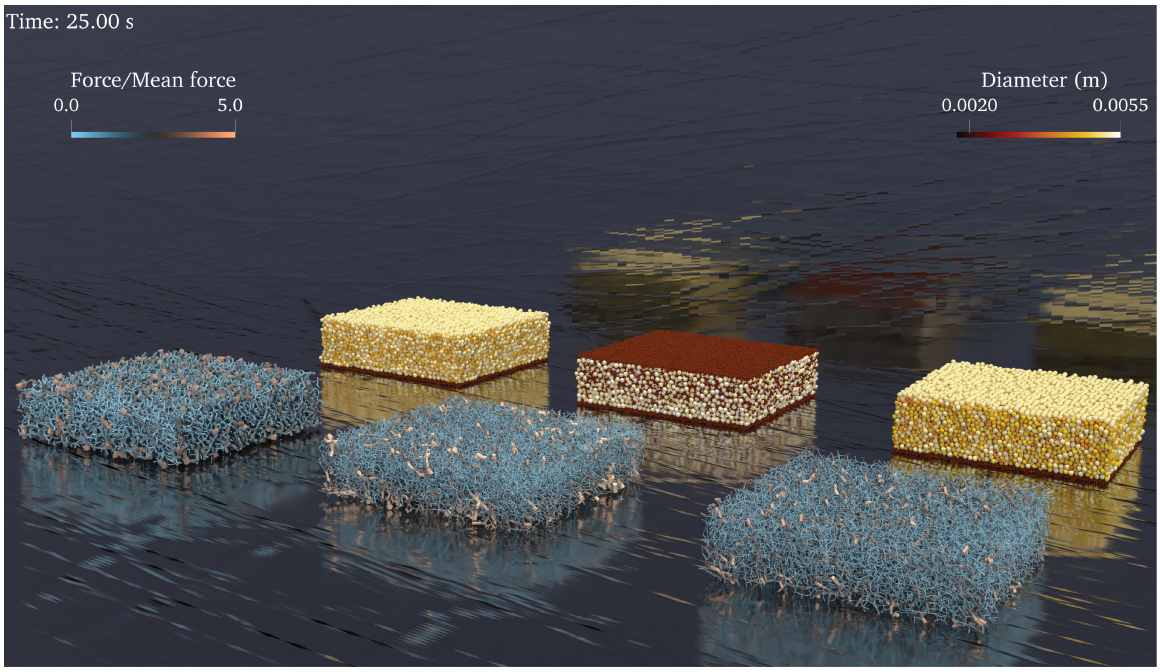

Figure 15. Example rendering type S2 simulations in their final state ($t = 25$ s). From left to right: 4–5 mm 50–50 number mixture, 2–5 mm 20–80 number mixture, and the approximately log-normal mixture. The foreground shows the particle-contact network and force chains via tubes with orientations corresponding to the contact orientation and thicknesses scaled by the contact force divided by the mean contact force.

Table 2. Summary of constant parameters and simulation configuration.

Setup Parameters

parameter	*variable*	*value*
domain size[1] $[m]$	$X \times Y \times Z$	$40d_{ref} \times \geq 20d_{ref} \times 40d_{ref}$
confining pressure $[kPa]$	P	2
particle density $[kg\ m^{-3}]$	ρ_s	1050
particle friction coeff.	μ_p	0.53
normal restitution coeff.	e_n	0.6
normal elastic coeff.[1] $[Pa\ m]$	k_n	$(2 \times 10^8)d_{ref}$
normal dissipation coeff. $[kg/s]$	η_n	$\frac{2\sqrt{m_{eff}k_n}\lvert ln\ e_n\rvert}{\sqrt{\pi+ln^2 e_n}}$
tangential elastic coeff. $[Pa\ m]$	k_t	$0.2k_n$
tangential disspation coeff. $[kg/s]$	η_t	$0.5\eta_n$

Simulations

Sim.	*GSD*	d_p	*Ra*
S1.1	mono. ($\pm$5%)	5 mm	0.4
S1.2	mono. ($\pm$5%)	5 mm	0.6
S1.3	mono. ($\pm$5%)	5 mm	0.8
S1.4	mono. ($\pm$5%)	2 mm	0.2
S1.5	mono. ($\pm$5%)	3 mm	0.4
S1.6	mono. ($\pm$5%)	4 mm	0.6
S1.7	mono. ($\pm$5%)	5 mm	0.8
S2.1	4-5 mm 50/50 mix[2]	2 mm	0.2
S2.2	2-5 mm 80/20 mix[3]	2 mm	0.2
S2.3	Log Norm.[4]	2 mm	0.2

[1] $d_{ref} = 5$ mm
[2] $d_{43} = 4.57$ mm
[3] $d_{43} = 4.32$ mm
[4] $d_{43} = 4.51$ mm

To derive global flow properties from the discrete particle data, we write out the position, velocity, and forces acting on every particle in the system at a frequency of 100 Hz for one second in simulation time once the simulations reach a steady state—as defined by the average particle velocity over a one second interval being within 5% of the average velocity in the interval prior. This data is then used to derive continuous fields that we then integrate to express the global averages (see Section 3.2.2). In order to fully resolve particle forces, we write out the sum of contact forces exerted on the bottom plate at a frequency of 100 kHz (therefore being near the same timescale for particle deformation $\tau_d = d/(k_n/\rho_s d)^{1/2}$), again, for a single second in simulation time. We then detrend the basal force time series, to isolate the fluctuating forces, and use a Hann window to segment the time series into 0.5 s segments with 80% overlap. The segments are used to calculate the one-sided Fourier transform. We then calculate the power spectral density and use a Konno-Ohmachi filter to smooth the spectra, preserving their general characteristics [Konno and Ohmachi, 1998].

3.2.1.1 S1: Varying basal roughness

In the first set of simulations we keep the grain-size distribution constant, being approximately monodisperse with 5 mm particles (±5% dispersion) and change the properties of the bottom static force plate. We construct the bottom plate in two ways: (1) we construct the rough plate by placing particles on top of an ordered lattice until a desired roughness is achieved (labeled as ordered in Figure 14a); (2) we randomly construct the plate by forcing a collection of particles with diameter d_p to the bottom of the simulation domain then define a plane $y = 2d_p$ below which particles are fixed (disordered in Figure 14a).

To construct a basal plate with a desired roughness we must first adopt a method of measuring basal roughness. Here we use methodology developed by [Jing et al., 2016], where Delaunay triangulation is used to discretize the particle positions into a triangular mesh. The areas of the triangular patches that comprise the void space between adjacent particles is used to calculate a local area roughness:

$$R_{al} = \frac{\frac{\sum_k 1+\epsilon_k}{2} \prod_k \left[\frac{\sum_k (1+\epsilon_k)}{2} - 1 + \epsilon_k \right]}{\frac{\sqrt{3}}{4}(1 + \frac{d_{ref}}{d_p})^2} \tag{3.4}$$

where the index l denotes the l^{th} triangle, ϵ_k is the triangle side length ($k = 1, 2, 3$ for the three sides of the triangle), d_{ref} is a reference diameter representing the averaging flow-particle diameter ($d_{ref} = 5$ mm), and d_p is the diameter of the particles

comprising the bottom plate. Eq. 3.4 is essentially comparing the area of the l^{th} void space by the area of the most stable situation in which the flowing particle's center is coplanar with the triangular mesh [Jing et al., 2016].

To construct our desired basal plate, we start with a hexagonal layer of particles then place individual particles on top of this layer. We continue to add particles on top of the lower layer until a desired roughness is met, defined by the mean of the local roughness calculated for each void space $R_a = \frac{1}{N_l}\sum_l R_{al}$, where N_l is the total number of triangles. This calculation is performed for each layer of particles j. This means that adjacent layers will be accounted for in the event that the l^{th} void space is larger than a critical area, such that a flowing particle will be in contact with the lower layer. This critical area is the void area at which point a flowing particle will be tangent to three fixed particles (the three apices of the triangular mesh) and a reference plain representing the top boundary of the lower layer. We use a weighted average following Jing et al. [2016] to account for roughness contributions from an adjacent lower layer.

The second method we use to construct a rough base is less ordered, as we are no longer working with layers of glued particles that are co-planar to each other, i.e., we do not construct the base by exactly placing particles on top of a hexagonal lattice, but instead randomly generate a base by freezing settled particles in place. Nevertheless, we approximate the roughness of these plates using similar methods outlined above. Each randomly generated rough plate has a height of $y = 2d_p$, thus we can approximately calculate the average local roughness R_a for three layers of particles that are within a band with a thickness of d_p. In this way, band l contains particles with vertical extents defined by $(\frac{y}{d_p} > l,\ \frac{y}{d_p} < l + 1)$.

3.2.1.2 S2: Varying grain-Size distribution

We run three suites of simulations where we vary the grain-size distribution (GSD) while keeping the bottom plate roughness constant. The bottom plate is composed of randomly settled 2 mm particles (the same plate as simulations S1.4) with an estimated roughness of $Ra = 0.2$. Two of these simulations are bidisperse assemblages: a 50/50 number mixture of 4 mm and 5 particles, and a 80/20 number mixture of 2 mm and 5 mm particles. A third set of simulations is run with a particle assemblage having an approximate log-normal GSD with a frequency distribution

defined as

$$f_n = \frac{1}{d\sigma_n\sqrt{2\pi}} e^{-\frac{(ln(d)-\mu_d)^2}{2\sigma^2}} \tag{3.5}$$

where d is the particle diameter, σ^2 is the variance and μ_d is the mean diameter. Here $\sigma_n = 0.2\mu_d$ and $\mu_d = 5$ mm. We discretely sample this distribution with 6 particle sizes ranging from 2–5 mm. We can express the mean particle size of each of these distributions with the volume-mean diameter d_{43}, which is used to calculate the inertial number I and has been shown to correctly scale for grain-size effects in poly-disperse granular flows [Gu et al., 2016, Breard et al., 2024]

$$d_{43} = \frac{\sum_i^N d_i^4}{\sum_i^N d_i^3} \tag{3.6}$$

where N is the number of particles. d_{43} values are shown in Table 1.

3.2.2 Coarse Graining and Scaling

The goal of this effort is to relate bulk flow characteristics to basal-force signals in order to understand the relationship between global fields and basal forces generated by our simulated granular flows. Therefore we employ a coarse-graining methodology to derive continuous fields from discrete data, and integrate these fields to express them as vertical averages. This provides a necessary link between discrete data obtained from the DEM approach to continuum and depth averaged models [Weinhart et al., 2013]. Details of our coarse-graining algorithm and full descriptions of the calculated tensor fields can be seen in Fullard et al. [2019] and Breard et al. [2020]. In summary, a smoothing function (a polynomial kernel with a defined smoothing length-scale) is applied to calculate fields that satisfy continuity and conservation of momentum equations. We follow the suggestion of Weinhart et al. [2016] and Tunuguntla et al. [2016] by using a coarse-graining width w such that $w/d_{avg} = 0.75$, where spatially-averaged fields are parameter independent. We integrate these fields to derive smooth vertical profiles, and domain averages, of parameters such as the average velocity V and the solid volume fraction Φ.

The coarse-graining method decomposes the total stress tensor σ into a sum of the kinetic stress tensor σ_k and the contact stress tensor σ_c. The kinetic tensor is a function of particle-velocity fluctuations, while the contact tensor is a function of particle-contact forces. From this decomposition, we calculate the solid pressure as the average normal stress, or the trace of the contact stress tensor

$$P_s = \frac{1}{3} tr(\sigma_c) \tag{3.7}$$

Similarly, the trace of the kinetic stress tensor is used to calculate the iso-tropic granular temperature

$$T = \frac{1}{3\rho_s} tr(\sigma_k) \tag{3.8}$$

We can relax iso-tropic assumption and calculate the granular temperature in the i^{th} direction as $T_i = \sigma_k^{ii}/\rho_s$.

Following Breard et al. [2024] and Weinhart et al. [2013] we use the magnitude of the deviatoric part of the 2-D total stress tensor, and the 3-D solids pressure (Eq. 3.7) to define the bulk friction coefficient

$$\mu = \frac{|\sigma^D|}{P_s} \tag{3.9}$$

This definition is used as the static friction coefficient (μ as $\dot{\gamma} \to 0$) more closely aligns with the tangent of the angle of repose [Weinhart et al., 2013]. We use our coarse-grained fields and the volume-mean diameter to calculate a global inertial number for each sheared particle assemblage

$$I = \frac{\dot{\gamma} d_{43}}{\sqrt{P_s/\rho_s}} \tag{3.10}$$

where $\dot{\gamma}$ is the magnitude of the deviatoric shear-rate tensor.

3.3 Results

Here we present results from our simulations testing the effects of basal roughness (S1) and grain-size distribution (S2) on granular rheology and basal forces. We will start by considering how these parameters affect the internal rheology through the use of our CG technique, deriving domain averages from discrete data. After, we will describe how basal-force signals change with respect to these bulk parameters, with a primary focus on the power spectral density of the basal-force time series.

3.3.1 Rheology and Kinematics

Figure 16a-b depicts the effective internal friction coefficient μ for type S1 (nearly monodisperse mixtures with variable roughness) and type S2 (bidisperse and polydisperse mixtures with constant basal roughness) simulations as a function of inertial number I. In Figure 16a, μ decreases with decreasing basal roughness for inertial numbers below 10^{-2}, whereas fines-enriched assemblages exhibit only a slight reduction (Figure 16b). At high inertial numbers ($I > 10^{-1}$) the effective friction coefficient begins to spread in type S2 simulations (Figure 16b). This is one example of configurations with relatively smooth substrates (where $d_p = 2$ mm, $Ra = 0.2$)

no longer being well described by $\mu(I)$ rheology, as the relatively smooth substrate fails to prevent crystallization (or ordering of the granular assemblage). As such, the basal boundary condition effectively becomes a near-free-slip condition, generating plug flow and precluding the beds from reaching inertial numbers much greater than 10^{-1}. We circle this crystallization event, when evident, in subsequent figures. Similarly, as we decrease basal roughness, the concentration Φ at low inertial numbers increases slightly (Figure 16c), though there is a much more visible increase, with a marked increase in the dilation rate, when assemblages are fines-enriched (Figure 16d). Again, flows with a relatively smooth basal roughness show divergences from general trends, as regular ordering and crystallization leads to an abrupt increase in solid concentration (Figures 16c-d).

Jop et al. [2006] shows that the bulk friction coefficient of sheared granular assemblages follows the empirical law:

$$\mu(I) = \mu_1 + \frac{\mu_2 - \mu_1}{1 + I_0/I} \tag{3.11}$$

where μ_1 is the static friction coefficient (μ as $I \rightarrow 0$), while μ_2 and I_0 are fit parameters. Similarly, Amarsid et al. [2017] uses an empirical fit to describe how the particle concentration varies with inertial state

$$\Phi(I) = \frac{\Phi_1}{1 + aI} \tag{3.12}$$

where Φ_1 is the steady-state quasi-static max packing, and a is a fit parameter on the order of 1. Figures 16a-b show that the static friction coefficient μ_1 decreases by nearly 10% when basal roughness Ra decreases from 0.8 to 0.2, but is only marginally affected by changes in the grain-size distribution, in agreement with data presented in Breard et al. [2024] showing that the grain-size distribution does not affect the effective friction coefficient. In contrast to the static friction coefficient μ_1, the steady-state quasi-static max packing Φ_1 varies by less than 1% when the bottom plate roughness decreases from 0.8 to 0.2 (Figure 16c), but increases by nearly 10% when assemblages are fines-enriched (Figure 16d). Yu and Standish [1991] describe how the packing efficiency in bidisperse mixtures is a function of their size ratio and relative population of the two particle classes, explaining why we see a drastic increase in Φ_1 with increased fines content. Figure 16e-d combines data from the two types of simulations and plots $\mu - \mu_1$ and $\Phi - \Phi_1$ as a function of I, respectively. Figure 16e shows that data from type S1 and S2 simulations agree well, up until $I > 10^{-1}$, or when the flows enter into the gas-like inertial-collisional limit, again, being a sign of

crystallization. Figure 16f generally shows good agreement among the two simulation types, but also displays: (1) deviations from the common $\Phi(I)$ relation when $I > 10^{-1}$, relating to flow crystallization, and (2) fines enriched mixtures dilating at a faster rate when $I > 10^{-3}$.

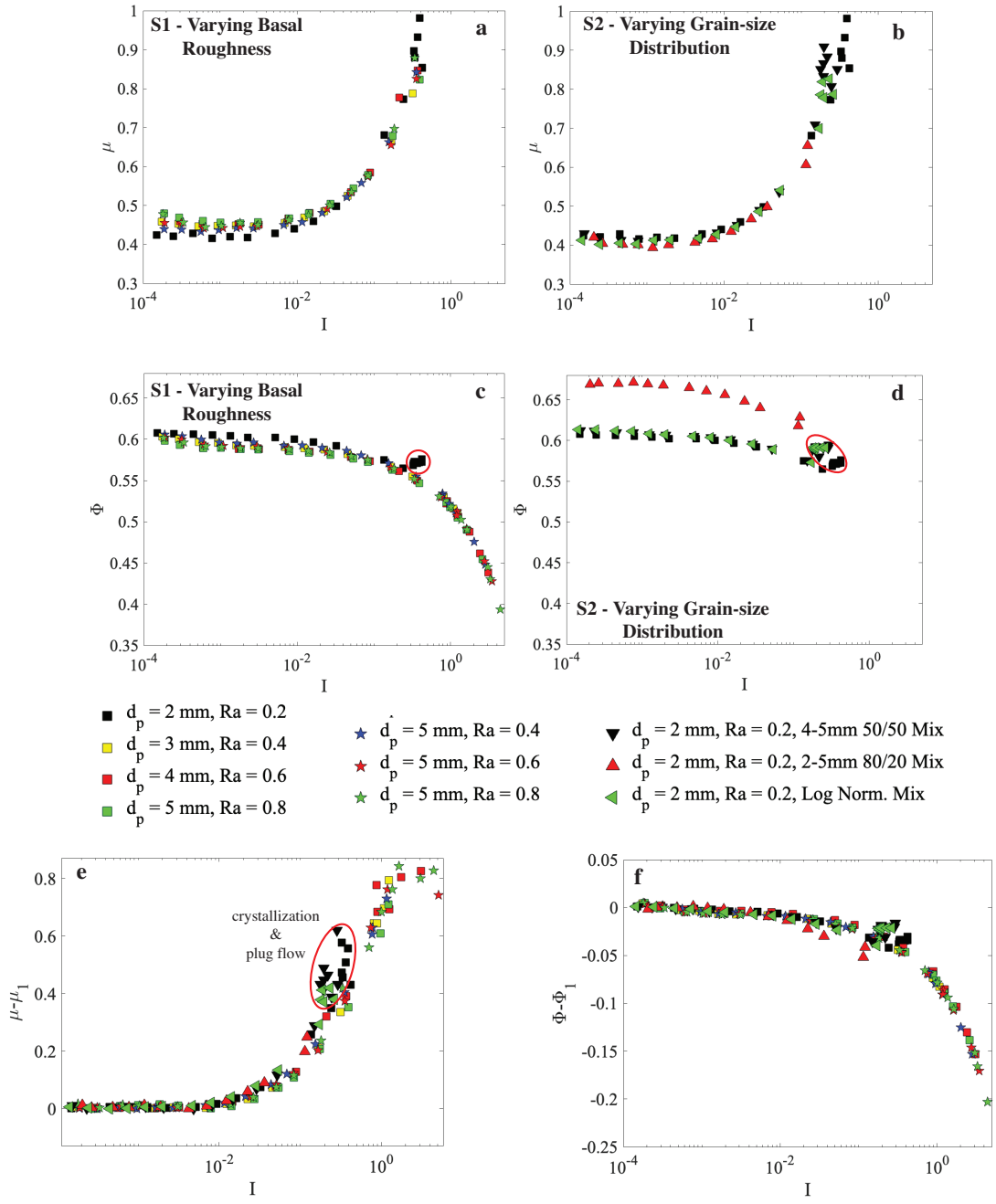

Figure 16. Domain-averaged (coarse-grained) $\mu(I)$ rheology for type S1 monodipserse simulations (a) and type S2 bidisperse/polydisperse simulations (b). Coarse grained $\Phi(I)$ scaling for type S1 (c) and type S2 (d) simulations. Combined data depicting the difference in internal friction μ from static friction μ_1 (e), and solid concentration Φ from steady-state quasi-static max packing Φ_1 (f). Annotated circles mark when assemblages crystallize and plug-like flow develops.

Figure 16 displays how the the common $\mu(I)$ and $\Phi(I)$ relations are affected by varying basal roughness and grain-size distribution, while keeping all other material constants unchanged. Figure 17 shows how internal kinematics and energy partitioning are affected by these changes. We observe that coarse-grained stream-wise velocity V_x increases with decreasing roughness, for a given inertial state (Figure 17a). This increase is directly related to the increase in slip at the base of these flows. The inset in Figure 17a plots vertical profiles of dimensionless stream-wise velocity for flows with inertial numbers on the order of 10^{-2}, showing that the velocity profile transitions from linear to Bagnold-like, where the later case indicates shear localization. In Figure 17a-b we observe another obvious sign of crystallization; there is a rapid increase in the coarse-grained stream-wise velocity for flows with basal roughness of 0.2 when $I > 10^{-1}$. This rapid increase is directly related to the regular ordering of the granular assemblage (or crystallization), and the development of a plug flow in the (near) absence of shear gradients within the bulk of the assemblage.

After examining mean flow properties we can now examine internal granular temperature T, giving insight into how the velocity distribution is affected by changes in basal roughness and grain-size distribution (Figures 17c-d). We report granular temperature as an isotropic quantity as we neglect the role of an interstitial fluid—which can affect the partitioning of fluctuating energy into stream-wise and span-wise components [Zrelak et al., 2024]—and because most of our data points fall within the quasi-static and intermediate regimes where granular temperature is roughly isotropic (i.e., $10^{-4} < I < 10^{-1}$; Campbell [2006]). Figure 17c shows that roughness hardly affects internal granular temperature, though mean velocities are directly influenced by basal roughness. Conversely, Figure 17d shows that fines directly lead to a marked increase in granular temperature for any given inertial number. Given the inventory of mean and fluctuating components of the particle velocity distribution—as measured using the averaged-stream-wise velocity V_x and granular temperature T, respectively—it is instructive to directly compare these quantities to understand how kinetic energy is redistributed with changes in basal roughness and grain-size distribution. Figures 17e-g depict the ratio T/V_x^2 as a function of inertial number. Figure 17e shows that this ratio decreases with decreasing roughness. Conversely, there is a marked increase when the beds are relatively fines-enriched (Figure 17f). We combine these two simulation types, rescaling T/V_x^2 by the roughness parameter Ra to account for variations caused by changing roughness conditions (Figure 17g).

This rescaling and subsequent collapse demonstrates that the decrease in T/Vx^2 with decreasing roughness is due to increases in basal slip; decreasing roughness increases basal slip, thereby increasing the averaged stream-wise flow velocity. Though rescaling collapses the changes in T/V_x^2 with varying degrees of roughness, there still exists a region that reflects an excess in fluctuating energy introduced by fine particles in the bidisperse $2-5$ mm $80/20$ number mixture. This excess relaxes with increasing shear rates and eventually meets the group trend when inertial numbers approach 10^{-1}, though this convergence is ultimately interrupted by crystallization and plug flow.

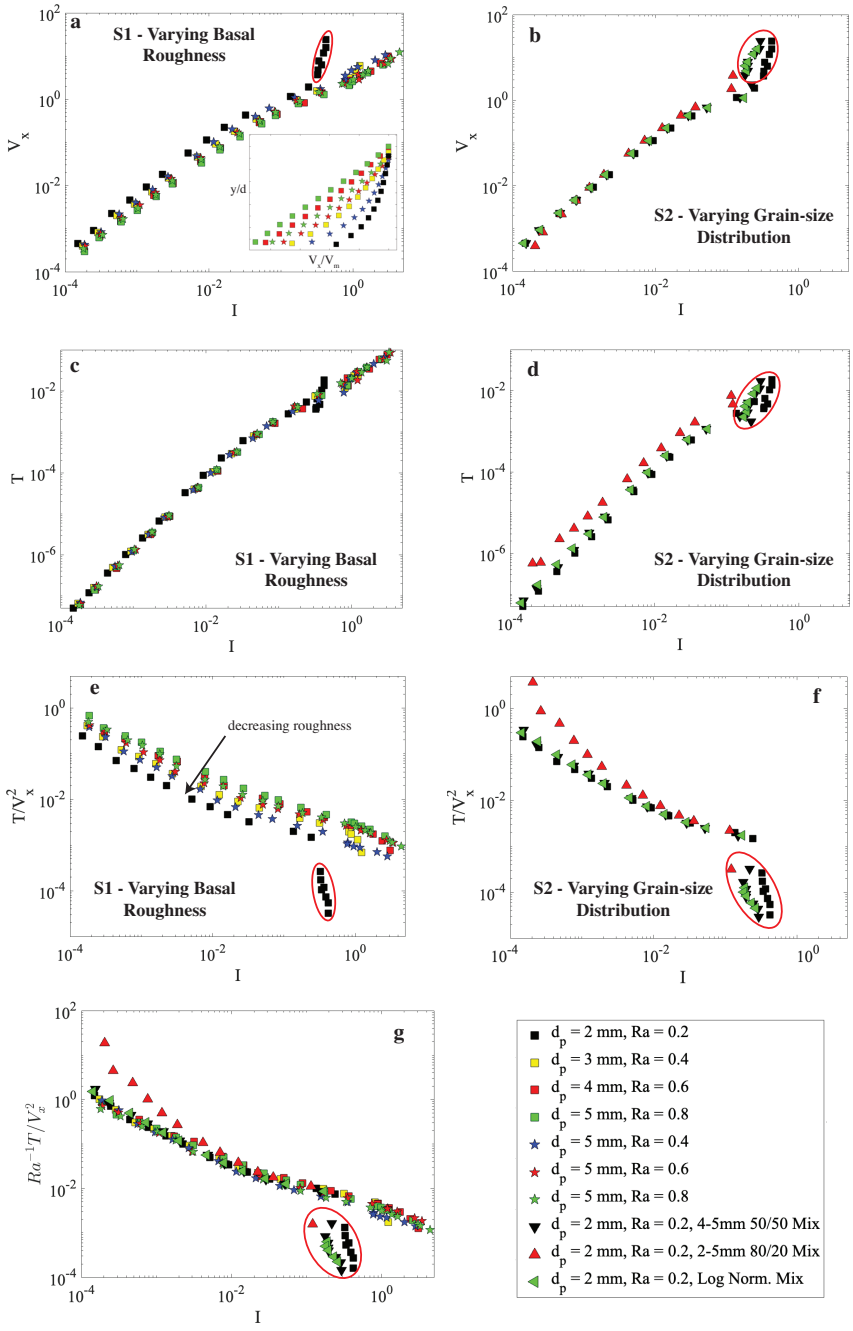

Figure 17. Domain-averaged (coarse-grained) stream-wise velocity V_x as a function of I for type S1 (a) and type S2 (b) simulations. Internal granular temperature T as a function of I for type S1 (c) and type S2 (d) simulations. The ratio of mean to fluctuating kinetic energy T/V_x^2 as a function of I for type S1 (e) and type S2 (f) simulations. (g) Combined data with T/V_x^2 scaled by the averaged-basal roughness parameter Ra^{-1}. Inset: normalized stream-wise velocity profile for type S1 simulations.

The above analysis can also be performed on basal quantities in order to get a complete picture of the cascade from internal dynamics to basal properties. We can define the effective basal friction coefficient, following Artoni and Richard [2015], as the ratio of shear to normal basal stresses—or the sum of particle forces in x and y directions $\mu_w = \sum F_x / \sum F_y$ (Figure 18a-b)—the average slip velocity V_s as the arithmetic mean of the stream-wise velocity of all particles in contact with the bottom plate (Figure 18c-d), and the basal granular temperature T_w as the arithmetic average of the fluctuating velocity $v = v_x - V_s$ of all particles in contact with the bottom plate (Figure 18e-f). Further, as above, we combine the basal friction data from the type S1 and S2 simulations by plotting the deviation from the static wall friction value $\mu_1^{(w)}$ (Figure 18g) and also include the ratio of the basal granular temperature and internal coarse-grained granular temperature T_w/T (Figure 18h). Similar to the bulk friction coefficient μ, the basal effective friction decreases with reduced roughness, while variations in grain-size distribution produce virtually no change (Figures 18a-b). When examining the difference from the apparent static value $\mu_w^{(1)}$ we find that much of the offset is accounted for, however, a residual spread persists across the simulations (Figure 18g). As in the coarse-grained stream-wise velocity V_x, there is an increase in slip velocity as basal roughness decreases, which is also reflected in the basal granular temperature (Figures 18c and 18e, respectively). Strikingly, there is drastic decrease in effective wall friction as flows crystallize and develop into plug-like flow states (Figures 18a-b,g). This transition coincides with a sharp increase in both slip velocity and basal granular temperature. Additionally, the ratio of basal to internal granular temperature decreases with increasing basal roughness, showing nearly an order of magnitude difference under nominal conditions for flows over relatively smooth substrates (Figure 18h). Moreover, basal granular temperature increases to nearly two orders of magnitude greater than the internal granular temperature when flows crystallize and develop into plug-like flow states (circled markers, Figure 18h). Figure 18h shows that the ratio T_w/T for nearly all the simulations fall on near-parallel lines that are dependent on the basal roughness aside from two scenarios: (1) as mentioned above, when the flows develop into plug-like flow states, and (2) when assemblages are enriched in fine particles (red triangles, Figure 18h). The ratio T_w/T for the fines enriched assemblages is not only a function of the basal roughness, but also inertial number. This indicates that shear localization leads to the advection of coarse particles in the direction of the shear gradient [Jing

et al., 2021]. Thus, as coarse particles segregate down to the bottom of the domain, with increasing shear rate, the scale roughness decreases, resulting in an increase in T_w/T. Aside from this effect, we see that basal properties are keenly sensitive to basal roughness, whereas the grain-size distribution has little effect, if the grain-size distribution is rather narrow and there is not a great deal of particle segregation.

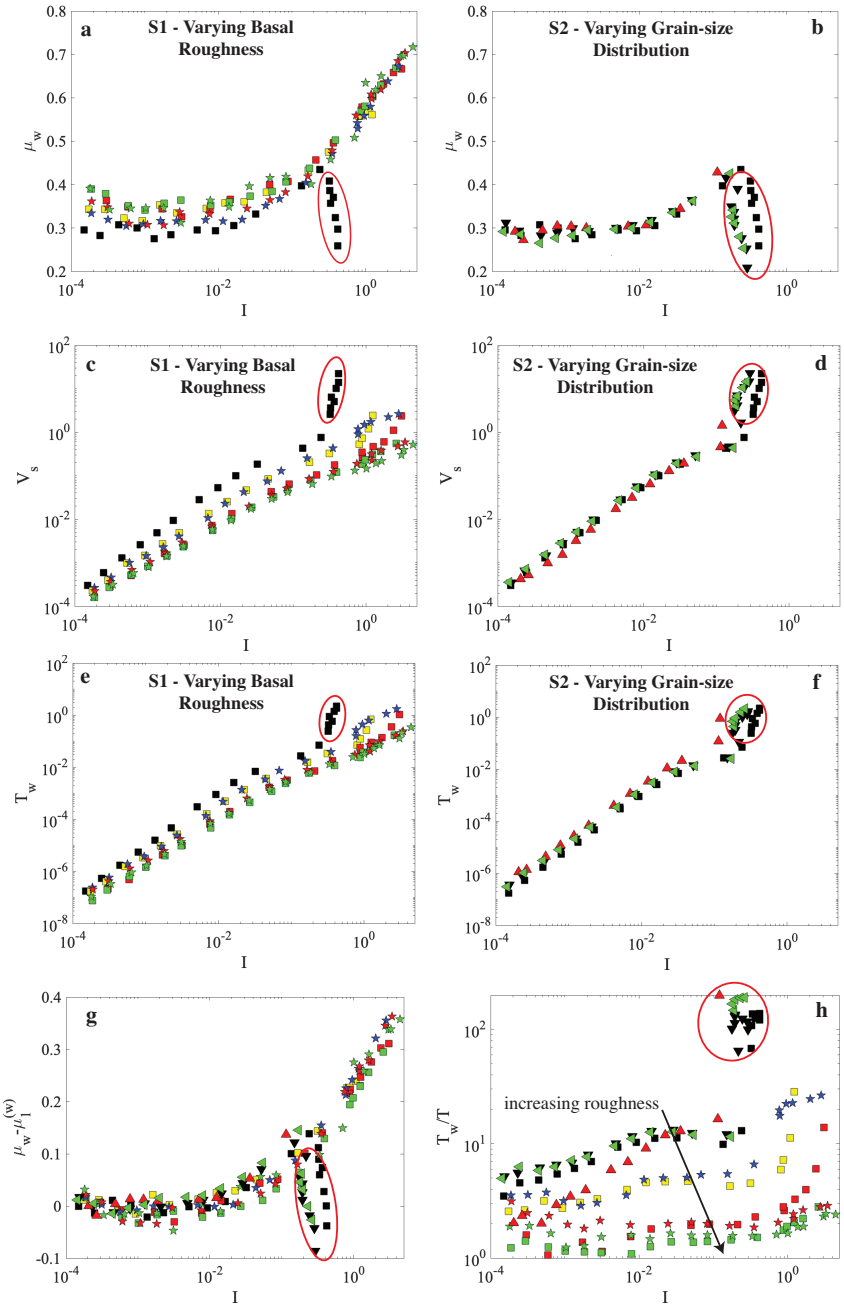

Figure 18. Effective basal friction coefficient μ_w as a function of I for type S1 (a) and type S2 (b) simulations. The basal-averaged stream-wise slip velocity as a function of I for type S1 (c) and type S2 (d) simulations. The base-averaged granular temperature as a function of I for type S1 (e) and type S2 (f) simulations. Combined data depicting the difference in μ_w from static values $\mu_1^{(w)}$ (g) and the ratio of basal granular temperature to internal granular temperature T_w/T (h).

3.3.2 Basal Force Spectra

Previously, we have shown that the shape of the power spectral density of the basal force time series is controlled by the inertial state of granular flows [Zrelak et al., 2024]. We continue to explore this by calculating the power spectra as we vary basal roughness and grain-size distribution. Figure 19 displays basal force spectra from four suites of simulations, two of type S1 and two of type S2. Figure 19 shows that the spectra transitions from rapidly decaying, when $I \leq 10^{-3}$, and gradually lifts until there is a relatively flat response up to a corner frequency that is a function of particle size and inertial number [Zrelak et al., 2024]. Notably, we observe spectral peaks that occur at about 300 – 400 Hz when inertial numbers are less than or equal to $\sim 10^{-2}$, though these peaks are less visible when the mixture is fines-enriched (Figure 19d). A physical interpretation of the inertial number is that it represents the ratio of the particle rearrangement timescale and the macroscopic deformation time of the bulk assemblage [MiDi, 2004]. The particle rearrangement timescale is the time it takes for a particle to fall into an energy well (or resting position) after mounting an adjacent particle as it is sheared and subjected to a confining pressure: $\tau_p = d(P/\rho_s)^{-1/2}$. Using the top plate confining pressure of 2 kPa as a pressure scale, a solid particle density ρ_s of 1050 kg/m^3, and a particle diameter d of 5 mm yields a timescale of ~ 0.004 s, or a frequency of 250 Hz. Using the solids pressure (Eq. 3.7) as the pressure scale for flows with inertial numbers $\leq 10^{-2}$ yields timescales with frequencies closer to the observed peaks, ~ 300 Hz. Therefore, these spectral peaks are related to the percolation of forces down to the bottom plate as particles rearrange under shear. This interpretation aligns with our previous work showing that when the monodisperse particle size decreases by an order of magnitude the frequency of these spectral peaks increases by an order of magnitude [Zrelak et al., 2024]. Data generated by the fines-enriched mixture do feature these peaks when assemblages are in the solid-like quasi-static state (i.e., when $I \leq 10^{-3}$), but the peaks are flattened as soon as the inertial number increases such that flows begin to yield continuously (Figure 19d).

Another spectral property that is shared among the various simulations types is that a great deal of power is partitioned into the ~ 1 – 100 Hz band when flows have inertial values of $10^{-2} < I < 10^{-1}$. This aligns with the 'transitional' regime identified in multiphase and dry monodisperse granular flows in plane-shear and inclined-slope configurations [Zrelak et al., 2024]. Note that these features are attenuated when flows

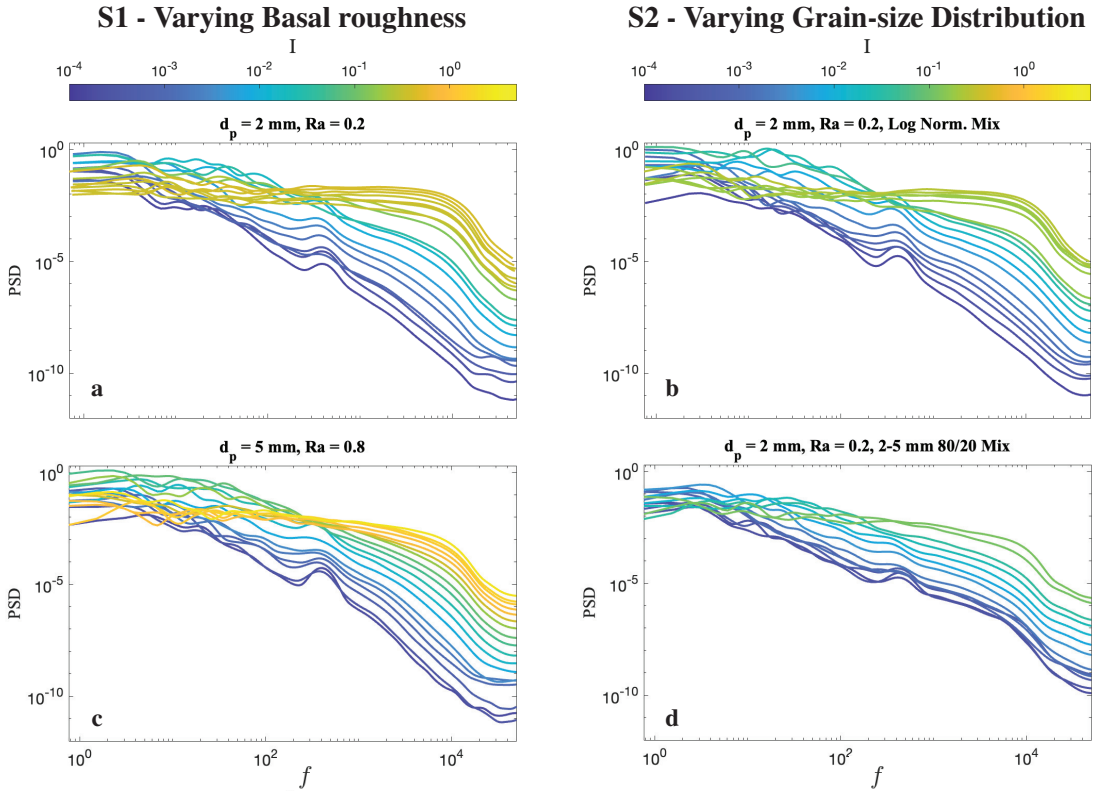

Figure 19. Aggregation of smoothed basal-force power spectral densities from four sets of simulations with each curve colored by the inertial number of the flow. (a) type S1 monodisperse simulation with an averaged basal roughness $Ra = 0.2$, (b) type S2 simulation with a log-normal particle size distribution and a basal roughness $Ra = 0.2$, (c) type S1 monodisperse simulation with basal roughness $Ra = 0.8$, and (d) type S2 simulation with a bidisperse particle size distribution with an enriched fine-particle content and basal roughness $Ra = 0.2$.

have a relatively enriched fine particle content (Figure 19). Previously, we used the non-dimensional integral of the power spectral density Λ to identify this transitional regime

$$\Lambda = \frac{\int_{f_{low}}^{f_{ny}} P(f)df}{\langle F(t)\rangle^2} \tag{3.13}$$

where $P(f)$ is the power spectral density, $\langle F(t)\rangle$ is the time average of the sum of basal forces exerted on the bottom plate, f_{low} is a low frequency cut-off (1 Hz), and f_{ny} is the Nyquist frequency (50 kHz). This is inspired by Arran et al. [2021], where the authors use a similar metric as an overall estimate of the high frequency variance of the basal-force time series. Figure 20 shows this parameter (unscaled and scaled by

the basal roughness, Figures 20a-b and 20c-d, respectively) as a function of inertial number and deviations from the steady-state quasi-static solids concentration $\Phi - \Phi_1$. Comparing Figures 20a-b with 20c-d shows how sensitive this scaling relationship is to basal roughness, though this sensitivity is diminished when plotting Λ as a function of concentration, until the flows are relatively dilute and are within the inertial-collisional regime (i.e., $I > 10^{-1}$). Figures 20a and 20c follow the same general trend described in Zrelak et al. [2024]; there is a log-linear increase in Λ with inertial number when I ranges from $(10^{-4}, \sim 10^{-2}]$, after which Λ stalls and decreases, until it recovers a log-linear relationship when $I >\sim 10^{-1}$. This stalling and decrease in Λ is the signature of the transitional regime. Here, low frequency and mean basal forcing signals increase relative to the variance, as observed in the spectra depicted in Figure 19. Within the transitional regime, we see that the granular system is approaching a critical point where spatial correlations increase, evidenced by the increase in power within frequency bands less than 100 Hz when the simulated force-plate area increases (Zrelak et al. [2024]: Appendix A.7). The critical point is also observed in the abrupt change in how Λ scales with deviations from the steady-state solids concentration at a critical value Φ_c (Figures 20b and 20d). This critical solids concentration is similar to a glass-like transition: when $\Phi > \Phi_c$ kinetic proprieties are inhibited, thus bulk strain is suppressed and assemblages are well within a contact-dominated regime [Cohen and Turnbull, 1959, Ness and Sun, 2015, Zhang and Kamrin, 2017].

Figure 20 shows that Λ has a general sensitivity to basal roughness, and also shows that fines-enriched mixtures have slightly higher values when comparing to flows at equivalent inertial states (red triangles, Figure 20). To further elucidate how basal roughness and grain-size distribution affect the basal-force spectra, we use spectral moments to calculate the 'radius of gyration' Ω, or the the average distance from the central frequency, giving an estimate of the concentration of power on the frequency axis [Vanmarcke, 1972]

$$\Omega = \sqrt{\frac{\lambda_2}{\lambda_0}} \tag{3.14}$$

where λ_n are the spectral moments

$$\lambda_n = \int_f f^n P df \tag{3.15}$$

Note that Λ in Eq. (3.13) is the 0^{th} moment λ_0 normalized by the time-averaged square of the basal force. Figures 21a-b depicts a rather noisy scaling between Ω and inertial number for both simulation types. Plotting Ω as a function of coarse-grained

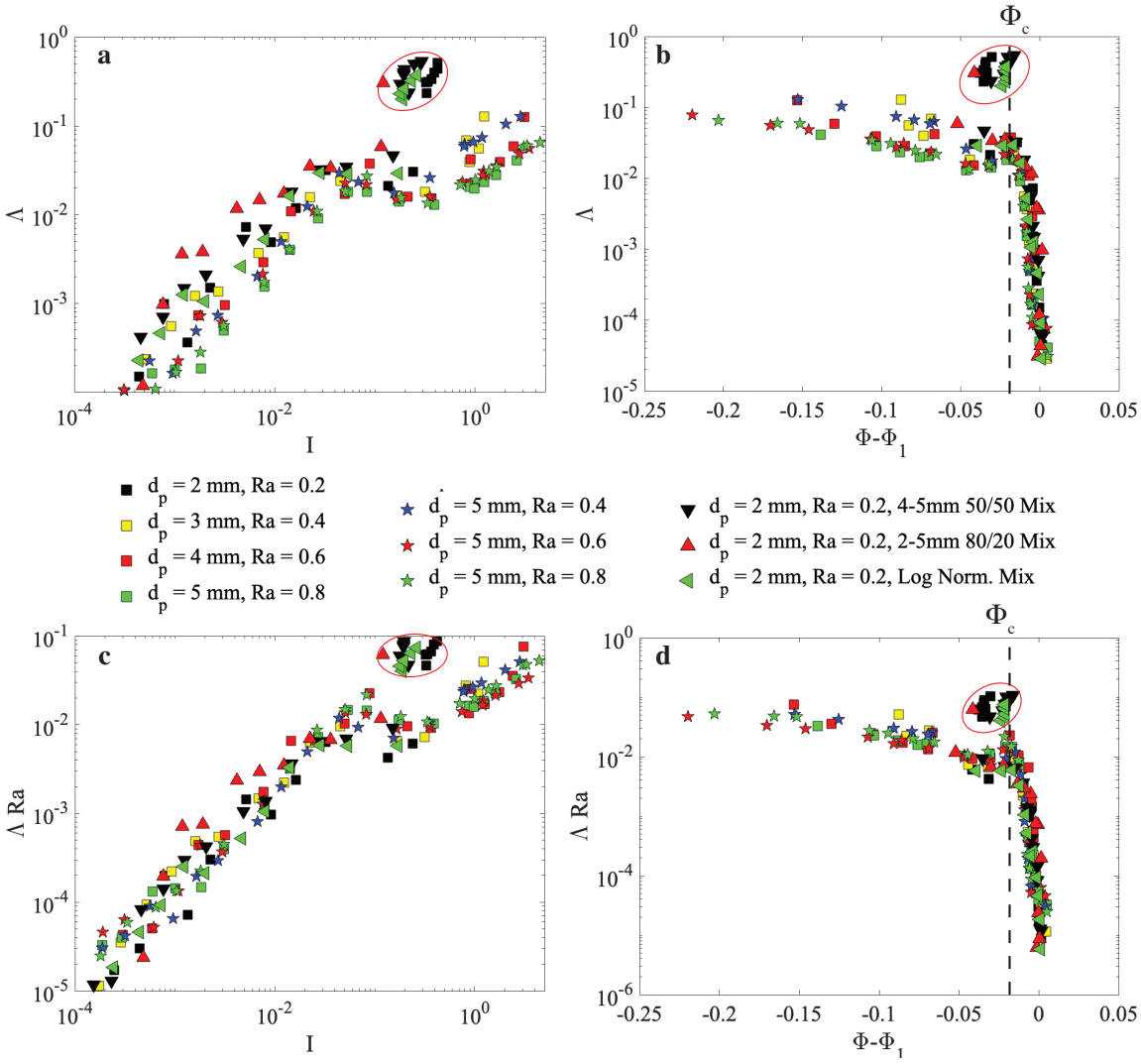

Figure 20. Non-dimensional basal force fluctuations Λ as a function of I (a) and the difference in solids concentration from the steady-state quasi-static max packing $\Phi - \Phi_1$ (b). (c) and (d) mirrors (a-b) but scales Λ by the averaged basal roughness Ra.

stream-wise velocity (a parameter we have shown to be sensitive to basal roughness, Figure 17a) shows how much of the poor scaling with inertial number is due to changes in basal roughness and, in turn, slip conditions, though there exists a region where it appears that Ω is sensitive to not only the average roughness value Ra, but how the rough base is constructed (Figure 21c). Recall that all type S2 simulations have the same basal roughness values, and yet we observe a consistent increase in Ω for fines-enriched mixtures (Figures 21b,d). Figure 21e combines type S1 and S2 simulations

and shows that there is good agreement among most of the simulations—aside from the fines-enriched mixtures—once coarse-grained velocities are greater than 10^{-1} (or when bulk inertial numbers are greater than 10^{-2}).

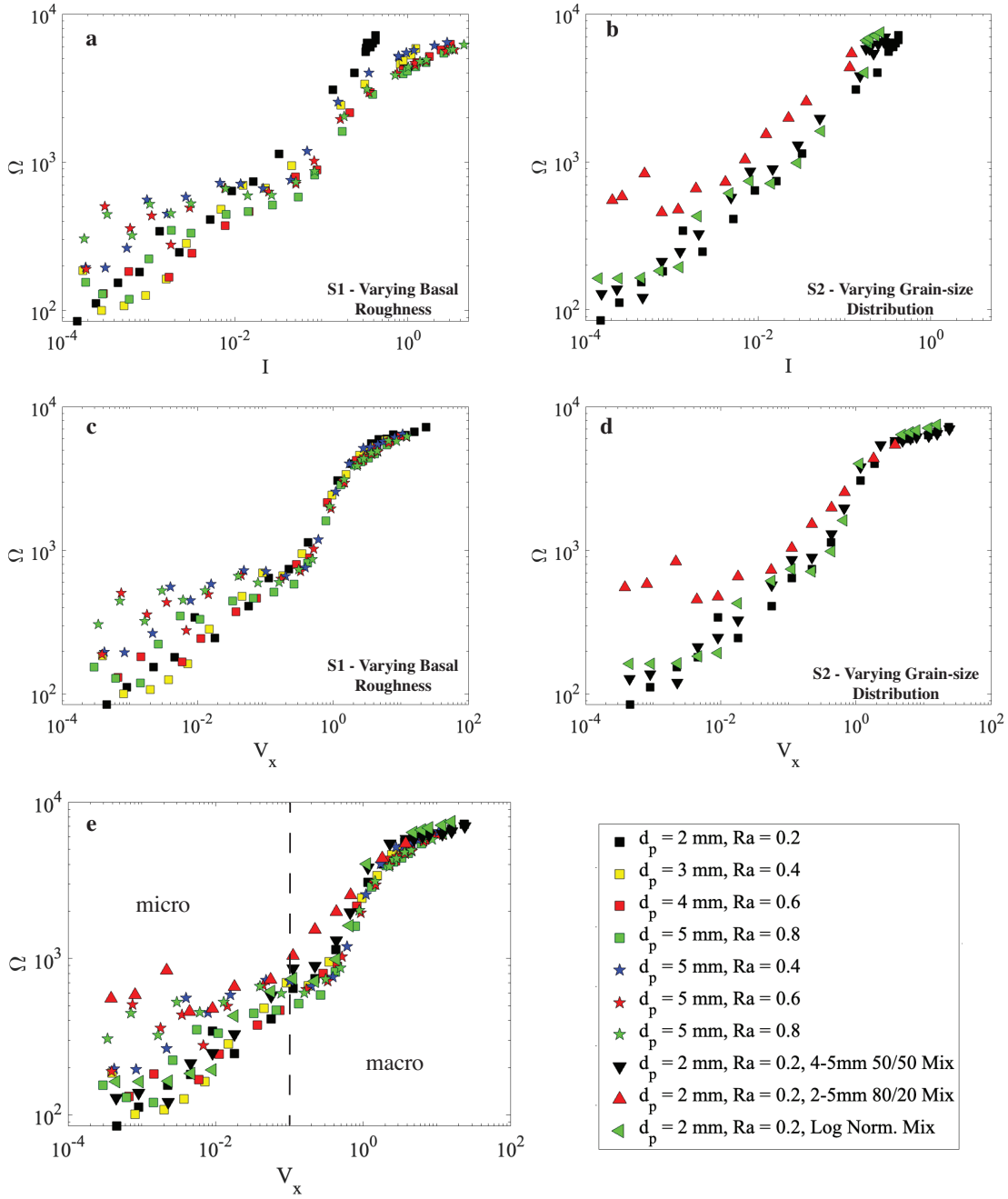

Figure 21. The radius of gyration Ω in the basal force power spectral densities as a function of I for type S1 simulations (a) and type S2 simulations (b). Ω as a function of the averaged stream-wise velocity V_x for type S1 (c) and type S2 (d). (e) Combined data of Ω as a function of V_x. Dashed line in (e) denotes when assemblages have bulk inertial numbers $I \geq 10^{-2}$

3.4 Discussion

Here we will start our discussion by separately considering the rheological and kinematic effects of varying the basal roughness and grain-size distribution. Then, we will discuss the controls on the basal force distribution. We will end the discussion by using the observed basal force signals as source functions to model one-dimensional (1-D) surface-wave propagation in a uniform medium.

3.4.1 Rheology and Kinematics

3.4.1.1 S1: Basal roughness effects on geometric friction and shear localization

We have shown that basal roughness directly contributes to setting the static friction coefficient μ_1 in the bulk (Figure 16a). This is rather intuitive: the 3-D generalization of the constitutive law proposed by Jop et al. [2006] (Eq. 4.5) enforces a yield criterion such that the mixture will flow only when the Drucker-Prager-like condition $|\tau| > \mu_1 P$ is met. Therefore, as μ_1 decreases with decreasing basal roughness, thereby decreasing geometric friction, the yield criterion decreases. This point is further illustrated by the engineered debris flows at the USGS flume in Blue River, Oregon, USA. Prior to September 2001, the bottom of the flume was a smooth, broom-finished concrete. With this boundary condition, workers were able to develop dry granular flows on an incline of $\sim 30°$. In September 2001, bumpy tiles were placed in the bottom of the flume and dry granular flows were no longer able to propagate to the bottom of the channel [Logan et al., 2018].

Bharathraj and Kumaran [2017] explore the effects of changing basal conditions on dense granular flow rheology in free surface inclined-plane flows. They show that there exists a critical basal roughness that leads to a discontinuous transition from an ordered (referred to above as crystallized) to disordered flow, with the transition being independent of slope angle. Similarly, a rapid transition from disordered to ordered flows is observed (e.g., circled region in Figure 17a-b), though this is dependent on the shear-rate, not just the composition of the rough base plate. Once flows become ordered—or, using our terminology, crystallized—Bharathraj and Kumaran [2017] show that mean particle velocity can increase up to an order of magnitude, which agrees with our markers of crystallization and plug flow. In contrast to Bharathraj and Kumaran [2017], we do not just see a discontinuous increase in particle velocity once flows crystallize, we also observe a gradual increase in velocity, within the bulk, before crystallization (Figure 17a). Moreover, as basal roughness decreases, such that

$Ra \leq 0.4$, the velocity profile transitions from linear to Bagnold-like, with the degree of shear localization increasing with decreasing roughness. In this way, the increase in the globally defined coarse-grained velocity with decreasing basal roughness is not only due to increases in velocities at the flow-substrate contact, but also a result of shear localization.

High degrees of shear localization can lead to a density inversion in high speed inclined-plane flows resulting in a 'supported' flow regime where a dense core is supported by a dilute, high granular temperature, boundary layer [Taberlet et al., 2007, Holyoake and McElwaine, 2012, Brodu et al., 2015]. To our knowledge, we present the first data that suggests such flow states are achievable in plane-shear configurations: as the basal granular temperature increases to nearly two orders of magnitude greater than the internal granular temperature, the global concentration Φ, stream-wise velocity V_x, and internal granular temperature T increases. As such, the supported regime described by previous efforts is the crystallized regime circled in preceding figures. The most interesting property of these crystallized-supported flows is that the effective basal friction μ_w weakens to well below static values, but this does not lead to a similar decrease in internal friction μ, but rather an increase (Figures 18g and 16e). Campbell [1989] suggests that the presence of such an agitated boundary layer could decrease the effective basal friction and may explain enhanced runout distances observed in geophysical granular flows. Similarly, bench-top experiments have shown that the Heim's ratio H/L (where H is the vertical elevation of the flow source and L is the runout length) decreases in the presence of these supporting boundary layers [Li et al., 2025]. While data presented in Li et al. [2025] may suggest that the boundary layer is indeed a source of the enhanced runout distance, it is important to note that their agitated boundary layer develops when the particle size increases relative to basal roughness elements, which we show here is necessary for shear localization and the ultimate development of a highly agitated boundary layer, but will also decrease geometric friction thus allowing a flow to propagate further down slope (recall our the analogy to the engineered flows by the USGS above). Further, Taberlet et al. [2007] force the development of this agitated boundary layer by imposing an initial particle velocity then allow the flow to arrest on a horizontal surface. The authors find that the dense core behaves frictionally much like a solid block and calculate an effective sliding friction coefficient. They report that this friction value does not weaken below the particle friction, and remains on the order

of 0.4, inline with the static friction μ_1 for our simulations with relatively smooth substrates. Therefore, it is not clear that the decrease in basal friction, caused by shear localization and the development of a high granular temperature boundary layer, can indeed lead to an increase in the runout distance of natural flows.

In summary, we see that basal roughness directly sets the static friction coefficient μ_1 in granular flows, with decreasing roughness decreasing μ_1 and leading to increased averaged velocities for a given inertial state. Moreover, relatively smooth substrates lead to shear localization that increases the disparity between internal fluctuating energy and basal fluctuating energy as measured by the granular temperature, which becomes exacerbated as flows crystallize and become supported by a highly agitated boundary layer that reduces the effective basal friction. This has implications for flows that traverse disparate reaches that may have non-uniform basal roughness, which will directly impact the partitioning of energy, not only in terms of bulk mean kinetic energy and fluctuating energy, but also in the internal architecture as shear localization can lead to drastic increases in internal heterogeneity, potentially providing a fluctuating energy source. Moreover, the link between bulk frictional values and basal friction must be closed in order to understand the role an agitated boundary layer might have on runout distance and bulk flow dynamics. Therefore, we suggest that there is a need for the careful development of both bench-top and numerical experiments to further elucidate the role this supported regime has on granular-flow runout distance, separating the effects of increased mobility due to a lowered static friction, induced by decreasing basal roughness, and the effects of a decrease in basal friction from particle agitations.

3.4.1.2 S2: Increased granular temperature generated through enriched-fines content

In S2 simulations, where we vary the grain-size distribution, we see that bulk properties like the static friction μ_1 and domain averaged velocity V_x remain relatively unchanged (Figures 16b,e and 17b, respectively). Nevertheless, packing efficiency increases due to an enriched fine-particle content (red triangles, Figure 16d). Jing et al. [2021] shows that large particles will segregate in the direction of shear gradients. As such, when there is a broader particle size distribution, as simulated by the bidisperse 2–5 mm mixture, large particles are advected towards the base of the flow, caused by shear localization induced by the relatively smooth substrate. This process decreases the packing efficiency and leads to a divergence in the dilation

response compared to the other simulations (Figure 16f). This segregation ultimately aids the development of an agitated boundary layer as larger particles dominate the population of particles in contact with the rough bottom plate, thereby decreasing the scale roughness. This is evidenced by the increasing basal granular temperature to internal granular temperature ratio T_w/T with inertial number (Figure 18h, red triangles). Coarse-particle segregation in the direction of shear gradients occurs in natural flows and is thought to be the leading cause of coarse-particle advection to the front and sides of dense granular flows, resulting in non-uniform morphologies such as coarse-grained fronts and self-channelization through levee formation (e.g., Johnson et al. [2012], Kokelaar et al. [2014]). It would be interesting to consider such a system in a gravitational field to observe the competition between reverse grading caused by kinetic sieving, and normal grading caused by advection towards shear gradients. If large particles are able to advect to the base of natural flows, when shear localization is present, this could lead to a positive feedback where large particles continue to move towards the base of the flow, decreasing the effective roughness and thereby increasing shear localization and heterogeneity in the vertical energy distribution. Inverse grading during transport ultimately yields lateral grading evidenced by coarse-grained levees [Johnson et al., 2012]. Therefore, shear localization, induced by relatively smooth substrates, may affect the timescale for levee-grain size segregation.

Heterogeneity in the vertical distribution of fluctuating energy is observed in all simulations with a mean basal roughness of $Ra \leq 0.4$, or when velocity profiles become Bagnoldian rather than linear (e.g., Figure 18h). Nevertheless, the fines enriched assemblages are particularly interesting because they also show an increase in internal energy fluctuations measured by their coarse-grained granular temperature, compared to their bidisperse and polydisperse counterparts with the same basal roughness (Figure 17d). Meanwhile, as discussed above, the internal friction measured in type S2 simulations is only marginally affected by changes in grain-size distribution: there is only a slight decrease in μ, up to 5%, when $I \leq 10^{-3}$ (Figure 16b). This is rather puzzling. Kim and Kamrin [2020] suggests that increases in granular temperature can cause divergence from classic $\mu(I)$ relations, specifically causing μ to decrease to values less than the static friction coefficient. The authors show that rescaling μ by the dimensionless granular temperature $\Theta = \rho_s T/P$ collapses data from a variety of flow configurations onto a single curve. As such, decreases in μ below μ_1 are met with increases in Θ. Nevertheless, Figure 17d shows an increase in granular temperature

and no sign of friction weakening. We can further test this view by plotting Kim and Kamrin [2020]'s proposed scaling (Figure 22). Note that, to remain consistent with the data presented in [Kim and Kamrin, 2020], we slightly change our definitions of granular temperature, solids pressure, and friction, to match those defined by the authors, and plot values for each grid cell within the simulation domain (see Figure 22 caption for details). Figure 22 is consistent with observations in Section 3.3.1; the bulk friction coefficient measured in type S2 simulations remains relatively unchanged while there is a marked increase in granular temperature. Breard et al. [2024] shows that scaling Kim and Kamrin [2020]'s $\mu(\Theta, I)$ relation by Φ^{-2} is required to collapse data derived from assemblages with disparate size mixtures (Figure 22b). This suggests that there is an intrinsic link between the granular temperature and the increase in packing fractions as a result of the increase in fine-particle ratios. The fact that the increase in granular temperature presented here does not 'heat' the material, and thereby decreasing the shear strength of the material, suggests that it is not a true 'excess', but that granular temperature is intrinsically tied to flow concentration, as suggested by kinetic theory [Jenkins and Savage, 1983, Lun et al., 1984]. Regardless, this exercise suggests that Kim and Kamrin [2020]'s $\mu(I, \Theta)$ relation needs to be further modified for flows with wider grain-size distributions and shear localization due to changing slip conditions prior to integration into continuum frameworks for modeling natural flow phenomena.

We can further consider the partitioning of fluctuating energy by recalling that Figures 17e-g shows that the ratio of fluctuating to average kinetic energy is directly affected by changes in basal roughness and grain-size distribution, but these changes are brought about by two opposing processes; T/Vx^2 decreases with decreasing roughness due to increases in the averaged particle velocity, while granular temperature remains unchanged, and T/V_x^2 increases with fines content because the average particle velocity is unchanged, while granular temperature increases. The increase in granular temperature can be attributed to the increase in the number density of 'rattlers', or particles that play a diminished role in the evolving contact network. In jammed states, rattlers are particles that are not in mechanical equilibrium—i.e., contact forces are not balanced resulting in mechanical instability [Behringer and Chakraborty, 2018]. As such, force chains, or quasi-linear features that concentrate the bulk of internal stresses, are predominantly supported by the largest particles in the system [Nguyen et al., 2015]. This view can be extended

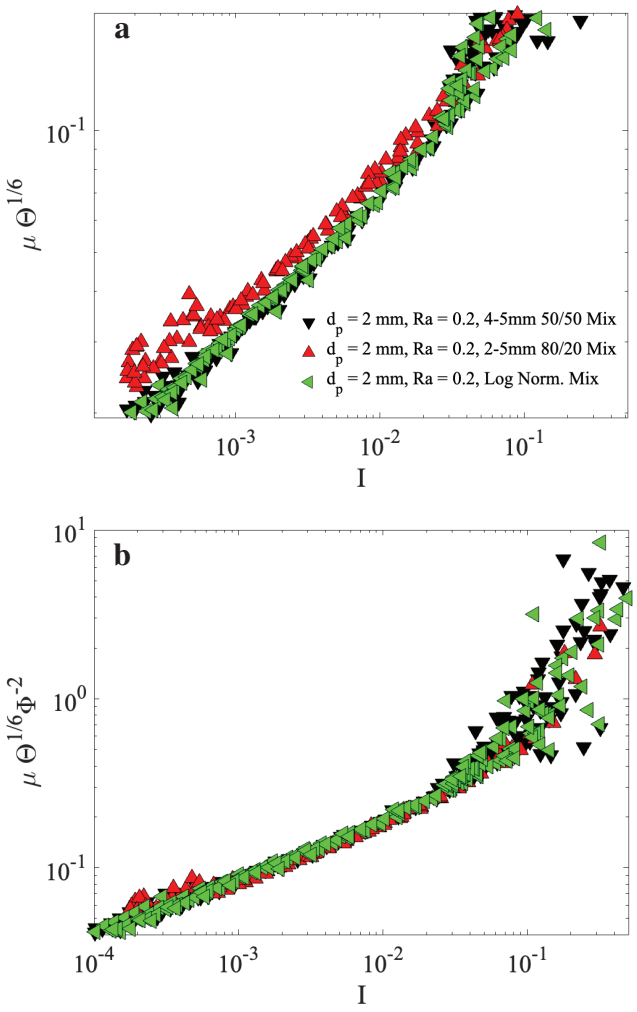

Figure 22. (a) $\mu(I, \Theta)$ scaling proposed by Kim and Kamrin [2020] for type S2 simulations. (b) $\mu(I, \Theta, \Phi)$ scaling proposed by Breard et al. [2024]. Note that here we change the definitions of granular temperature to its stream-wise component, and the effective friction coefficient to $\mu = \sigma_{xy}/P_y$ to remain consistent with [Kim and Kamrin, 2020]. Here, rather than plotting the global average of these values, we plot the local value derived from each coarse-graining grid cell.

to yielding states where force chains become more dynamic structures that bend, buckle, and collapse with shear [Tordesillas et al., 2011, Estep and Dufek, 2012]. In agreement with [Nguyen et al., 2015], we observe that an increase in the number of fine particles results in larger, less probable, contact forces, resulting in a more heavy tailed fluctuating velocity distribution (Figures 23a and 23c, respectively), with the heavy tail being enhanced by the fine-grained particle fluctuations (Figure

23e). As the inertial number approaches 10^{-1}, the 'excess' in T/Vx^2 relaxes and eventually converges with the other type S2 simulations. This is reflected in the force and velocity probability distribution and is a reflection of granular temperature being predominantly a function of the shear-rate, rather than a function of contact dynamics [Campbell, 2006].

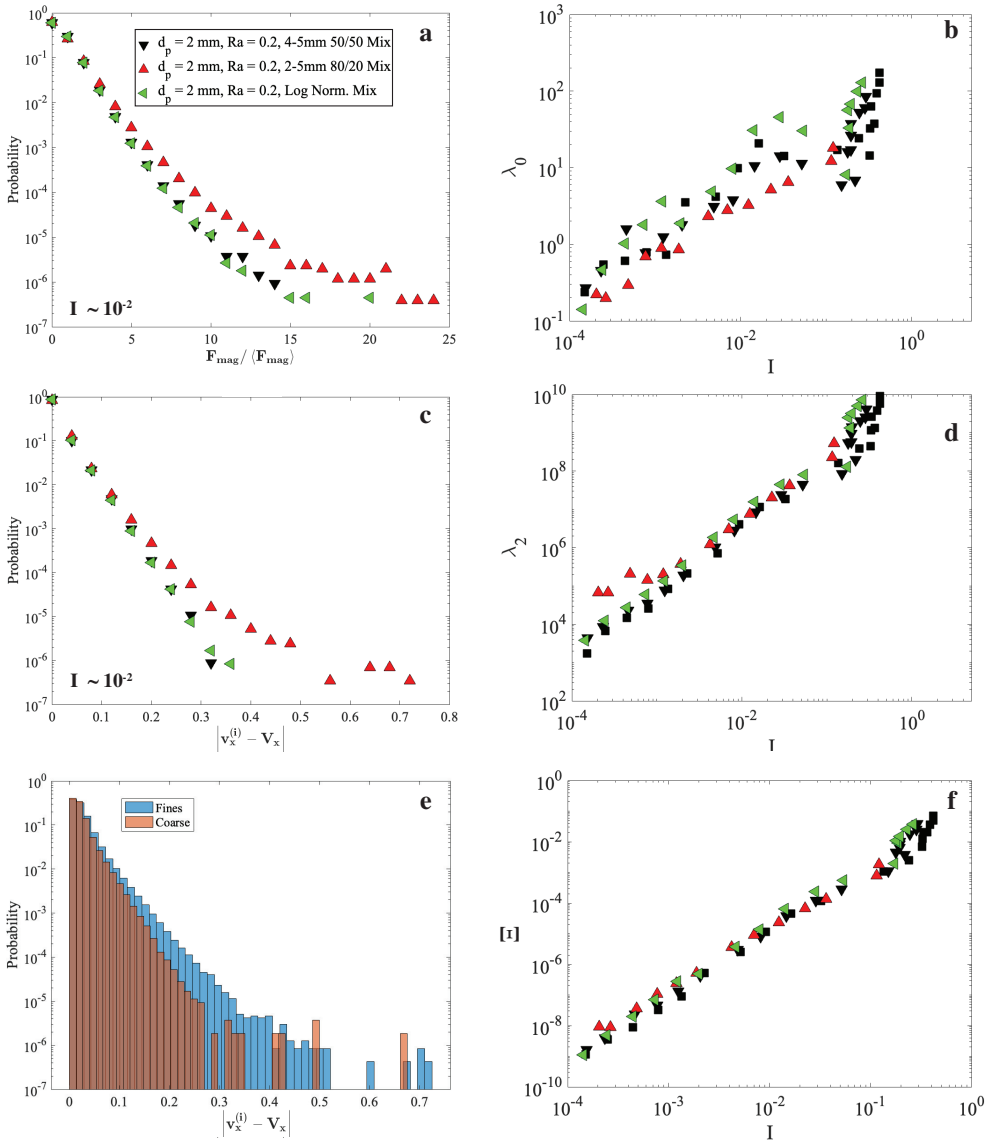

Figure 23. (a) The probability distribution of the magnitude of internal contact forces normalized by the average magnitude, for type S2 simulations with an inertial number $I \sim 10^{-2}$, (b) the zeroth moment of the basal-force power spectral density λ_0 as function of I for type S2 simulations, (c) the probability distribution of the magnitude of internal fluctuating velocities, for type S2 simulations with $I \sim 10^{-2}$, (d) the 2^{nd} moment of the basal-force power spectral density λ_2 as function of I for type S2 simulations, (e) the probability distribution of the fluctuating velocities for the fine (2 mm) and coarse (5 mm) particles from the fines enriched assemblage (5–2 mm 80/20 number mixture) with $I \sim 10^{-2}$, and (f) the dimensionless number $\Xi = \frac{\lambda_0^{1/2} T \rho_s}{P_s^2 d_{43}}$ as function of I.

To summarize, assemblages with an enriched fines content show a marked increase in their packing efficiency, but they dilate at a much more rapid rate with increasing shear rates due to coarse particle segregation caused by shear localization. This segregation can enhance a vertically heterogeneous energy distribution, especially when flows enter the collisional regime ($I > 10^{-1}$), and the basal roughness is sufficiently smooth to promote crystallization and the development of an agitated basal layer. Further, assemblages show evidence of an excess in granular temperature, compared to their more narrow grain-size distribution counterparts, though there appears to be no effect on the effective friction coefficient, counter to recent work by granular physicists. Regardless, the increase in granular temperature with an increased fines content implies that as a flow becomes enriched in fine particles, perhaps as blocks fragment as a flow propagates down slope, fluctuating energy at the base, as well as in the bulk, will increase. Shear localization will then dictate the ultimate fate of large particles, whether they are advected towards the front, side walls, or even towards the base of the flow depending on the competition of gravitational and shear-induced segregation. This is a rather important point to consider when posed in the context of depth averaged models that are agnostic to vertical fields. If coarse particles are advected towards the base of the flow, there can be a positive feedback where shear localization will increase and basal granular temperature will increase. In the following section, we will show that the redistribution of kinetic energy into particle fluctuations, implied by the increase in internal granular temperature, has a direct effect on the total power of the basal-force spectra, indicating that this may lead to a measurable signature of fines-enrichment in force-plate, and potentially, seismic signals.

3.4.2 Basal Force Spectra: a micro-macro transition and the redistribution of energy via internal energy fluctuations

We examine basal-force signals that result from varying basal roughness and grain-size distribution with a focus on the distribution of power measured by the radius of gyration Ω. Figures 19 – 21 show how basal force spectral characteristics are sensitive to changes in basal roughness and grain-size distribution. Using the non-dimensional variance Λ we show that the total power normalized by the mean basal force is sensitive to the roughness of the base plate (Figure 20). This sensitivity is a result of how the internal velocity structure transitions from linear to Bagnold-like as basal roughness decreases (Figure 17a). Despite this, we still observe distinct changes

in how Λ scales with the bulk inertial number and concentration, showing that the 'phase' transition from liquid-like to gas-like granular flows, suggested by our previous effort, is still recorded. This transition is representative of the fluctuating energy that is consumed by the destruction of the internal contact network, a necessary process for granular flows to enter into a regime where internal momentum exchange is driven by particle collisions. Figure 21a shows that the dispersion of power in frequency space Ω is not fully captured by the inertial number. When plotting Ω against the coarse-grained streamwise velocity V_x, we observe an improved scaling relationship for velocities exceeding 0.1 ms^{-1}. However, in fines-enriched assemblages, Ω continues to increase until velocities surpass 1 ms^{-1} (Figure 21e). Let us first consider the dispersion of data when $V_x < 0.1$ ms^{-1}.

Both type S1 and S2 simulations show rather poor scaling in the low velocity limit corresponding to $I \leq\sim 10^{-2}$. Notably, we observe that Ω is not only sensitive to the roughness parameter Ra, but also to the ordering of the base plate; when $V_x < 10^{-1}$ m/s data separates into roughly two fields, with the ordered rough plates (where $d_{ref}/d_p = 1$) having higher Ω values for a given velocity (Figure 21c). This suggests that dispersion in the basal force spectra is not solely sensitive to the average basal roughness Ra, but is rather sensitive to the nature of particle-scale contacts with the rough base. A similar trend is observed in type S2 simulations, where fines-enriched assemblages exhibit higher Ω values in the low-velocity limit. This behavior is attributed to bulk internal stresses being primarily carried by the coarse particles. As force chains buckle and collapse under imposed shear, microscale fluctuations propagate downward and reach the bottom plate. In this way, we observe a micro-to-macro transition, a transition away from a regime where individual basal roughness asperities, and micro-structure reorganizations, dominate the basal-force spectra into a regime where basal forces may be accurately described by macro-scale flow properties. This view of a micro-to-macro transition is supported by our previous effort that shows a $\Lambda(I)$ collapse in data generated by monodisperse simulations, both dry and submerged in an liquid fluid, when I approaches 10^{-2} (Zrelak et al. [2024]; Figure 10).

As flows reach this micro-macro transition, data across variable basal roughness conditions collapse, but we still observe an increase in Ω when assemblages are fines-enriched. This shows that the collective effects of fines-enrichment affects the mixture's macro-states, evidenced by the increase in bulk granular temperature and

the changes in internal energy partitioning (Figures 17d and 17f). It is noteworthy to recall that Ω is defined as the square of the ratio between the second (λ_2) and zeroth (λ_0) spectral moments (Eq. 3.14). Figures 23b,d show how the spectral moments from type S2 simulations vary with inertial number. The zeroth moment, or total power, exhibits a noisy scaling with inertial number, but shows a general decreasing trend as fines content increases (Fig, 23b). Meanwhile, the second moment is relatively unchanged (Fig, 23d). Noting that the zeroth moment decreases with increasing granular temperature, we use dimensional analysis to define a new dimensionless parameter Ξ

$$\Xi = \frac{\lambda_0^{1/2} T \rho_s}{P_s^2 d_{43}} \tag{3.16}$$

Figure 23f presents this dimensionless parameter as a function of inertial number for type S2 simulations and effectively collapses the data. This suggests that the decrease in power is directly related to the increase in granular temperature due to fines enrichment, providing a physical picture of flow driving energy being redistributed into fluctuating energy within the bulk.

3.4.3 1-D Seismic Signal Forward Modeling

One motivation to understand the relationship between basal tractions, assemblage properties, and flow dynamics is to understand what information can be extracting from seismic signals. To help bridge this gap we follow Tsai et al. [2012], Gimbert et al. [2014], and Farin et al. [2019] in using one-dimensional surface wave Green's functions to model seismic wave propagation through a uniform medium. Given a force-time function $F(t)$ the frequency domain ground velocity recorded at a station located at a distance r is given by

$$\dot{u}(f,r) = 2\pi i f \tilde{F}(f) G(f,r) \tag{3.17}$$

where $\tilde{F}(f)$ is the Fourier transform of the the force-time function, and $\tilde{G}(f)$ is the transform of the displacement Green's function [Aki and Richards, 2002, Tsai et al., 2012]. The Green's function is an approximation of surface-wave propagation through a 1-D structure, with a vertical displacement from a force on the substrate in the j^{th} direction given by

$$\tilde{G}_{jy}(f,r) = N_{jy} \frac{k}{8\rho_0 v_c v_u} \sqrt{\frac{2}{\pi k r}} e^{-\pi r f/(v_u Q)} \tag{3.18}$$

where k is the wave number and N_{jy} are dimensionless numbers with values $N_{yy} = 0.6$, $N_{xy} = 0.8 cos\psi$, $N_{zy} = 0.8 sin\psi$, with ψ being the source-station azimuth [Gimbert

et al., 2014]. We follow Gimbert et al. [2014] and use a solid rock density $\rho_0 = 2500$ kg/m^3, a quality factor $Q = 20$, and a functional relationship between the phase and group velocities v_c and v_u: $v_c(f) = v_{c0}(f/f_0)^{-\xi}$ and $v_u(f) = v_c(v)/(1+\xi)$, with $v_{c0} = 2175$ m/s, $f_0 = 1$ Hz, and $\xi = 0.48$. Our goal is to use basal-force time series generated by our DEM simulations as the source $\tilde{F}(f)$ in Eq. (3.17). Conceptually, this means that we simulate steady-state flow in a 100 m long channel using a series of point forces, representing the integral of basal forces over the rough base plate area $x_{plate} \times z_{plate}$, r meters from the receiver (Figure 24a). The total power spectrum of the observed ground velocity is then expressed as the sum of contributions from forcing components in the x, y, and z directions, as well as the sum of point forces in the channel

$$P_R^{tot} = \sum_{m}^{M} \left| 2\pi f \sum_{j}^{x,y,z} \tilde{F}_{jy}(f) \tilde{G}_{jy}(f, r_m) \right|^2 \tag{3.19}$$

In this way we calculate ground velocity spectra for all of our simulations, varying the receiver's distance from the channel r_0 from 3—100 m.

Previous efforts have used this approach to model seismic signals generated from particles in river transport and particle impacts associated with debris-flow transport [Tsai et al., 2012, Farin et al., 2019]. While [Farin et al., 2019] models a source, in-transit, with an internal morphology similar to what is observed in natural flows (i.e., a saltating front, a coarse snout, and a concentrated body), we assume a steady-state and uniform source. Nevertheless, one important difference is that we relax the assumption that granular tractions arise from uncorrelated forcings in space. Modeling seismic noise generated via uncorrelated forcings is a good first-order approximation, but may only be an accurate illustration of basal forces when attempting to model the highest frequency basal-force signals related to individual particle-collisions with the substrate, or when flows have inertial numbers that near the collisional limit [Zrelak et al., 2024]. By using basal forces generated over our entire modeling domain, though rather small when compared to the foot-print of real-world flows, we no longer assume that forces are solely generated by individual particle-substrate interactions, but rather collective motion that occurs on the scale of our shear-cell. This is important because we have shown that it is not the highest frequency basal forces that record bulk rheologic changes, but rather intermediate bands of about 1-100 Hz. This allows us to evaluate how recorded spectra may

be used to make assessments on the inertial state of the flows, and ultimately, the rheology of the granular media.

We again employ spectral moments to characterize how the recorded spectra evolve as the receiver is moved from 3 to 100 m away from the channel; Figures 24b,d,f plot the radius of gyration of signals recorded by our simulated receiver Ω_R, and Figures 24c,e,g plot the recorded total power λ_{0R} (zeroth spectral moment) for type S2 simulations (where we vary the grain-size distribution) against the flow's bulk inertial number. Figure 24b shows that, in the near-field, the dispersion of power about the central frequency decreases to a global minimum as flows transition from the intermediate fluid-like regime to the gas-like collisional regime, with no clear variations depending on basal roughness, nor the grain-size distribution, up until flows on the relatively smooth substrates crystallize (circled markers). As the receiver moves to 10 m from the channel, we see a clearer picture of how Ω_R records changes in flow dynamics: in the quasi-static regime, Ω_R increases monotonically until flows start to deform continuously, as they are now in the liquid-like intermediate regime, at which point Ω_R decreases to a local minimum, though we observe that the fines-enriched assemblages do not display such a drastic change (Figure 24d). Ω_R increases again as flows enter into the transitional regime, representing the steady transition to a gas-like state, at which point Ω_R saturates. Moving the receiver to a distance of 100 m shows that many of the details correlating to regime change are lost, and we observe that Ω_R is a rather noisy increasing function of inertial number across all regimes (Figure 24f). The total power of the recorded signals λ_{0R} retains the observations we made in Sections 3.4.1.2 and 3.4.2, where fines-enriched assemblages have a consistent decrease in total power (Figures 24c,e,g). This feature remains independent of distance from the source, with the largest disparity between the log-normal and fines-enriched bidisperse distributions visible at the furthest distance from the channel (compare green and red triangles in Figure 24g). Nevertheless, this feature is dependent on the inertial state; in quasi-static inertial states, differences in the total power caused by varying the grain-size distribution is effectively filtered out at all distances explored here, until the flow enters into the continuously deforming intermediate state ($10^{-3} < I < 10^{-1}$). However, engineered debris-flow experiments conducted by the USGS have estimated Savage number values of $N_{Sav} \sim 0.1$, which yield equivalent inertial number values of $I \sim 10^{-2}$ [Iverson, 1997]. Therefore, we expect that differences in the total power recorded by seismic stations will be sensitive

to grain-size distribution effects in natural debris flows and perhaps concentrated pyroclastic density currents. These data show that the zeroth moment of recorded power spectra could be used to assess fines enrichment in real time.

Plotting the dispersion in recorded power spectra Ω_R with inertial number at various distances from the channel provides two salient results: (1) Ω_R does not show any systemic changes with basal roughness, indicating that frequencies encoding these differences are attenuated during the propagation phase, (2) the dispersion of power in spectra recorded in the near field (i.e., $r_0 = 3,\ 10$ m) reflects inertial regime changes, though these changes are occluded in off-channel observations (i.e., $r_0 = 3$ m) and more keenly reflected at intermediate distances (i.e., $r_0 = 10$ m). This is due to off-channel observations becoming relatively saturated in high-frequency energy, whereas the station placed 10 m from the channel isolates the relatively low-frequency, high power, bands that reflect bulk regime change (Figure 19). This point is further elucidated by the fact that, when the receiver is 10 m from the channel, fines-enriched assemblages do not show such a dramatic decrease in Ω_R as the flows enter into the transitional regime (Figure 24d), reflecting that fines enrichment works to attenuate low frequency signals that encode regime change (Figure 19d). It is important to remember that these results are qualitative in nature, as the length scales at which frequency bands will be attenuated will depend on the locality and substrate, thus this observation will be highly dependent on the Green's function. Nevertheless, this exercise can be done with various Green's functions, with the most useful being empirical Green's functions like the ones presented in Allstadt et al. [2020]. Using empirical Green's functions in this exercise of utilizing forcings derived from first-principles simulations can aid in understanding the information that can be extracted from seismic signals, taking in consideration the path effects that will largely be dependent on the local geology, and informing the most optimal nodal or broadband deployments.

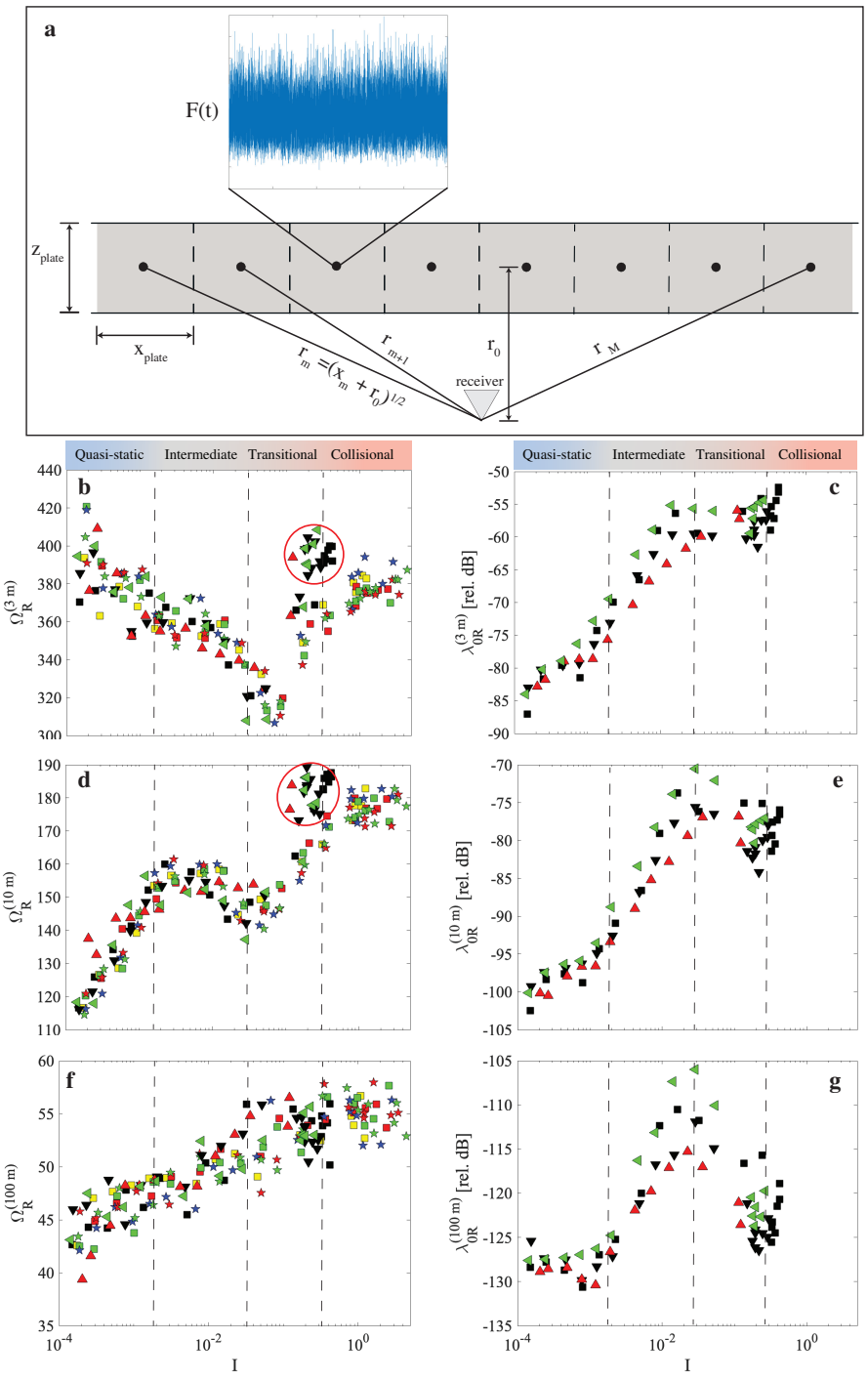

Figure 24. (a) One-dimensional surface- wave propagation calculation schematic with inset showing a basal-force time series derived from a DEM simulation. (b,d,f) radius of gyration of the observed seismic power spectra Ω_R as a function of I recorded 3, 10 and 100 m from the channel, respectively. (c,e,g) the zeroth moment of the observed power spectra λ_{R0} as a function of I recorded 3, 10 and 100 m from the channel, respectively.

3.5 Conclusions

In the present study we show the effects of basal roughness and grain-size distribution on granular rheology and how this is ultimately reflected in the basal force distribution. This effort aims to further develop the findings presented in Zrelak et al. [2024] by acknowledging that natural flows span a wide range of basal roughness conditions and grain-size distributions. The simulations presented here are not meant to be exhaustive but rather a first-order examination of the role these parameters play in affecting the partitioning of energy within granular systems, and the implications for modeling and monitoring.

We find that basal roughness plays a key role in setting the static friction and controlling the onset of shear localization. As roughness decreases, localization becomes more pronounced. In the collisional inertial regime ($I > 10^{-1}$), the smoothest substrates promote a crystallized flow structure, where a dense, ordered plug is supported by an agitated basal layer that lowers the apparent wall friction. Surprisingly, internal energy fluctuations measured by the granular temperature is unaffected by basal roughness. Increasing the proportion of fine particles within the granular mixture has little effect on the effective friction coefficient or the mean flow velocity. However, it leads to a noticeable rise in the internal granular temperature.

To assess how changing basal-roughness conditions and grain-size distributions affect basal-force signals we use the method of spectral moments to examine how the distribution of power is affected by these parameters. We find that the dispersion of power Ω has a sensitivity not only to the average basal roughness, but also to how the roughness elements are constructed when flows have inertial numbers of $\leq\sim 10^{-2}$. We relate this to a micro-to-macro where individual particle-substrate contacts, or asperities, as well as microscopic fluctuations in the internal particle-contact structures, directly affecting the basal-force distribution. Additionally, we show that while increasing fines content raises the granular temperature, it does not alter the bulk shear strength of the assemblage—as suggested by previous studies—but instead redistributes flow-driving energy into internal fluctuations, thereby reducing the total power transmitted through basal forces.

Finally, we conduct a series of 1-D surface wave propagation calculations to evaluate which features of the basal-force signals persist during transmission. Using spectral moments, we find that the dispersion of power in the recorded seismic spectra, Ω_R, exhibits distinct scaling behavior with inertial number, indicating its

potential as a diagnostic tool for tracking flow state. However, measurements taken off-channel, using receivers placed 3 meters from the source, are dominated by high-frequency energy. As a result, transitions in flow regime are not easily detected. This underscores the importance of receiver placement when using seismic signals to infer the inertial state and bulk rheology of the flow. Stations located too close to the source may be saturated by high-frequency noise. Furthermore, the total power, represented by the zeroth spectral moment, recorded at various distances from the channel, retains the power reduction observed in basal-force signals as fines content increases. This suggests that spectral moments may also be useful in monitoring changes in relative fines content during flow propagation. Using DEM-derived basal-force signals in combination with empirical Green's functions provides a promising framework for optimizing future seismic deployment strategies.

CHAPTER IV
(GRANULAR) MATTER AND MEMORY

4.1 Introduction

In 1991 Pierre-Gilles de Gennes won the Nobel Prize in Physics for his efforts that led to the the formation of what is now referred to as soft-matter research. In his Nobel Prize lecture, de Gennes states that soft-matter has two properties: complexity and flexibility [de Gennes, 1992]. Complexity here refers to soft matter's macroscopic behavior not being solely a function of the properties of constituent parts comprising the system. Instead, collective effects lead to emergent phenomenon. Soft matter displays flexibility in multiple ways. First, soft matter is flexible in that they can behave elastically upon loading. This form of elasticity is in contrast to hard-matter atomic particles: the force needed to deform a soft-matter particle is orders of magnitude less than a 'hard' atomic particle; [Frenkel, 2002]. Second, flexibility refers to the fact that soft matter has 'large response functions' when external forcings or stimuli are introduced [de Gennes, 2005]. One of de Gennes' favorite examples is the vulcanization of rubber: sap extracted from the hevea tree responds to the addition of sulfur thereby undergoing a state change from a liquid-like polymer (latex) to solid rubber. Further examples of soft matter are colloids, liquid crystals, particle-fluid systems, and granular materials.

The Earth's surface is dominated by granular materials that provide the supply for mass transport phenomena—or geophysical flows—that shape the landscape. Geophysical flows take the form of, for example, landslides, debris flows, rock avalanches, and pyroclastic density currents. These particle-fluid systems with their variable admixtures of fluid-solid concentrations and dynamic coupling between the two phases display enigmatic emergent properties. These properties are exemplified by the appearance of yield stresses [Houssais and Jerolmack, 2017], shear-rate-dependent rheologies [Guazzelli, 2024], aging and glassy dynamics [Ferdowsi et al., 2018], and jamming [Liu and Nagel, 2010]. All of these properties typify soft-matter materials [Nagel, 2017].

A simple but profound feature of soft-matter is the excluded-volume effect. This can be simply described as the volume that a particle cannot occupy, because another particle already occupies said volume [Caglioti et al., 1997]. This process leads to the emergence of effective friction, even in the absence of material friction [Peyneau and Roux, 2008]. Jerolmack and Daniels [2019] express excluded volume effects as a

process that prohibits states that require two particles to overlap. This provides a condition on the energy landscape of possible metastable states a granular system can occupy. As a state is forced by some energy input, for example surface deformation, the energy landscape shifts with the geologic landscape. This change in the energy landscape can be enough to perturb a granular system out of its metastable state, thus being transported until it is able to find a more stable state, e.g., an energy minima provided by a valley floor. This process is true for any disordered, out-of-equilibrium system, and, importantly, is what allows for the formation of memory [Keim et al., 2019].

Memory in granular materials can take many forms. Vanel et al. [1999] report that the stress distribution in static sand piles is a function of how they were built. A more dynamic example is given by sheared particle-suspensions and dry granular material 'recalling' the most recent direction in which the assemblage was driven [Gadala-Maria and Acrivos, 1980, Toiya et al., 2004]. Moreover, granular materials can 'self-organize' under repeated shear cycles, meaning that particle's will dynamically explore the landscape of possible states (positions), ultimately finding positions that comply with the driving force [Ren et al., 2013]. This processes allows the material to store a memory of the shear amplitude under which the material had reached a steady state. Similarly, [Paulsen et al., 2014] show that particle suspensions can be 'trained' by shearing until the system reaches a steady state. As a shearing cycle is restarted, the system will be unperturbed until strain amplitudes become greater than that of the training cycle. Galanis et al. [2022] report that granular beds preconditioned by an overlying hydrodynamic shear flow encode memory about both the amplitude and the direction of the flow; granular beds are strengthened under hydrodynamic shear such that the Shields number, or the dimensionless shear stress required to initiate particle motion, increases. When the direction of the overlying shear flow is reversed, after preconditioning the bed, the Shields number decreases.

The forms of memory described above suggests that geologic deposits composed of unconsolidated sediments can encode memories of past flow states, emplacement mechanisms (i.e., how the deposit was built), and post-deposition reworking. All of these factors work in tandem with the physical properties of the granular material to define the sate of metastability as a deposit resides on a slope. It is important to consider that these deposits can act as sources for future geologic hazards as the geologic landscape evolves, and energy landscape is perturbed. For example, the

3 June 2018 eruption of Fuego Volcano (Guatemala) produced a complex series of pyroclastic density currents that inundated the surrounding area [Naismith et al., 2019]. Data suggests these flows were, in part, derived from perched tephra deposits built from previous eruptions 2–3 years prior [Charbonnier et al., 2023, Risica et al., 2022]. It is interesting to consider that such complete retrogressive failure of the perched deposits might give some indication about the metastability of these piles. Here we use idealized discrete element methods (DEM) to explore how the stability of granular assemblages on time-varying slopes is affected by previous flow history and emplacement processes.

4.2 Methods

We model three-dimensional dense granular flows using the Department of Energy solver MFiX-DEM [Garg et al., 2012]. Assemblages are composed of greater than 37000 particles. The assemblages are nearly monodisperse, with an average diameter $d = 5$ mm. We model particle contacts using the linear-spring-dashpot contact model with an elastic coefficient $k_n = 2 \times 10^5$ Pa m. Table 3 gives a summary of simulation parameters.

Simulations are composed of three phases. First, the particles are randomly distributed between two rough and bumpy plates composed of 5 mm particles. We then prepare the assemblage by shearing it with a prescribed top-plate velocity and constant confining pressure, while the bottom plate remains static through all time. The first phase ends once a steady-state is reached, with the steady state being defined by the average particle velocity over a second interval being within 5% of the average velocity in the interval prior. The second phase is defined by one of two 'emplacement' pathways: (1) we allow the particle assemblage to come to a rest by linearly decreasing the top plate velocity to zero or (2) we instantaneously set the top plate velocity to zero. Once the particles come to rest (or when particle velocity fluctuations decay to values less than 10^{-8} m/s), we begin the third phase by removing the top plate and rotating the gravity vector to simulate a 15° slope. The particle assemblages are held on this slope for 1 s, allowing particles to adjust to the new slope orientation, then the gravity vector is rotated at a rate of 0.5°/s. This form of destabilization allows us to examine how particle assemblages react to time varying shear forces imposed by the rotating gravity vector. Rotating gravity, and thus increasing the slope angle, allows us to impose an effective friction coefficient μ. This process can be thought of as simulating a system where the effective friction coefficient increases until the

assemblage fails. Note that this form of gradual destabilization is not likely in nature, but it does provide a view of how assemblages may respond to changing conditions that will ultimately weaken the material and lead to bulk failure, such as excess pore pressure [Breard et al., 2020, 2022]. Figures 25a-b show curves representing assemblage-driving histories (i.e. top plate velocities in phases 1 and 2). Figure 25c-e depicts snapshot renderings of an assemblage in each simulation phase.

During the first preparation phase, we export particle positions, velocities, and contact forces at a frequency of 100 Hz. We coarse-grain (CG) this data using methods outlined in Fullard et al. [2019] and Breard et al. [2020], following the technique developed by Weinhart et al. [2013]. This allows us to derive fields which we integrate to express, for example, the domain-averaged effective friction coefficient $\mu = |\sigma^D|/P_s$, using the two-dimensional magnitude of the deviatoric shear stress $\sigma^D = \sigma^{(2D)} - 0.5tr(\sigma^{(2D)})$ and three-dimensional solids pressure $P_s = 1/3tr(\sigma)$. Further we use the CG method to calculate the domain-averaged inertial number $I = d\dot{\gamma}/(P_s/\rho_s)^{-1/2}$, where d is the average particle diameter, $\dot{\gamma}$ is the shear rate, P_s is the 3-D solids pressure, and ρ_s is the solid particle density. This process is repeated as the assemblages approach failure during the third phase.

After the emplacement phase, and when particle fluctuations diminish, we export particle-contact data during this static state to aid in classifying the static assemblages prior to placing them on a slope. We calculate the mobilization index M_I

$$M_I = \frac{|F_t^c|}{\mu_p F_n^c} \tag{4.1}$$

where F_t^c is the tangential particle-particle contact force, F_n^c is the normal contact force, μ_p is the particle friction coefficient, and the superscript c refers to particle-contact forces. The mobilization index is typically used to calculate the proportion of particles that are mobilized due to saturation of the Coulomb failure (sliding) criterion: $|F_t^c| = \mu F_n^c$ [Behringer and Chakraborty, 2018]. Therefore, contacts with M_I values equal to one are considered mobilized contacts. Furthermore, contact orientations are used to construct the fabric tensor A

$$\mathbf{A} = \frac{1}{N_c}\sum^{N_c} \mathbf{n}_{ij}\mathbf{n}_{ij} - \frac{1}{3}\mathbf{I} \tag{4.2}$$

where N_c is the number of contacting particle pairs, $\mathbf{n}_{ij}$ is the unit vector pointing to the centers of particle-contact pairs i and j, and $\mathbf{I}$ is the identity tensor. We focus our analysis on the the components A_{12}, quantifying the degree of anisotropy in the shear direction [Ness and Sun, 2015].

Authors have shown that the density of vibrational modes $D(\omega)$ exhibits an excess in low-frequencies as granular assemblages approach yielding states [O'Hern et al., 2003, Silbert et al., 2005, Wyart, M., 2005, Owens and Daniels, 2013, Brzinski and Daniels, 2018]. The transition from a static pile to a yielding flow can be analogized to a second-order phase transition, with the low-frequency modes acting as harbingers of the onset of plasticity through collective motions [Tanguy et al., 2010]. Dickey and Paskin [1969] and Keyes [1997] use molecular dynamics simulations to relate the Fourier transform of the velocity auto-correlation function to the density of modes. We follow these authors and use the particle velocities in the third phase, on approach to failure, to calculate the velocity auto-correlation function C_v

$$C_v(t) = \sum^{N} \frac{\mathbf{v}_i(t) \cdot \mathbf{v}_i(t+\tau)}{\mathbf{v}_i(t) \cdot \mathbf{v}_i(t)} \tag{4.3}$$

where N is the number of particles, τ is the lag time, and $\mathbf{v}_i$ is the velocity of the i^{th} particle. The density of modes, in time, becomes

$$D(t, f) = \int^{\infty} C_v(t) cos(2\pi f t) dt \tag{4.4}$$

where the frequency f replaces ω [Owens and Daniels, 2013, Brzinski and Daniels, 2018]. We use this measure to help quantify the state of the assemblages as they approach failure. This also allows us to test how the density of modes might be used to help classify the onset of bulk failure.

Table 3. Summary of particle parameters and simulation setup..

parameter	*variable*	*value*
Particle Parameters		
diameter [m]	d	$0.005 \pm 5\%$
density $[kg\ m^{-3}]$	ρ_s	1050
angle of repose [°]	θ_s	≈ 21
particle friction coeff.	μ_p	0.53
restitution coeff.	e_n	0.6
normal elastic coeff. $[Pa\ m]$	k_n	2×10^5
normal dissipation coeff. $[kg/s]$	η_n	$\frac{2\sqrt{m_{eff}k_n}\lvert ln\ e_n\rvert}{\sqrt{\pi+ln^2 e_n}}$
tangential elastic coeff. $[Pa\ m]$	k_t	$0.2k_n$
tangential disspation coeff. $[kg/s]$	η_t	$0.5\eta_n$
Simulation Parameters		
domain size $[m]$	$X \times Y \times Z$	$40d \times \geq 20d \times 40d$
confining pressure[1] $[Pa]$	P_p	2000
top plate velocities[1] $[ms^{-1}]$	V_p	$0.5 - 5$
inclination angle[2] [°]	θ	$15 - 25.5$

[1] Phase 1: Preparation
[2] Phase 3: Destabilization

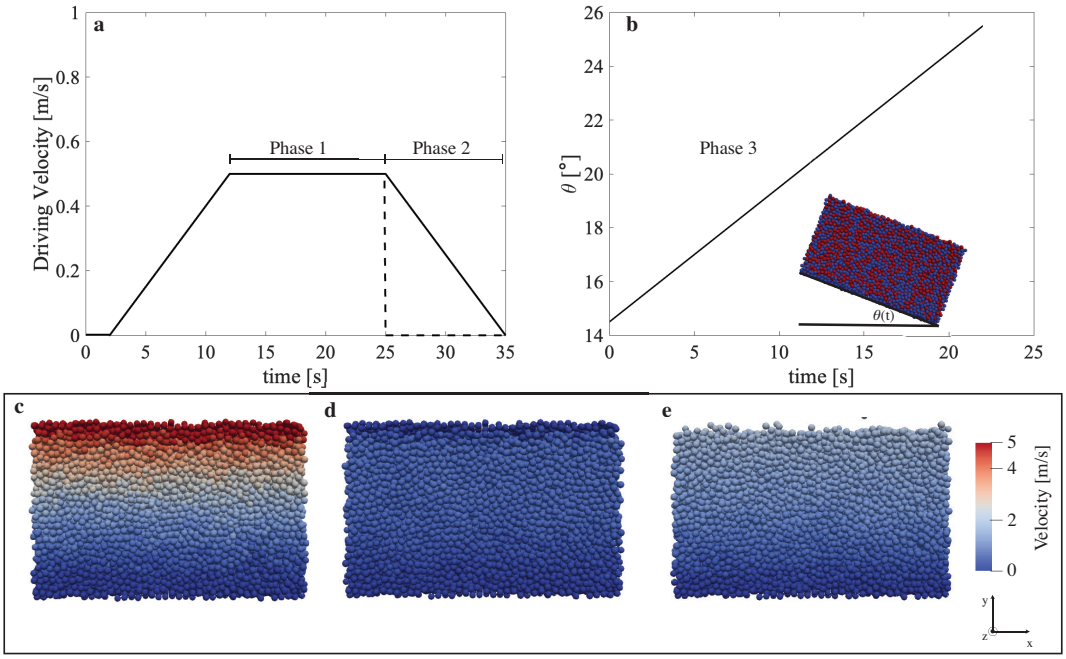

Figure 25. Organization of simulation procedures. (a) Driving history during Phase 1 and emplacement pathways defining Phase 2. Solid line denotes the driving history when the top-plate velocity is linearly decelerated to zero, and the dashed line represents when the top-plate velocity is instantaneously set to zero. (b) Slope angle versus time during Phase 3. (c-e) Snapshots of simulation phases: Phase 1 (c), Phase 2 with instantaneous top plate deceleration (d), and Phase 3 (e).

4.3 Results

We will start by describing the rheology of the mixtures as they are prepared in the plane-shear configuration. Figures 26a-b show the coarse-grained (time and domain-averaged) effective friction coefficient μ and the solids concentration Φ as a function of inertial number I. We fit theses two parameters with empirical functions [Jop et al., 2006, Amarsid et al., 2017, Breard et al., 2024]

$$\mu(I) = \mu_1 + \frac{\mu_2 - \mu_1}{1 + I_0/I} \tag{4.5}$$

$$\Phi(I) = \Phi_1 - \alpha I^{\gamma} \tag{4.6}$$

where μ_1 and Φ_1 are the static friction coefficient and the quasi-static max packing, respectively. All other fit parameters are presented in Figures 26a-b. Further, we plot A_{12} to show the relationship between particle-scale anisotropy and the macroscopic state during preparation (Figures 26c-d). Ness and Sun [2015] show that negative A_{12} values represent a particle fabric that opposes the shear flow, while $A_{12} = 0$ represents an isotropic fabric. We see that the fabric becomes increasingly anisotropic with increasing shear rate, or with decreasing concentration (Figure 26c and 26d, respectively). This aligns with a view that contact dynamics become more anisotropic as flows enter into the collisional regime (i.e., $I \geq 10^{-1}$), leading to anisotropic kinetic properties [Campbell, 2006, Zrelak et al., 2024].

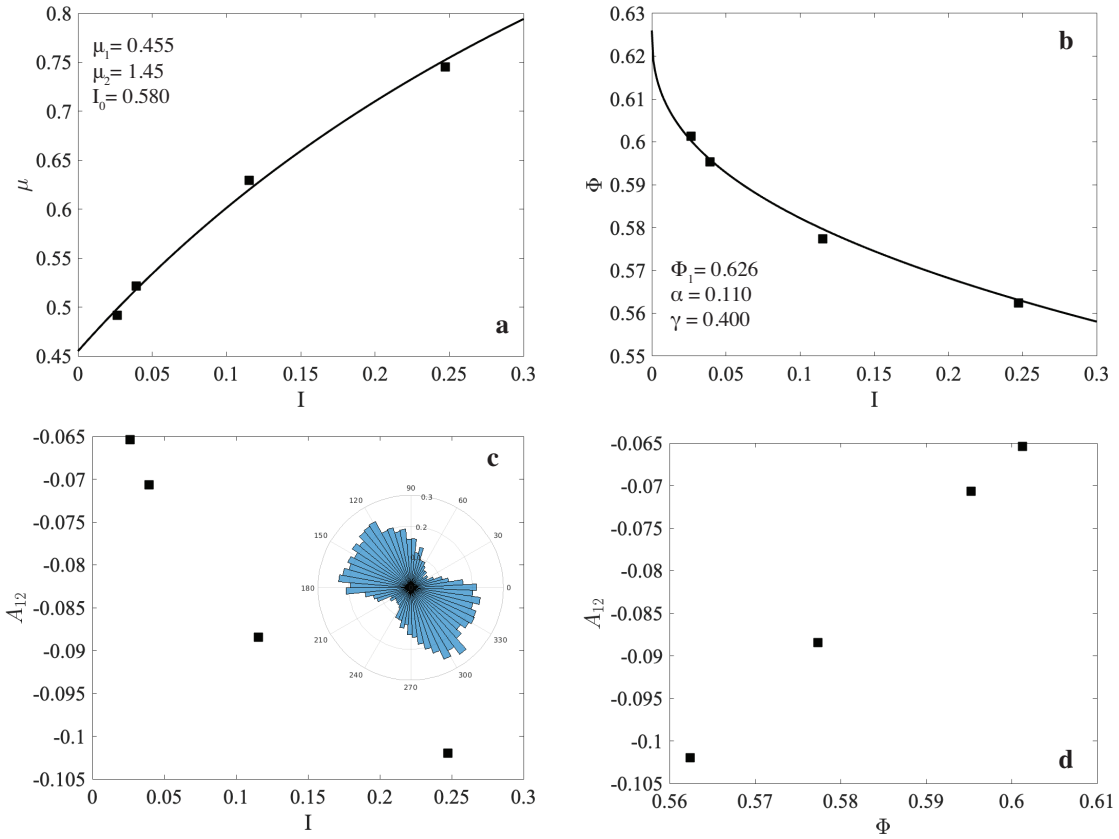

Figure 26. Domain-averaged (coarse-grained) effective friction coefficient μ (a) and concentration $\Phi(I)$ (b) as a function of inertial number I measured during the preparation phase. Black squares denote coarse-grained properties and solid lines depict fits from Eqs. 4.5 and 4.6. Particle-scale anisotropy, as measured by A_{12}, as function of I (c) and Φ (d). Inset in (c) depicts a rose diagram plotting particle-contact orientations in the x-y plane opposing the sheared direction for the case when $I \approx 0.25$.

Next, we present data classifying the static-state of the prepared assemblages, while comparing the prepared assemblages with an unprepared control assemblage that was settled but not prepared by plane-shear. Figure 27a depicts the mobilization index M_I probability density function for assemblages where the top-plate driving velocity is linearly decelerated to zero, while Figure 27b shows this for assemblages where the top-plate velocity is instantly decreased to zero (solid and dashed lines in Figure 25b, respectively). In general, M_I seems rather agnostic to the pathway to the static state, though two assemblages feature heavier tails compared to the other distributions. While the mobilization index does not show systematic variation with

past flow state and the emplacement mechanism, there are systematic changes in the solids concentration Φ with preparation flow history and emplacement pathway. Figures 27c-d display vertical profiles of the coarse-grained solids concentration Φ (averaged in the z-direction), showing that decreasing inertial numbers recorded during the preparation phase yield increasing solids concentrations in the static state. Similarly, the static-state concentration is dependent on the pathway to emplacement; the beds that are linearly decelerated to a resting position have higher and more uniform concentration profiles, while the instantaneously decelerated assemblages show more disorder and are less concentrated. Figure 27e drives this point further by depicting the domain averaged concentration as a function of the preparation phase inertial number. Figure 27f illustrates that regardless of the preparation phase inertial state, and the path to emplacement, particle-fabric anisotropy A_{12} generated under plane-shear conditions is lost. This reflects that particle-fabric anisotropy is intrinsically a function of particle concentration and shear-rate, thus as shear vanishes, particle contacts become isotropic.

In summary, the mobilization index M_I does not show systematic variations in reference to past flow states, nor in reference to the pathway to emplacement, though all of the distributions do differ from the control state, and there exist two assemblages with heavier-tailed distributions. Furthermore, anisotropy measured during the preparation phase is lost as shear vanishes, indicating that memory of the past amplitude of shear is not necessarily encoded in static-state particle contacts. Nevertheless, we see that the static-state packing, or solids concentration, is inherently tied to the history of the assemblage.

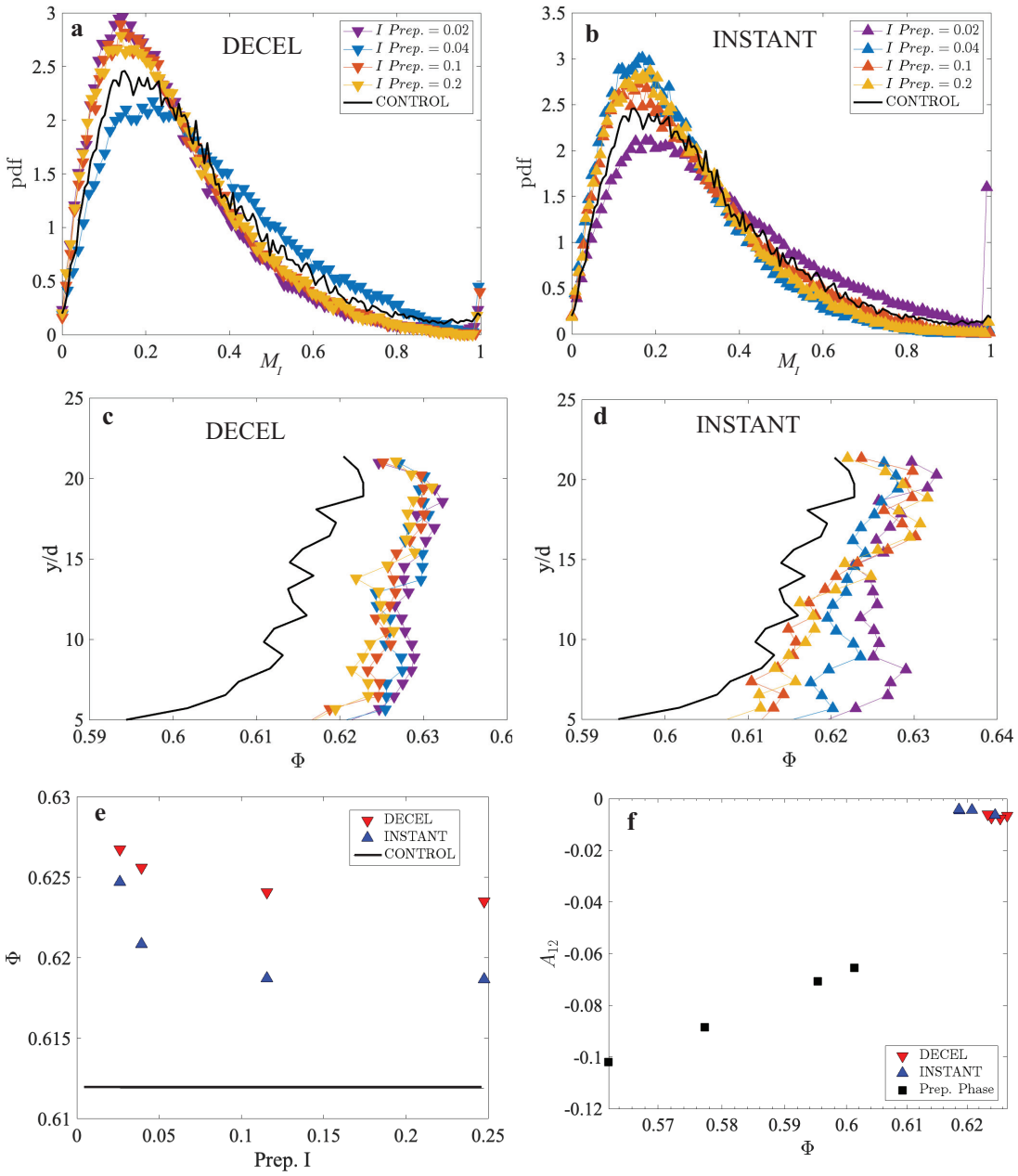

Figure 27. Characterizing the static assemblages. (a-b) probability density of the mobilization index M_I, (c-d) vertical profiles of solid concentration Φ (averaged in the span-wise direction), (e) solids concentration as a function of the preparation phase inertial number I, and (f) fabric anisotropy A_{12} as a function of domain-averaged solids concentration.

Now we present coarse-grained transient data for the last five seconds in simulation time as the prepared, and control, assemblages are placed on time varying

slopes. Figures 28a-b plots the stream-wise coarse-grained velocity as a function of slope angle θ, with a dashed line depicting when the coarse-grained velocity equals 0.005 m/s. We will use this value as a first-order estimate of bulk failure, as after this point all of assemblages are in a continuously yielding, accelerating, state. Figure 28a shows that the angle at which this velocity is reached decreases with the preparation phase inertial number, though there is hardly any differences between the assemblages with an inertial state of $I \approx 0.1$ and $I \approx 0.2$. Conversely, Figure 28b shows that when the top-plate velocity is instantaneously decelerated to zero, the two assemblages with preparation inertial numbers ≥ 0.1 do not meet, though they have reached a velocity of 0.005 m/s well before this time window. Figures 28c-d present the coarse-grained solids concentration Φ as a function of slope angle, with black stars plotted to illustrate the concentration of the assemblage when they have reached an average velocity of 0.005 m/s. The solids concentration shows that once velocities are greater than $\sim$ 0.005 m/s, the assemblages start to dilate rapidly past quasi-static values, aligning with the view that the flows are transitioning from a quasi-static state, where the concentration does not vary, to a continuously deforming media analogous to a liquid-like state [Forterre and Pouliquen, 2008]. In summary, Figure 28 shows that the angle at which an assemblages reaches a continuously yielding state is not only a function of the preparation phase inertial number, but also a function of the pathway to the static state: all of the assemblages in which the top-plate driving velocity was instantaneously set to zero reach this continuously yielding and accelerating state at lower slope angles. Furthermore, as the inertial number measured during the preparation phase increases, we see two effects that highlights the importance of the emplacement mechanism: (1) when the top-plate driving velocity is linearly decelerated, there appears to be diminishing returns in that increasing the preparation phase inertial number has no effect on how the assemblage fails; (2) when the top plate is instantaneously set to zero, increasing inertial states during the preparation phase does have an effect, such that curves approach convergence with the control assemblage on shallower slopes.

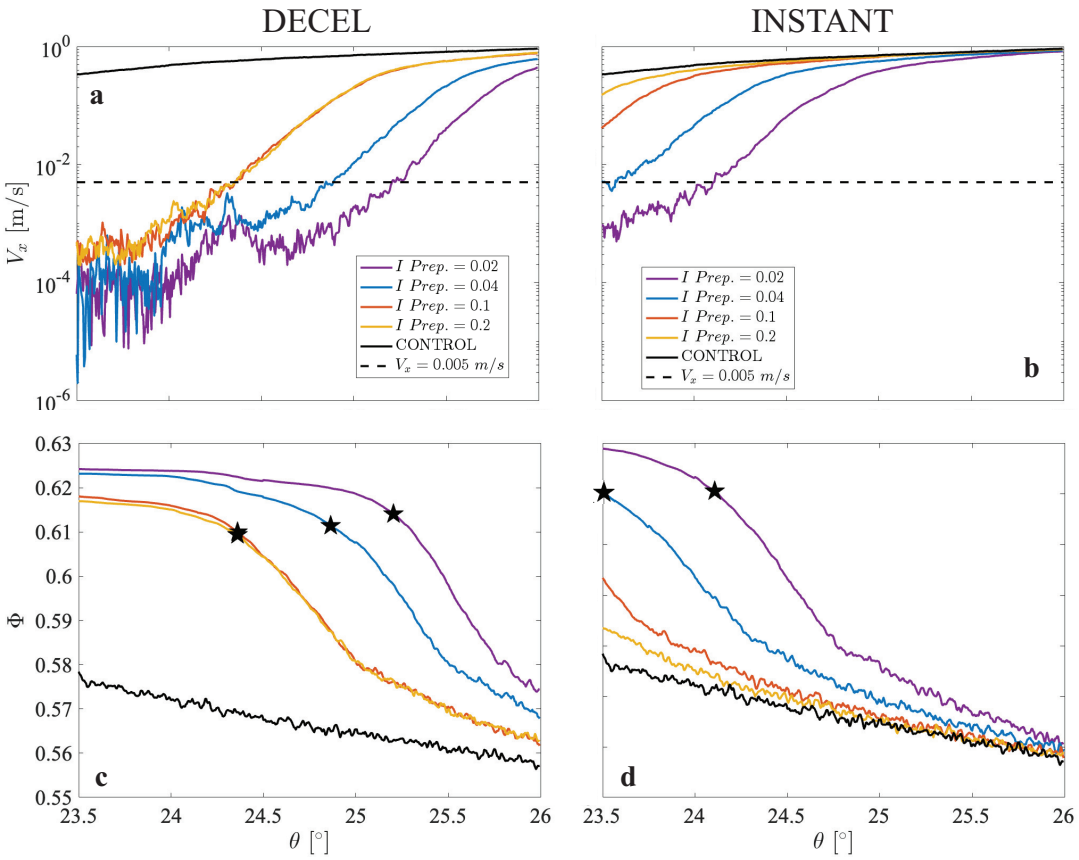

Figure 28. Domain-averaged velocity V_x (a-b) and solids concentration Φ (c-d) as a function of slope angle. Black stars in (c-d) indicate the slope at which $V_x = 0.005$ m/s.

To further probe the state of the material as it approaches failure, we use the velocity auto-correlation function to calculate the density of modes $D(f)$ Eqs. (4.3) and (4.4). Brzinski and Daniels [2018] show that the first moment of $D(f)$ decreases upon, and immediately after, yielding. Therefore, we calculate the mean frequency as

$$\langle f \rangle = \frac{\lambda_1}{\lambda_0} \tag{4.7}$$

where λ_n is the n^{th} spectral moment

$$\lambda_n = \int f^n D(f) df \tag{4.8}$$

When calculating Eq. (4.3) we keep a constant lag-time window size of 100 samples, therefore we restrict the density of modes calculation to slope angles $\theta = [23.5°, 25.5°]$. We focus our density of modes analysis on the the mean frequencies as they

vary with slope angle (Figures 29a-b). Note since assemblages that were emplaced via instantaneously decelerating the top-plate velocity to zero fail on shallower slopes, we do not observe the more dynamic variations in $\langle f \rangle$ that are evidenced in the linearly-decelerated assemblages. Figure 29a suggests there are two salient features in the mean frequency $\langle f \rangle$: (1) the mean frequency decreases and converges to a frequency of ≈ 8 Hz when assemblages are fully yielding and accelerating, and (2) fluctuations in $\langle f \rangle$ abruptly terminate prior to slope angles corresponding to averaged velocity equals 0.005 m/s. To isolate these two features, we apply a moving average with a window size of 50 samples to isolate the time-varying mean of $\hat{f}$ and use this to extract the fluctuating component $f^* = \langle f \rangle - \hat{f}$. Figure 29c shows this decomposition for the linearly decelerated bed with an preparation-phase inertial state $I \approx 0.2$. These features suggest that the density of modes can provide a better approximation for when the assemblages yield, and perhaps even providing a measure to assess the assemblages state as it destabilizes.

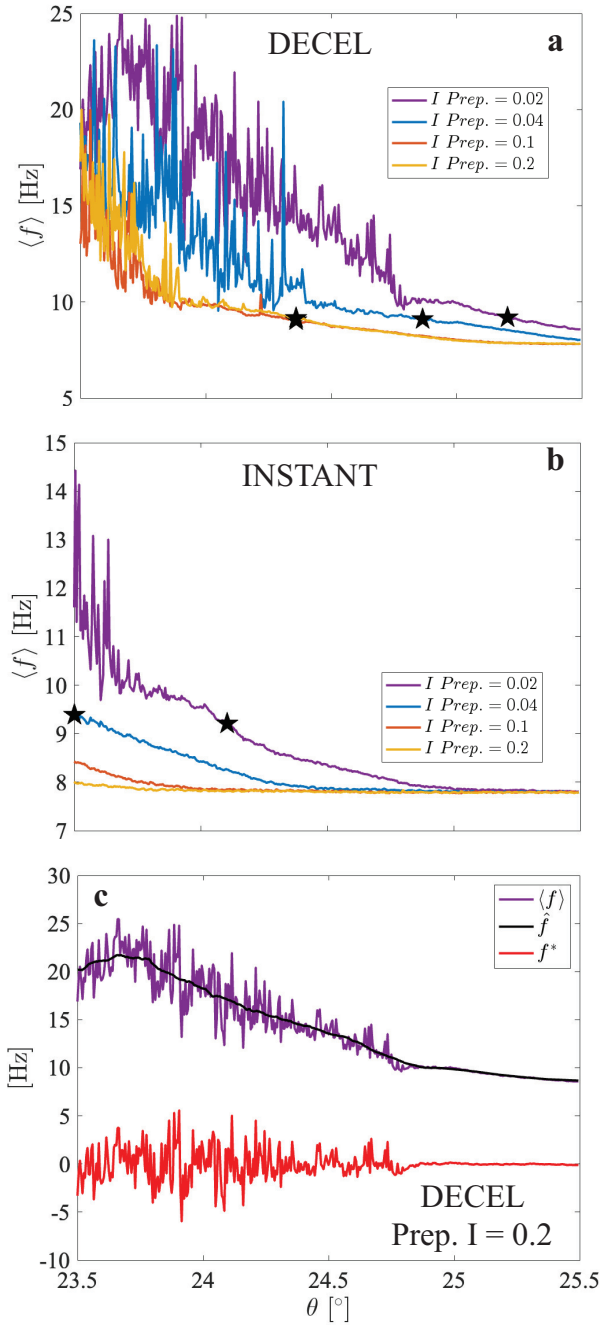

Figure 29. The mean frequency of the density of vibrational modes $\langle f \rangle$ (a-b) and its decomposition into mean $\hat{f}$ and fluctuating f^* parts, as a function of slope angle θ.

Comparing $\langle f \rangle$, along with its mean and fluctuating parts, against the domain-averaged velocity shows that these metric can help paint a picture of assemblage dynamics on the approach to failure. Figure 30 shows this comparison isolated to the

assemblage with a preparation inertial number $I \approx 0.2$, and that was emplaced by linearly decelerating the top plate velocity to zero (purple curves in Figures 28a,c,e and Figure 4.4a). Using these data, we identify three regions of interest labeled in Figure 30. The first occurs when $\hat{f}$ reaches a global maximum, after which it monotonically decreases with increasing slope angle. This corresponds with an increase in fluctuations f^*, as measured by the windowed standard deviation σ_{f^*} (Figure 30c), and an increase in V_x. It has been shown that collective motion leads to a decrease in the first moment of $D(f)$ [Tanguy et al., 2010, Brzinski and Daniels, 2018]. Therefore, increasing fluctuations f^* occurring with a decreasing mean suggests that the increase in collective motion is driven by unsteady particle rearrangements throughout the domain. As such, we identify this as the start of destabilization. The second region is defined by a decrease in the fluctuations from the mean. This occurs along with a slight decrease in V_x. Though the domain averaged velocity decreases we still observe a persistent decrease in mean frequencies. We suggest that this may be a signifier of imminent failure as velocity fluctuations become correlated in time. Finally, the third region is marked by a nearly log-linear increase in V_x, an abrupt decrease in the standard deviation of the fluctuations, and a limit like approach to a mean of $\approx$ 8 Hz, which we posit to be linked to the scale of the system. We denote this third region as 'true' bulk failure occurring at slope angles about a half a degree shallower than the first-order estimate using the arbitrarily defined threshold $V_x = 0.005$ m/s (black stars in Figure 30 and in preceding figures). This comparison suggests that the mean frequencies of the density of vibrational modes can not only be used to detect bulk failure, but may also be used to predict when failure is imminent.

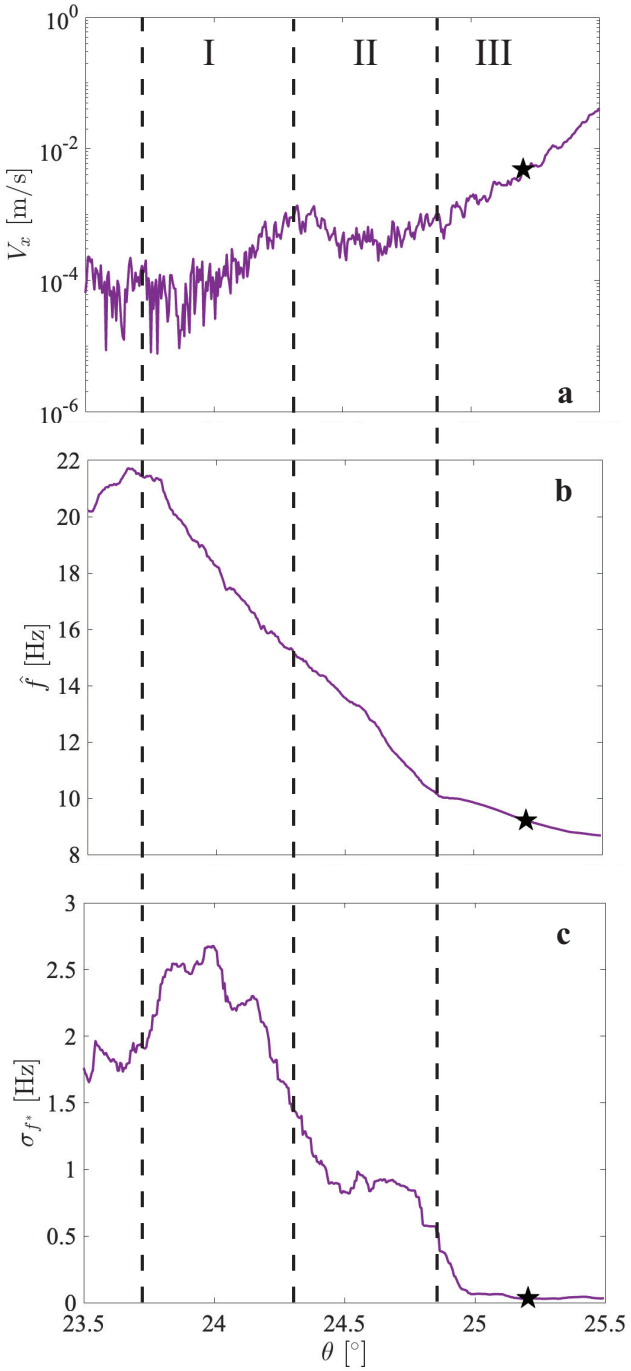

Figure 30. The mean frequency of the density of modes $\langle f \rangle$ (a-b) and the decomposition of $\langle f \rangle$ into mean $\hat{f}$ and fluctuating f^* parts (c). Black stars indicate the slope at which $V_x = 0.005$ m/s.

For our final analysis we will explore how the mean frequency $\langle f \rangle$ evolves with a range of conditions from destabilization to jamming. We isolate this exploration to a single assemblage with no preparation history. The setup is similar to that of the Phase 3 simulations above, gravity is rotated in time such that the effective slope linearly increases from 15° to 45°. Once the slope reaches 45°, the slope linearly decreases back down to 15°. In the context of geophysical systems, this can be envisioned as a system destabilizing due to a marked shift in the energy landscape, then arrests as it reaches, for example, a valley floor—a minima in the energy landscape. Figure 31a plots the coarse-grained stream-wise velocity, Figure 31b the effective friction coefficient μ and the tangent of the slope angle (left and right vertical axes, respectively), Figure 31c shows the domain-averaged coordination number Z and concentration Φ (left and right vertical axes, respectively); Figure 31d plots the inertial number with blue and red fields indicating quasi-static and failing states, respectively; Figure 31e shows the mean frequency of the density of vibrational modes $\langle f \rangle$, and Figure 31f the moving window standard deviation of $\langle f \rangle$, all as a function of time. Red dashed lines indicate when the assemblage fails, and dotted lines depict when the assemblage jams. We see that at early times, there are abrupt jumps in the average velocity, which corresponds with decreasing coordination number and increases in the inertial number. We denote these events as 'false starts', as the assemblage is reorganizing itself as the slope angle increases. It is important to note that these 'false starts' are not observed in Figures 31e,f. This shows that the density of modes is able to discriminate assemblage rearrangement events, or perhaps reorganization of the micro-states, from bulk failure. Furthermore, as suggested in Figure 30, we observe that bulk failure is preceded by a slight decrease in the magnitude of fluctuations from the mean frequency $\langle f \rangle$. As the slope angle is decreased, and the assemblage approaches jamming, both the mean frequency $\langle f \rangle$ and its fluctuations increases rather abruptly, nearly 10 seconds (or 4 °) prior to reaching a jammed state. Note that jamming occurs at slope angles less than that at which bulk failure occurs, a hallmark of hysteresis in granular media [MiDi, 2004]. Ultimately this indicates that if the velocity autocorrelation function can be calculated, both failure and jamming can be predicted.

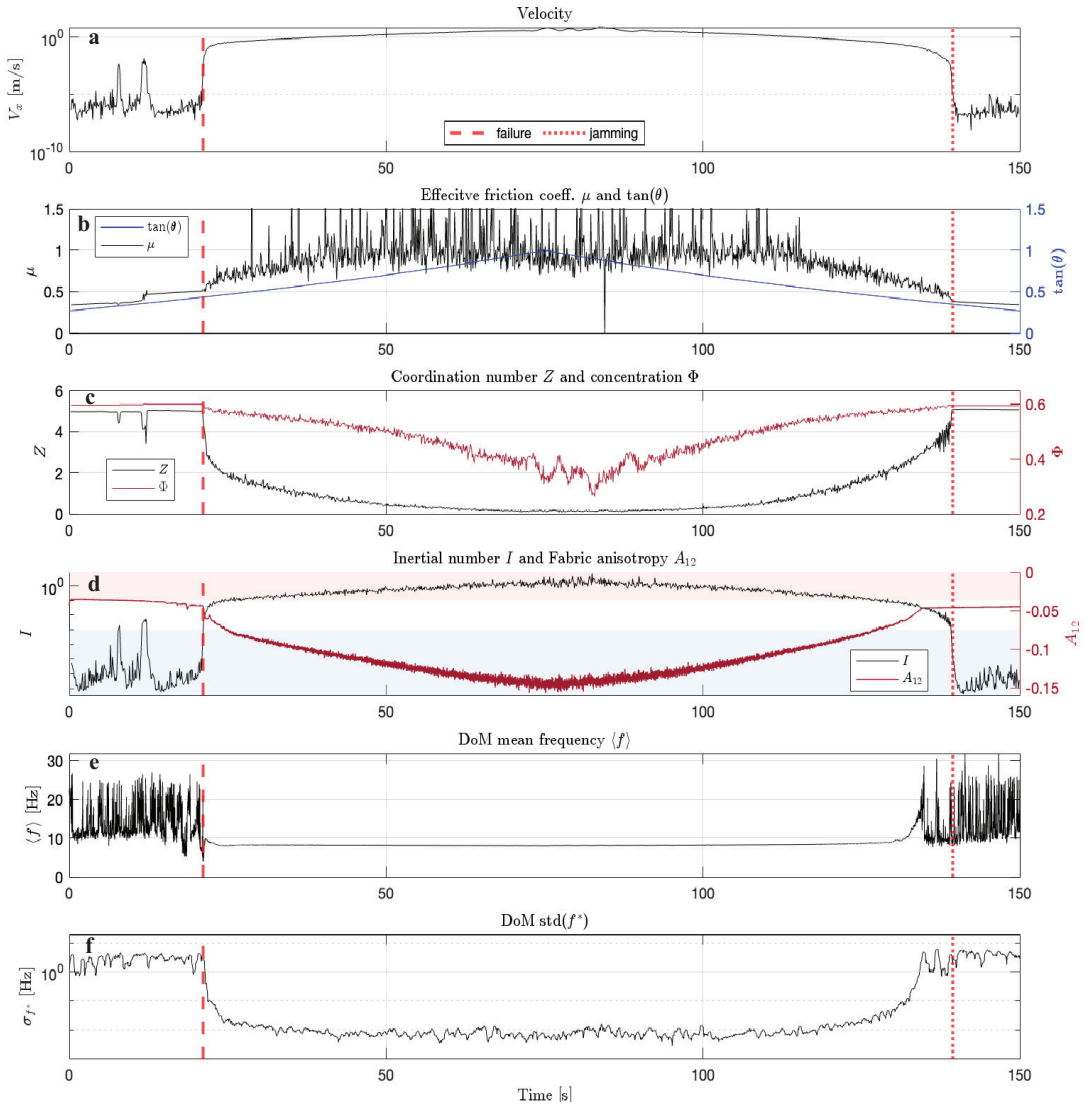

Figure 31. Kinematics of an assemblage on approach to failing and jammed states. (a) the domain-averaged velocity V_x, (b) the effective friction coefficient μ (black curve) and the tangent of the slope angle θ (blue curve), (c) the mean coordination number Z (black) and the concentration Φ, (d) the inertial number I (black) and particle-fabric anisotropy (red), (e) mean frequency of the density of modes $\langle f \rangle$, and the moving window standard deviation of the fluctuating part of $\langle f \rangle$ σ_{f*}, as a function of time.

4.4 Discussion and Conclusion

We have shown how the preparation of granular assemblages plays a direct role in determining the slope angle at which bulk failure will occur. We subjected assemblages to a preparation phase in which assemblages were placed in plane-shear

configurations and sheared to a desired inertial number. Then, the assemblages take one of two pathways to a static state. This allows for exploration in how emplacement processes might add to, or diminish, memory of past flow states. Figure 28 shows that kinematics of a pile on time-varying slopes are directly affected by the assemblages' history. When assemblages are emplaced via linearly decreasing the flow driving top-plate velocity to zero, increasing shear-rates in the preparation phase yields assemblages that fail on shallower slopes. Nevertheless, once the inertial number in the preparation phase approaches the collisional limit (i.e. $I \geq 10^{-1}$), there seems to be no added effect on the critical slope angle that yields bulk and continuous failure. Conversely, when assemblages are emplaced by instantaneously setting the top-plate velocity to zero, increasing shear rates during the preparation phase leads to ever-decreasing critical slope angles, such that the kinematics approach the control test case. Galloway et al. [2022] report data from experiments on dense colloids and suggest that memory is stored in the form of elastic contacts. From a granular perspective, this means that memory is stored in the form of force chains, as evidenced by the fact that the radial stress distribution in a sand pile is inherently a function of how it was built [Vanel et al., 1999]. As a flow reaches inertial states of $I \geq 10^{-1}$, prolonged particle-particle contacts and long-range correlations, in the form of force chains, are diminished, and the flow becomes a gas-like collisional flow [Zrelak et al., 2024]. The observation that decelerated assemblages with inertial number greater that 10^{-1} fail in very similar ways aligns with this view and suggests that the memory stored in assemblages that were once in the collisional regime is that of the emplacement pathway. As such, the material is similarly strengthened (relative to the control case) from further strain as the driving velocity linearly decelerates to zero.

When examining the microstructure of the static assemblages, we see that fabric anisotropy is lost as shear vanishes, and that the distribution of mobilized contacts does not help to explain why the assemblages fail at disparate slope angles. The main difference between assemblages with similar flow histories, but different emplacement pathways, is that the decelerated beds have systematically denser, and more uniform, packings. When the top plate velocity is allowed to linearly decelerate to zero, particles are strained such that the concentration approaches random close packing (i.e. $\Phi \approx 0.64$). If the top plate velocity is instantaneously set to zero, particles settle into more disordered and looser packings. The fact that the denser and more uniform

assemblages fail at steeper slope angles suggests that memory in the form of excluded volume effects plays a non-trivial role in setting the angle at which bulk failure occurs. This begs an analogy to configurational entropy in thermodynamic systems. Defining entropy in granular systems is a difficult processes. Asenjo et al. [2014] give an example of a granular entropy calculation in a two dimensional system comprised of 128 disks. They suggest that granular entropy is related to the probability of particle packings being near an energy minima that is represented by lattice positions. In this view, packings that approach random close packing may indeed have a higher probability of particles packings closer to these minima. Therefore, denser and more uniform packings (exemplified by our linearly decelerated assemblages) have metastable states that require larger energy inputs (i.e., steeper slopes) to promote bulk failure. As such, our results align with the conclusions presented by [Galloway et al., 2022], in that memory is stored in the form of configurational entropy.

We can extend the view that particle packings, and therefore flow history and emplacement processes, will have implications on the metastability of granular deposits by considering two aggradational end-members commonly attributed to geophysical-granular flows. Geophysical-granular deposits may be built via a process that spans a continuum from progressive aggradation to en-masse 'freezing' [Branney and Kokelaar, 2002]. Progressive aggradation suggests a deposit is formed via the deposition of particles in successive layers. In this way a deposit at any given location is a representation of the lower most portion of the flow. En-masse freezing is the processes whereby an entire plug flow freezes as flow-driving shear stresses vanish, and the deposit at a location represents the entirety of the flow structure. These two emplacement processes will necessarily have an effect on the configuration of particles in the static deposit, and thus will play a role in dictating the metastability of the pile.

A central question that remains is how to assess the metastability of a natural deposits, and can this assessment be linked to a configurational entropy that encodes the history of emplacement. Our final analysis performed on an assemblage approaching failing and jammed states suggests that the density of vibrational modes might hold the key to answering this question. We have shown that the density of vibrational modes can not only be used to define bulk failure, but may also provide signals that presage failure and jamming. Nevertheless, more effort is needed to interrogate the information encoded in the density of vibrational modes. This is

needed given the difficulty in computing entropy even in idealized systems, and it's near impossibility in natural systems. DEM provides an excellent opportunity to flesh out this approach. For example, DEM can be used to test whether the volume of a of failing assemblage is linked to the asymptotic mean frequency in the density of modes, and whether the decay in fluctuations prior to failure can help elucidate excluded-volume effects that lead to pinned particle-states prior to yielding. DEM could also be used to assess potential signals as an assemblage approaches failure through other means, such as progressively increasing pore pressure. Authors have shown that the density of vibrational modes can be extracted from acoustic measurements (i.e. Owens and Daniels [2013], Brzinski and Daniels [2018]), therefore we expect that acoustic sensors may give promising results for monitoring the stability of granular piles in nature. This exploration highlights how discrete element methods might be used to assess ways in which researchers can probe granular materials, perhaps giving rise to methods that use disparate active and passive wave fields to learn more about the metastability of natural deposits.

CHAPTER V
FUTURE OUTLOOK

In the preceding chapters, I present how discrete element methods (DEM) may be used to improve modeling and monitoring of natural geophysical granular flows. In Chapters 2, I described how basal force distributions can encode rich dynamical information, even under the null hypothesis of monodisperse assemblages and invariable roughness conditions. Chapter 3 relaxed this assumption by considering both bidisperse and polydisperse grain-size distributions, as well as variable basal-roughness conditions, and ended with 1-D steady-state surface-wave propagation, with results suggesting granular-flow regime changes may be observed when receivers are placed at optimal distances away from the source. Finally, Chapter 4 shows how DEM provides a unique opportunity to test how flow history and deposit emplacement processes may affect the metastability of granular piles, and provides a glimpse into how the methods of vibrational modes can be used to probe configurational stability. In this final chapter I will outline how future studies might build upon my results.

Chapters 2 and 3 show that DEM can be used to obtain a better understanding of internal granular flow processes. This can prove to be a powerful tool in building physics-based parameterizations of vertical fields such as velocity, dynamic pressures, and shear gradients. These parameterizations could then be linked to depth-averaged models thereby creating 2.5-D models. Keim and de' Michieli Vitturi [2025] does this in the context of depth-averaged models applied to dilute pyroclastic density currents. They use parameters derived from depth averaged models to then calculate velocity and concentration profiles by making assumptions about based in theory and observations. A better understanding of internal dynamics under conditions relevant to geophysical granular flows would allow researchers to apply similar methods in the context of concentrated granular flows using, for example, D-CLAW. If vertical gradients are derived from depth averaged parameters, then a coupling between the 2-D and proposed 2.5-D model may be developed such that, for example, shear localization that develops when boundary roughness is reduced might be used to predict particle segregation and improved predictions of depositional processes and dynamic pressures. Furthermore, this method would then be well poised to not only forward model potential seismic signals, but also can be used to make estimates on erosion and entrainment rates. Nevertheless, more numerical experiments are needed to understand a broader range of potential dynamic conditions developed from, for

example, wider grain-size distributions and non-spherical particles. Furthermore, these observations must also be linked to a clearer understanding of underlying physical processes.

In Chapter 3, I presented dynamical data measured at the base of the simulated granular flows, showing that there exists conditions under which a 'supported' plug-like flow regime can develop. In this regime, a dense plug flow is supported by a thin (a few grain diameters in size) boundary layer with a granular temperature at least an order of magnitude greater than that which is measured in the bulk. With this increase in basal granular temperature there is a decrease in the effective basal friction coefficient. This has been hypothesized to be a cause of the rather anomalous runout distances often observed in geophysical mass-flows [Campbell, 1989]. Researchers suggest that they observe this effect in bench-top experiments [Li et al., 2025]. Nevertheless, results in Chapter 3 show that relatively smooth substrates may be a requirement for the development of this 'supported' flow regime, and smooth substrates will necessarily allow flows to travel further distances. This occludes findings presented in Li et al. [2025], and indicates more effort is needed to understand how the effective basal-friction, especially in this supported regime, is related to bulk runout distance. Furthermore, Chapter 3 ends with simple 1-D steady-state wave propagation calculations through a uniform medium. Results from these calculations show that spectra recorded by receivers placed, not directly off channel, but 10 meters away, retain characteristics that can be linked to changes in flow-regime. This is due to the isolation of basal-force frequency bands that effectively encode transitions from quasi-static solid-like states, to liquid-like and gas-like flows. These calculations underscore the importance of receiver placement, which ultimately controls what flow information might be extracted from remote geophysical observations. While this exercise is instructive, it is not exhaustive. I suggest it should be conducted with empirical Green's functions (for example, those presented in Allstadt et al. [2020]), and with the incorporation of a signal-to-noise threshold condition. This will be a necessary step for a more refined, operationally relevant, understanding of what sort of information can be extracted from geophysical signals.

Finally, Chapter 4 shows that the stability of a granular pile on a slope is not just a function of the particle-scale properties, but also of the assemblage's configurational state. This is a hallmark of soft-matter materials and further exemplifies the complex

nature of these many-bodied systems. I show that memory of previous flow states and emplacement processes can directly affect how and when a particle assemblage will fail on time-varying slopes. Further, the methods of vibrational modes, calculated through the velocity auto-correlation function, may provide a means to predict bulk failure and jamming. I suggest that more effort is needed to explore what information is encoded within the density of vibrational modes, and if it can truly be used to predict failure and jamming. The density of vibrational modes can be a powerful tool as authors have shown that it can be inferred through acoustic measurements [Owens and Daniels, 2013, Brzinski and Daniels, 2018]. Moreover, it would be valuable to see if the density of vibrational modes can be used to probe static granular media, potentially giving a method to read-out memory encoded by the assemblage's configurational state. Moreover, this provides a avenue for exploring how granular materials may interact, and respond to, disparate fields, informing future geophysical measurements.

In summary, I have shown the power of discrete approaches to modeling geophysical granular flows. Though DEM reduces the amount of assumptions required for micro-scale particle-particle interactions, these models are intractable for modeling large scale flow phenomenon. Furthermore, DEM, as applied here, also requires it own assumptions in terms of, for example, how particle contacts are modeled at the sub-particle scale, the shape of the grains, and the grain-size distributions. Nevertheless, future implementations of exascale DEM solvers (e.g., MFiX-EXA) will allow researchers to simulate billions of particles with a variety of grain-sizes and shapes. This can prove a useful tool in improving reduced-dimension models, and simulating near-scale conditions. Nevertheless, numerical simulations are only one part of the picture, and information that they provide should always be used along side natural and experimental observations. Only then can we hope to develop a unified framework to describe and model geophysical granular flow phenomena.

APPENDIX
SUPPORTING INFORMATION FOR CHAPTER 2: BASAL FORCE FLUCTUATIONS AND GRANULAR RHEOLOGY: LINKING MACROSCOPIC DESCRIPTIONS OF GRANULAR FLOWS TO BED FORCES WITH IMPLICATIONS FOR MONITORING SIGNALS

A.1 CG parameters

Here, we will briefly describe coarse-grained parameters that are key to calculating non-dimensional parameters described in Section 2.2.2 and Appendix A.2. Detailed information on the coarse-graining (CG) technique used in this study can be found in Breard et al. [2020].

The CG method assumes that momentum is distributed through the system via non-instantaneous contacts between particles, whose contact area can be modeled as a contact point: particles are considered soft (i.e. collisions are not instantaneous) but hard enough such that particle deflections can be approximated to a point [Weinhart et al., 2013]. Our CG methods uses a peaked Gaussian function that is convolved with microscopic properties, effectively performing spatial smoothing with a width equal to $0.75d$, where d is the monodisperse particle diameter. Convolved particle mass and momentum are used to satisfy conservation of momentum and to derive a bulk stress tensor that is the sum of kinetic ($\bar{\bar{\sigma}}^{ki}$) and contact stresses ($\bar{\bar{\sigma}}^{c}$)

$$\bar{\bar{\sigma}} = \bar{\bar{\sigma}}^{ki} + \bar{\bar{\sigma}}^{c} \tag{A.1}$$

In this way, stresses are broken down into contributions that are a function of particle velocity fluctuations, i.e., $\bar{\bar{\sigma}}^{ki}$, and contributions that are a function of the contact forces between particles, i.e., $\bar{\bar{\sigma}}^{ki}$. From this macroscopic description of the stress field we can derive scalar parameters that will become important in scaling analyses (Sections 2.2.2 and A.2).

The solids pressure is defined by the trace of the total stress tensor

$$P_s = \frac{1}{3} tr(\bar{\bar{\sigma}}) \tag{A.2}$$

Similarly, the trace of the kinetic stress tensor gives the granular temperature under an isotropic assumption

$$T = \frac{1}{3\rho_s} tr(\bar{\bar{\sigma}}^{ki}) \tag{A.3}$$

Granular temperature is a parameter that is derived from kinetic theory applied to granular systems [Lun et al., 1984]. This parameter captures the squared average fluctuating particle velocity, providing a measure of the fluctuating component of kinetic energy in the system. Anisotropic granular temperature estimates may be defined via the corresponding positions in the main diagonal of the kinetic stress tensor

$$T = \frac{\bar{\bar{\sigma}}_{ii}^{ki}}{\rho_s} \tag{A.4}$$

We apply the plain strain assumption when calculating the deviatoric stress tensor

$$\sigma^D = \sigma^{2d} - \frac{1}{2} tr(\sigma^{2d}) \tag{A.5}$$

where $\sigma^{2d}$is the 2-D stress tensor composed of the x (stream-wise) and y (bed-normal) components of the total stress tensor $\bar{\bar{\sigma}}$. From this we calculate the magnitude of shear stresses as

$$|\sigma^D| = \sqrt{\frac{1}{2}\sigma_{ij}^D \sigma_{ij}^D} \tag{A.6}$$

Here, i and j are tensor indices, and repeated indices imply summation. Similarly, we can define the magnitude of the shear-rate from the averaged (in the span-wise z-direction) particle velocity and 2-D shear-rate tensor

$$|\dot{\gamma}| = \sqrt{\frac{1}{2}\sigma_{ij}^D \sigma_{ij}^D} \tag{A.7}$$

where $\dot{\gamma}_{ij}^D$ represents the domain averaged shear-rate deviator.

A.2 Scaling for viscous effects

Scaling relations are used to derive non-dimensional parameters that quantitatively access the dominate first-order mechanisms that occur in our simulated flows. Section 2.2.2 introduces disparate parameters that represent the various stress-states, as well as the competition between inertial and viscous properties. Among these non-dimensional parameters are the inertial number I:

$$I = \frac{\dot{\gamma} d}{\sqrt{\frac{P_s}{\rho_s}}} \tag{A.8}$$

Where $\dot{\gamma}$ is the magnitude of the coarse-grained shear-rate tensor, d is the particle diameter, P_s is the solid's pressure (or trace of the coarse-grained stress tensor), and ρ_s is the particle density. This quantity expresses the ratio between a microscopic timescale of particle rearrangement and a macroscopic timescale for bulk bed deformation. The ratio between grain inertia and viscous stresses is expressed by the viscous inertial number I_v:

$$I_v = \frac{\dot{\gamma}\eta_f}{P_s} \tag{A.9}$$

where η_f is the interstitial fluid viscosity. A similar ratio is given by the Stokes number St — a measure of grain inertia in an ambient flow field:

$$I_v = \frac{\dot{\gamma}d^2\rho_s}{\eta_f} \tag{A.10}$$

Finally, the modified inertial number I_m represents a quantity that combines the viscous and inertial numbers to unify the rheologies of dry-granular flows and dense suspensions. The first form of the modified inertial number I_m was introduced by Trulsson et al. [2012], and later was augmented by Amarsid et al. [2017] into the form:

$$I_m = \left(\alpha I_v + I^2\right)^{1/2} = I\left(\frac{\alpha}{St} + 1\right)^{1/2} \tag{A.11}$$

where α is a constant fitting parameter. This states that the modified inertial number simplifies to the dry inertial number I under two conditions: (1) the absence of an interstitial fluid (i.e., fluid viscosity $\eta_f = 0$ thus, $I_v = 0$) and (2) as $St \to \infty$.

We can visualize at what shear-rates viscous stresses will be important when estimating the inertial state of a flow by plotting the Stokes number for simulations conducted with an interstitial fluid (Figure A.32). The dashed line in Figure A.32 represents the point at which, given the scaled shear-rate expressed by I, grain-inertia overtakes viscous forcing imparted by the ambient flow field. As expected, this is highly dependent on grain size and interstitial fluid viscosity: simulations conducted in the presence of a viscous fluid ($\eta_f = 0.01$ Pa s) fall below the dashed line where $St = 1$. This suggests that when using the dry inertial number I as an estimate for the inertial state of simulations conducted with 500 micron particles submerged in a viscous fluid, the state will be underestimated (i.e., viscous effects will not be considered) when $I \leq 10^{-2}$. In effect, using the modified inertial number will shift

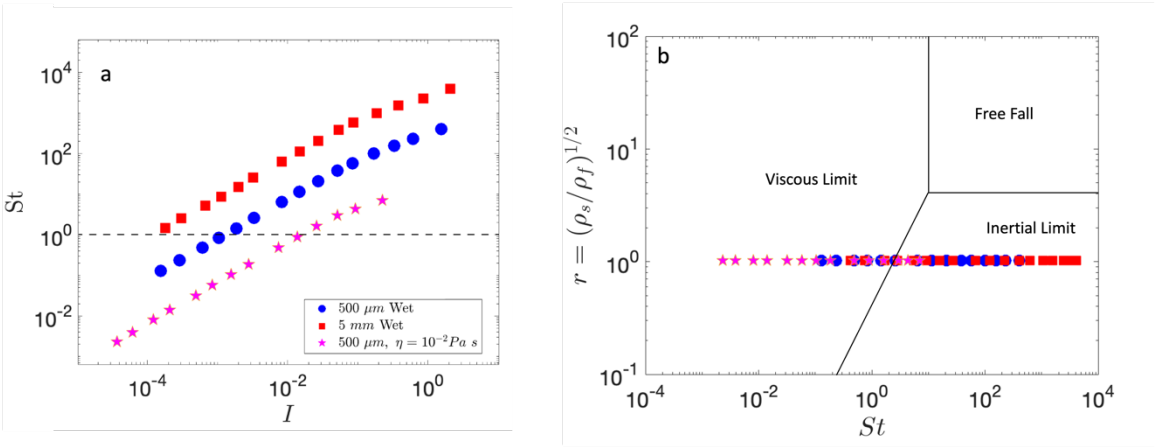

Figure A.32. Stokes number St as a function of dry inertial number I. Dashed line shows the point at which grain inertia dominates over fluid stresses. (b) Regimes defined by Courrech du Pont et al. [2003] for comparison.

any point that corresponds to $St < 1$ to the right in inertial space (Figure A.33). In terms of the granular rheology described by the effective friction coefficient μ and the solid particle concentration Φ, I_m aids in aligning the observed values calculated at low shear-rates for the small particle viscous fluid simulations with the rest of the results. Nevertheless, Figures A.33e and A.33f show that the non-dimensional granular temperature Θ ($\Theta = T\rho_s P_s^{-1}$, where T is the granular temperature) is drastically affected using I_m. Instead of aiding to collapse the data onto the curve which the dry experiments fall on (thus unifying the dynamics of dry and submerged granular flows), Im appears to cause a move-out away from the dry experiments which itself is dependent on fluid viscosity, suggesting that the dry inertial number is a much better predictor of granular temperature at a given shear-rate. The fact that granular temperature is better predicted by the dry inertial number, and the effect of using Im is minuscule in the context of the other rheological properties explored here (i.e., μ and Φ), we have opted to express our results in terms of the dry inertial number I.

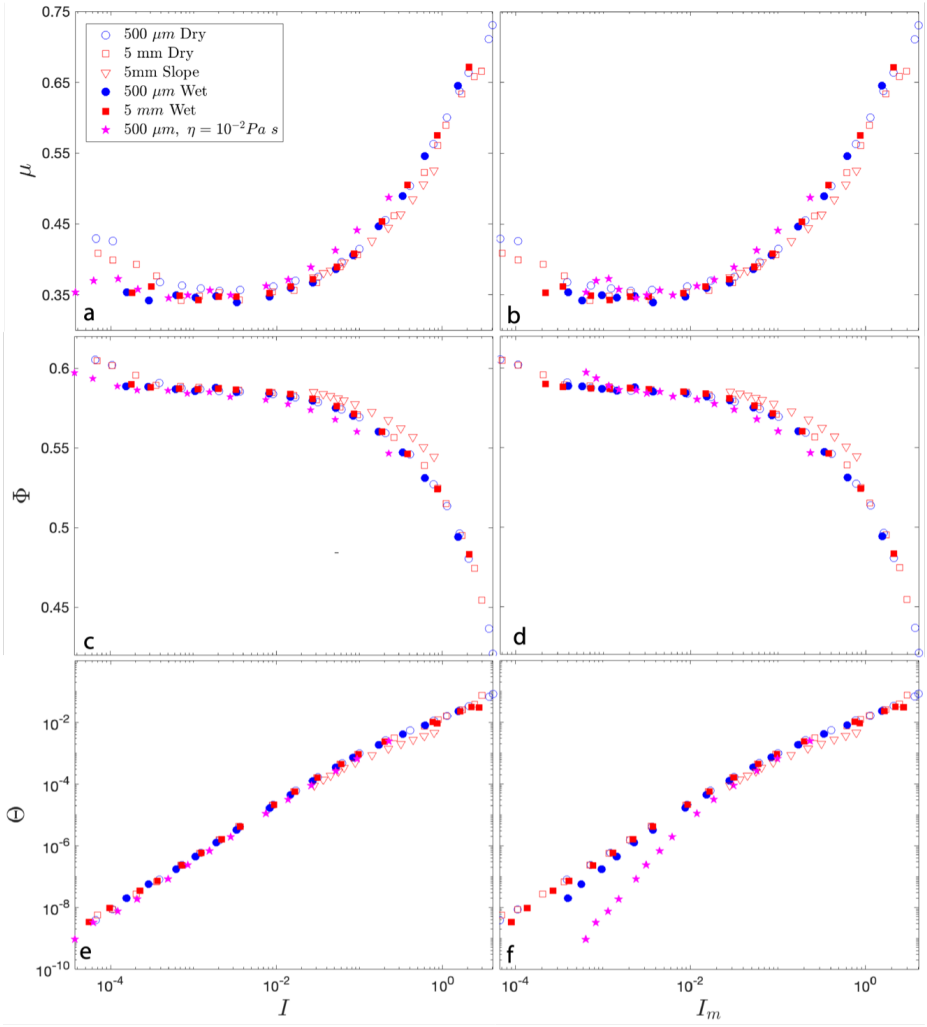

Figure A.33. Rheology of simulations expressed in terms of the effective friction coefficient μ, the solid particle concentration Φ, and the dimensionless granular temperature Θ as a function of dry inertial number I (a, c, e) and the modified inertial number I_m (b, d, f).

A.3 Basal roughness

To establish the bottom boundary (i.e., our numerical force-plate), we settle the particles, either under gravity or forcibly via the top flow driving plate (in the absence of gravity). Then, we fix the basal particles throughout time. To estimate surface roughness, we calculate the root mean square of the particle surfaces above a common center line

$$S_a = \left(\frac{1}{N} \Sigma z_i^2 \right)^{1/2} \tag{A.12}$$

N is the number of basal particles and z_i is the height of the i^{th} particle's surface above the laterally averaged particle height:

$$z_i = y_i - \bar{h} \tag{A.13}$$

Where $\bar{h}$ is the arithmetic mean of the laterally (i.e., z-direction) averaged basal-particle surface heights (Figure A.34)

$$h(x_j) = \frac{\Sigma A_{ji} y_i}{\Sigma A_{ji}} \tag{A.14}$$

A_{ji} is the cross-sectional area of the i^{th} particle's distance away from the lateral profile interval x_j.

Increasing the bottom plate roughness to size ratios greater than the flowing particles will likely affect the results. Basal roughness has been found to generate force and velocity fluctuations that can trigger slip events below a globally conditioned slip threshold [Artoni and Richard, 2015]. Thus, we would hypothesize that when $S_a > d$, velocity fluctuations would be primarily driven by flow-particle interactions with the base, effectively out competing the generation of fluctuations arising from flow driving forces (i.e., the top plate boundary condition in plane shear configurations, and gravity in inclined flow configurations). As we are considering how the bulk rheology relates to basal force fluctuations, through forcings that drive bulk flow, rather than how, secondarily, roughness affects granular rheology, our results are generally valid for conditions where $S_a \leq d$.

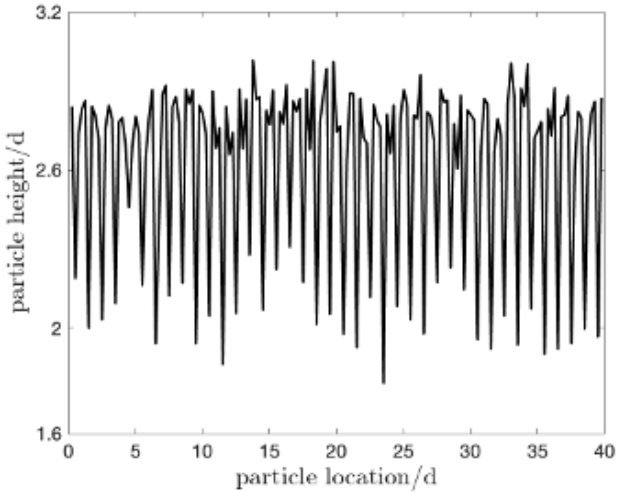

Figure A.34. Non-dimensional particle surface height of the particles composing the bottom 'force' plate, normalized by particle diameter. Heights are laterally averaged in the z-direction.

A.4 Defining steady state

In this study, we observe disparate granular flows under steady-state conditions. The purpose of this study is to examine the disparate rheological regimes, relating these regimes to basal force characteristics. This study follows numerical experiments performed by Cruz et al. [2005], where steady states were achieved in plane-shear configurations. While steady-state geophysical granular flows are unlikely in nature Iverson and Denlinger [2001], steady-state experiments and solutions can provide useful insights and points of comparisons to mathematical models. Further, steady-state experiments allow a first-order view into the physical processes that govern flow. This can provide a framework for a theoretical understanding of the driving processes that is independent of the seemingly aleatory nature of complex unsteady dynamics. Preparation of our steady-state experiments conducted in plane shear is as follows, particles settle to the bottom of the domain, establishing the bottom plate, once settling is complete by fixing the bottom of the simulated apparatus. Then, the top flow driving plate steadily shears the bed to allow it to find max packing. The top plate linearly accelerates to the prescribed top plate velocity (in Figure A.35, the prescribed final velocity is 0.005 m/s). Once the top plate reaches the desired velocity, the velocity is held until the time averaged average particle velocity over a 1 second interval is within less than 5% of the mean in the following interval (at higher plate

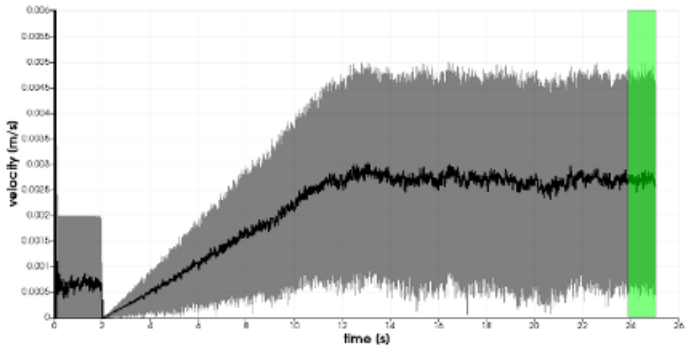

Figure A.35. Average particle velocity in the stream-wise direction (dark line), q1 and q3 quartiles (gray shading) vs time. Green box shows when bottom plate wall forces are recorded.

velocities, time averaged mean particle velocities vary less than 1% over steady-state intervals). Finally, the bottom plate forces are written at a frequency of 100 kHz.

A.5 Transitions into isotropic particle-contact regimes

A secondary view of anisotropy, and subsequent grading into relative isotropy at intermediate inertial numbers, is evidenced by the directionality of the contact forces. As the inertial number increases, the distribution of the directionality of contact forces changes (Figure A.36). For example, when $I < 10^{-3}$, high magnitude contact forces are concentrated within the first, second, and fourth quadrants (Figure A.36a). As $I < 10^{-2}$, high magnitude contact forces become more diffuse in all directions, with a bias in the direction of shear (second and fourth quadrant; Figure A.36b). This reflects the trend towards isotropic granular temperature at intermediate inertial numbers (Figure 4c). This diffuse nature becomes more biased in the direction of shear as I increases to the collisional limit (Figure A.36c-d). The grading of both the directionality of contact forces and granular temperature into an isotropic field variable supports the idea that isotropic conditions arise as momentum exchange is dominated by prolonged particle contacts, as is the phenomenological nature of dense granular flows at intermediate inertial numbers [Campbell, 1989, Forterre and Pouliquen, 2008].

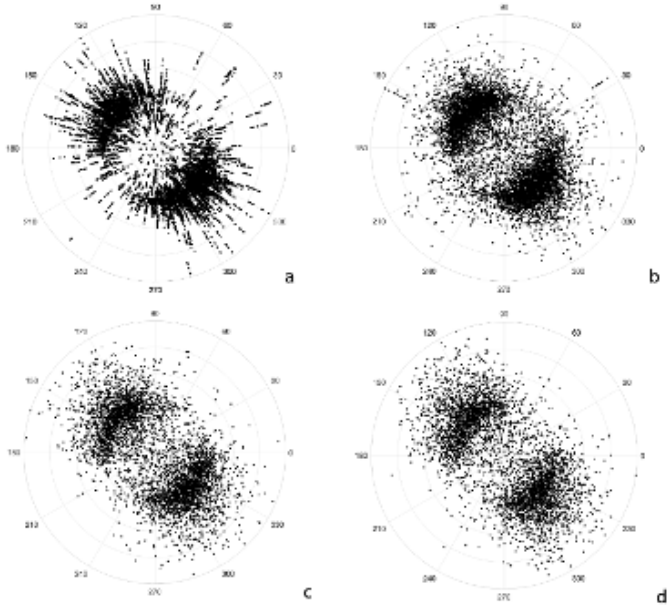

Figure A.36. Rose diagrams of contact forces during shear cell simulations, at inertial numbers: (a) $I < 10^{-3}$, (b) $I < 10^{-2}$, (c) $I < 10^{-1}$ and (d) $I < 10^{0}$, Angles labeled in the outer diameter are measured in respect to the stream-wise axis.

A.6 Granular temperature's configurational dependence

Figure 4 in the main text shows a direct relationship between non-dimensional granular temperature Θ and inertial number I. We use the definition of Θ given by Kim and Kamrin [2020]:

$$\Theta = \frac{T\rho_s}{P_s} \tag{A.15}$$

where T is granular temperature, ρ_s is the solid particle density, and P_s is the solid pressure. Plotting granular temperature T as a function of I shows the effect of non-dimensionalizing granular temperature (Figure A.37). Namely, this shows the effect of scaling granular temperature by the solid pressure (ρ_s is constant across all simulations). Figure A.37 shows that the magnitude of granular temperature generated by the incline-slope flows are nearly an order of magnitude lower than a plane-shear simulation at an equivalent inertial number. This reflects the fact that the incline-slope flows experience shear-rates that are much lower than the rates experienced by the plane-shear experiments conducted with particles of the same size. Granular temperature is primarily produced through two mechanisms: particle-contacts driving velocity fluctuations, and shear 'heating'

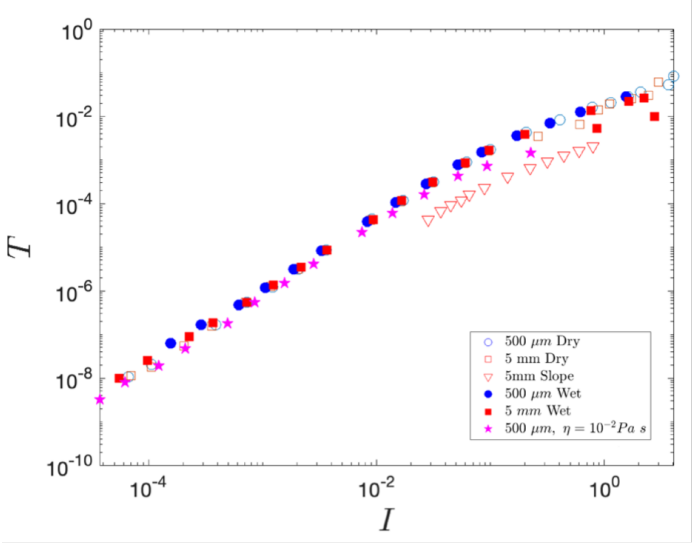

Figure A.37. Granular temperature under the isotropic assumption T as a function of inertial number I.

caused by particles advecting parallel to the shear-velocity gradient Campbell [2006]. Therefore, the shear-deficiency experienced by incline-slope flows, compared to plane-shear experiments at an equivalent inertial number, directly leads to a net decrease in granular temperature production. Rescaling granular temperature by the solid pressure, and the density of the particles, shows that the this deficiency can be accounted for when granular pressure is taken into consideration.

A.7 Scale dependence in basal-force spectra indicative of correlations in forcings

When modeling granular forces exerted on a substrate, it is common to assume that individual particle-forcings occur randomly (e.g., Tsai et al. [2012], Farin et al. [2019], Allstadt et al. [2020]). This assumption simplifies the calculation for a sum of particle-forcings by a flow on its substrate to a simply scale factor of a single particle-forcing. In effect, this assumption states that the forcing spectra generated by many particles in contact with the substrate, summed over the area of the flow's footprint, has the exact shape of the forcing generated from a single particle contact, with the amplitude scaled by the square root of the total number of forcings. Since we can observe all particle-forcings in our discrete element approach, we can see where this assumption breaks down.

First, we can define a scaled power spectral density as

$$P_1(f) = \frac{P(f)}{A_0} \tag{A.16}$$

Where P_1 is the scaled PSD (now being expressed in newtons squared per frequency per unit area), and A_0 is the experimental force plate area. Fig. A.38 depicts the RMS of scaled basal forcing spectra for five 5 mm experiments with inertial numbers ranging from 10^{-5}–10^{0}, and with three different plate areas depicted for each experiment (i.e., three different areas over which individual particle-forcings are summed over). In the low inertial to intermediate regime (i.e., $10^{-5} \leq I \leq 10^{-2}$ the spectra for forcings applied over the entire footprint of the experimental flow (i.e., $A_0 = (40d)^2$) shows a spectral 'hump' near 300 Hz whose amplitude is not captured by considering the scale of the numerical force plate (Figures A.38a-d). This hump is intrinsically related to particle size; when the particle size decreases to an order of magnitude from 5 mm to 500 microns the hump shifts by an order of magnitude to the right, from $\sim$ 300 Hz to $\sim$ 3000 Hz. The greatest scale effects are seen when the flow transitions from the intermediate regime into the collisional inertial limit when $I \sim 10^{-1}$ (Figure A.38d). Here, the spectrum that corresponds to a summation over the entire flow's footprint has a higher amplitude up to 200 Hz, then falls to the same curves as the smaller force plates. When the flow is well within the collisional limit ($I \sim 1$), scaling the PSD by the force plate area corrects for all amplitude effects and the general shape of the curve is maintained (Figure A.38e). This may suggest that as a flow transitions from a liquid-like state to a gas-like state (i.e., as inertial numbers become equal to, and greater than, 10^{-1}), particle forcings become more correlated in space, such that the assumption of random particle impacts breaks down in the lower frequency bands.

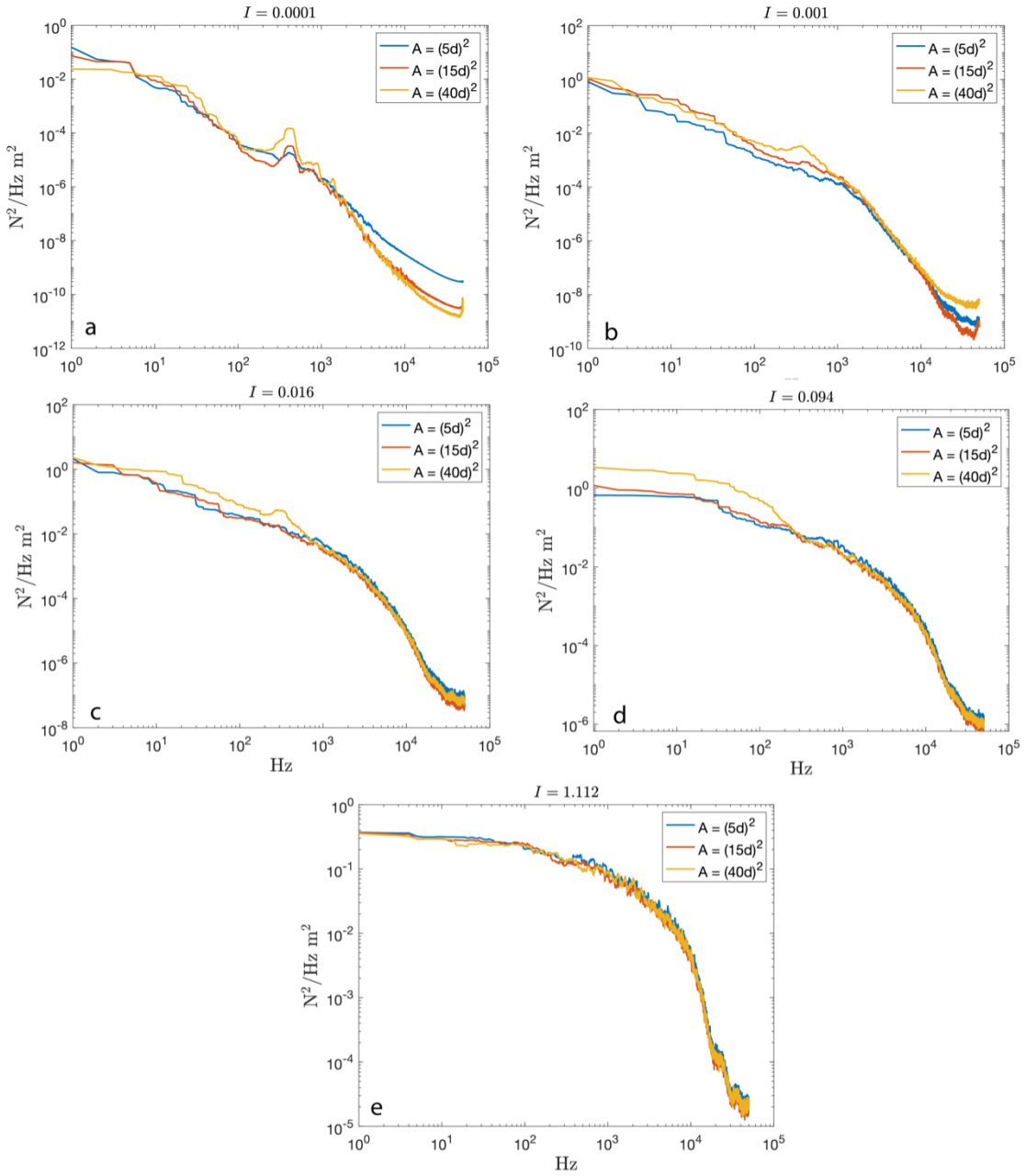

Figure A.38. The RMS amplitude of scaled PSDs from 5 mm plane-shear experiments with inertial numbers: $I \approx 10^{-4}$ (a), $I \approx 10^{-3}$ (b), $I \approx 10^{-2}$ (c), $I = 10^{-1}$ (d), and $I = 1$ (e). Each plot depicts three spectra that show the effect of decreasing the numerical force plate footprint from $A_0 = (40d)^2$ (the footprint of the entire flow) to $A_0 = (5d)^2$, where d is the diameter of the particles.

Bibliography

K. Aki and P. G. Richards. *Quantitative seismology*. University Science Books, Sausalito, Calif, 2nd ed. edition, 2002. ISBN 0935702962.

K. E. Allstadt, R. S. Matoza, A. B. Lockhart, S. C. Moran, J. Caplan-Auerbach, M. M. Haney, W. A. Thelen, and S. D. Malone. Seismic and acoustic signatures of surficial mass movements at volcanoes. *Journal of Volcanology and Geothermal Research*, 364:76–106, 2018.

K. E. Allstadt, M. Farin, R. M. Iverson, M. K. Obryk, J. W. Kean, V. C. Tsai, T. D. Rapstine, and M. Logan. Measuring basal force fluctuations of debris flows using seismic recordings and empirical green's functions. *Journal of Geophysical Research: Earth Surface*, 125, 2020.

L. Amarsid, J. Y. Delenne, P. Mutabaruka, Y. Monerie, F. Perales, and F. Radjai. Viscoinertial regime of immersed granular flows. *Physical Review E*, 96, 2017.

B. Andreotti, Y. Forterre, and O. Pouliquen. *Granular media: between fluid and solid*. Cambridge University Press, Cambridge, 1st edition, 2013. ISBN 1-316-09073-6.

M. Arran, A. Mangeney, J. D. Rosny, M. Farin, R. Toussaint, and O. Roche. Laboratory landquakes: Insights from experiments into the high-frequency seismic signal generated by geophysical granular flows. *Journal of Geophysical Research: Earth Surface*, 126, 2021.

R. Artoni and P. Richard. Effective wall friction in wall-bounded 3d dense granular flows. *Physical Review Letters*, 115, 2015.

D. Asenjo, F. Paillusson, and D. Frenkel. Numerical calculation of granular entropy. *Phys. Rev. Lett.*, 112, 2014. doi: 10.1103/PhysRevLett.112.098002.

R. A. Bagnold. Experiments on a gravity-free dispersion of large solid spheres in a newtonian fluid under shear. *Proceedings of the Royal Society of London. Series A, Mathematical and physical sciences*, 225, 1954.

A. Baldassarri, M. A. Annunziata, A. Gnoli, G. Pontuale, and A. Petri. Breakdown of scaling and friction weakening in intermittent granular flow. *Scientific reports*, 9(1), 2019.

R. P. Behringer and B. Chakraborty. The physics of jamming for granular materials: a review. *Reports on Progress in Physics*, 82(1), 2018.

M. C. Benage, J. Dufek, and P. A. Mothes. Quantifying entrainment in pyroclastic density currents from the tungurahua eruption, ecuador: Integrating field proxies with numerical simulations. *Geophysical Research Letters*, 43(13), 2016.

D. Berzi, J. T. Jenkins, and P. Richard. Extended kinetic theory for granular flow over and within an inclined erodible bed. *Journal of fluid mechanics*, 885, 2020.

S. Bharathraj and V. Kumaran. Effect of base topography on dynamics and transition in a dense granular flow. *Journal of Fluid Mechanics*, 832:600–640, 2017. doi: 10.1017/jfm.2017.683.

R. B. Bird. *Transport phenomena*. Wiley, New York, 1960. ISBN 047107392X.

F. Boyer, Élisabeth Guazzelli, and O. Pouliquen. Unifying suspension and granular rheology. *Physical Review Letters*, 107:1–5, 2011.

M. J. Branney and B. P. Kokelaar. Pyroclastic density currents and the sedimentation of ignimbrites, 2002.

E. C. Breard, L. Fullard, J. Dufek, M. Tennenbaum, A. N. Fernandez, and J.-F. Dietiker. Investigating the rheology of fluidized and non-fluidized gas-particle beds: implications for the dynamics of geophysical flows and substrate entrainment. *Granular Matter*, 24, 2022.

E. C. P. Breard, J. Dufek, L. Fullard, and A. Carrara. The basal friction coefficient of granular flows with and without excess pore pressure: Implications for pyroclastic density currents, water-rich debris flows, and rock and submarine avalanches. *Journal of Geophysical Research: Solid Earth*, 125:1–22, 2020.

E. C. P. Breard, J. Dufek, S. Charbonnier, V. Gueugneau, T. Giachetti, and B. Walsh. The fragmentation-induced fluidisation of pyroclastic density currents. *Nature communications*, 14, 2023.

E. C. P. Breard, L. Fullard, and J. Dufek. Rheology of granular mixtures with varying size, density, particle friction, and flow geometry. *Phys. Rev. Fluids*, 9:054303, 2024.

N. Brodu, R. Delannay, A. Valance, and P. Richard. New patterns in high-speed granular flows. *Journal of Fluid Mechanics*, 769:218–228, 2015.

T. A. Brzinski and K. E. Daniels. Sounds of failure: Passive acoustic measurements of excited vibrational modes. *Phys. Rev. Lett.*, 120, 2018. doi: 10.1103/PhysRevLett.120.218003.

E. Caglioti, V. Loreto, H. J. Herrmann, and M. Nicodemi. A "tetris-like" model for the compaction of dry granular media. *Physical review letters*, 79(8):1575–1578, 1997.

C. S. Campbell. The stress tensor for simple shear flows of a granular material. *Journal of fluid mechanics*, 203:449–473, 1989.

C. S. Campbell. Granular material flows - an overview. *Powder Technology*, 162:208–229, 2006.

S. J. Charbonnier, F. Garin, L. A. Rodríguez, K. Ayala, S. Cancel, R. Escobar-Wolf, G. Chigna, C. Chun-Quinillo, D. González, W. Chigna, K. Chun-Quinillo, R. Mérida, F. Juarez, and E. S. Calder. Unravelling the dynamics and hazards of the june 3rd, 2018, pyroclastic density currents at fuego volcano (guatemala). *Journal of Volcanology and Geothermal Research*, 436, 2023.

M. Chmiel, F. Walter, M. Wenner, Z. Zhang, B. W. McArdell, and C. Hibert. Machine learning improves debris flow warning. *Geophysical Research Letters*, 48, 2021.

M. H. Cohen and D. Turnbull. Molecular transport in liquids and glasses. *The Journal of Chemical Physics*, 31:1164–1169, 1959.

S. E. Cole, S. J. Cronin, S. Sherburn, and V. Manville. Seismic signals of snow-slurry iahars in motion: 25 september 2007, mt ruapehu, new zealand. *Geophysical Research Letters*, 36, 2009.

E. I. Corwin, H. M. Jaeger, and S. R. Nagel. Structural signature of jamming in granular media. *Nature*, 435(7045):1075–1078, 2005.

S. Courrech du Pont, P. Gondret, B. Perrin, and M. Rabaud. Granular avalanches in fluids. *Phys. Rev. Lett.*, 90:044301, 2003.

F. D. Cruz, S. Emam, M. Prochnow, J. N. Roux, and F. Chevoir. Rheophysics of dense granular materials: Discrete simulation of plane shear flows. *Physical Review E - Statistical, Nonlinear, and Soft Matter Physics*, 72, 2005.

V. Dansereau, V. Démery, E. Berthier, J. Weiss, and L. Ponson. Collective damage growth controls fault orientation in quasibrittle compressive failure. *Phys. Rev. Lett.*, 122, 2019. doi: 10.1103/PhysRevLett.122.085501.

P. G. de Gennes. Soft matter. *Science*, 256(5056):495–497, 1992. doi: 10.1126/science.256.5056.495.

P. G. de Gennes. Granular matter: a tentative view. *Rev. Mod. Phys.*, 71, 1999.

P. G. de Gennes. Soft matter: more than words. *Soft matter*, 1(1), 2005.

E. DeGiuli and M. Wyart. Friction law and hysteresis in granular materials. *Proceedings of the National Academy of Sciences of the United States of America*, 114:9284–9289, 2017.

R. Delannay, A. Valance, A. Mangeney, O. Roche, and P. Richard. Granular and particle-laden flows: From laboratory experiments to field observations. *Journal of Physics D: Applied Physics*, 50, 2017.

J. M. Dickey and A. Paskin. Computer simulation of the lattice dynamics of solids. *Phys. Rev.*, 188:1407–1418, 1969. doi: 10.1103/PhysRev.188.1407.

J. Dufek and M. Manga. In situ production of ash in pyroclastic flows. *Journal of Geophysical Research: Solid Earth*, 113, 2008.

A. Einstein. Eine neue bestimmung der moleküldimensionen. *Annalen der Physik*, 324(2):289–306, 1906.

A. Einstein. Berichtigung zu meiner arbeit: „eine neue bestimmung der moleküldimensionen. *Annalen der Physik*, 339(3):591–592, 1911.

J. Estep and J. Dufek. Substrate effects from force chain dynamics in dense granular flows. *Journal of Geophysical Research: Earth Surface*, 117(F1), 2012. doi: https://doi.org/10.1029/2011JF002125.

M. Farin, A. Mangeney, R. Toussaint, J. D. Rosny, N. Shapiro, T. Dewez, C. Hibert, C. Mathon, O. Sedan, and F. Berger. Characterization of rockfalls from seismic signal: Insights from laboratory experiments. *Journal of Geophysical Research: Solid Earth*, 120:7102–7137, 2015.

M. Farin, A. Mangeney, J. de Rosny, R. Toussaint, and P. T. Trinh. Link between the dynamics of granular flows and the generated seismic signal: Insights from laboratory experiments. *Journal of Geophysical Research: Earth Surface*, 123: 1407–1429, 2018.

M. Farin, V. C. Tsai, M. P. Lamb, and K. E. Allstadt. A physical model of the high-frequency seismic signal generated by debris flows. *Earth Surface Processes and Landforms*, 44(13), 2019. doi: https://doi.org/10.1002/esp.4677.

B. Ferdowsi, C. P. Ortiz, and D. J. Jerolmack. Glassy dynamics of landscape evolution. *Proceedings of the National Academy of Sciences*, 115(19):4827–4832, 2018. doi: 10.1073/pnas.1715250115.

Y. Forterre and O. Pouliquen. Flows of dense granular media. *Annual Review of Fluid Mechanics*, 40:1–24, 2008.

D. Frenkel. Soft condensed matter. *Physica A*, 313(1):1–31, 2002.

L. A. Fullard, E. C. Breard, C. E. Davies, A. J. Godfrey, M. Fukuoka, A. Wade, J. Dufek, and G. Lube. The dynamics of granular flow from a silo with two symmetric openings. *Proceedings of the Royal Society A: Mathematical, Physical and Engineering Sciences*, 475, 2019.

F. Gadala-Maria and A. Acrivos. Shear-induced structure in a concentrated suspension of solid spheres. *Journal of rheology*, 24(6):799–814, 1980.

M. Galanis, M. D. Shattuck, C. S. O'Hern, and N. T. Ouellette. Directional strengthening and weakening in hydrodynamically sheared granular beds. *Physical review fluids*, 7, 2022.

K. L. Galloway, E. G. Teich, X. G. Ma, C. Kammer, I. R. Graham, N. C. Keim, C. Reina, D. J. Jerolmack, A. G. Yodh, and P. E. Arratia. Relationships between structure, memory and flow in sheared disordered materials. *Nature physics*, 18(5): 565–570, 2022.

E. Gardel, E. Sitaridou, K. Facto, E. Keene, K. Hattam, N. Easwar, and N. Menon. Dynamical fluctuations in dense granular flows. *Philosophical transactions of the Royal Society of London. Series A: Mathematical, physical, and engineering sciences*, 367(1909):5109–5121, 2009.

R. Garg, J. Galvin, T. Li, and S. Pannala. Open-source mfix-dem software for gas–solids flows: Part i—verification studies. *Powder technology*, 220:122–137, 2012.

Z. Ge, T. Man, H. E. Huppert, K. M. Hill, and S. A. Galindo-Torres. Unifying length-scale-based rheology of dense suspensions. *Phys. Rev. Fluids*, 9:L012302, 2024.

D. L. George and R. M. Iverson. A depth-averaged debris-flow model that includes the effects of evolving dilatancy. ii. numerical predictions and experimental tests. *Proceedings of the Royal Society. A, Mathematical, physical, and engineering sciences*, 470(2170), 2014.

D. Gidaspow. *Multiphase flow and fluidization*. Academic Press, Boston, MA, 1994.

F. Gimbert, V. C. Tsai, and M. P. Lamb. A physical model for seismic noise generation by turbulent flow in rivers. *Journal of Geophysical Research: Earth Surface*, 119 (10):2209–2238, 2014. doi: https://doi.org/10.1002/2014JF003201.

I. Goldhirsch. Introduction to granular temperature. *Powder technology*, 182(2): 130–136, 2008.

Y. Gu, A. Ozel, and S. Sundaresan. Rheology of granular materials with size distributions across dense-flow regimes. *Powder technology*, 295:322–329, 2016.

Guazzelli. Rheology of dense granular suspensions across flow regimes. *Physical review fluids*, 9(9), 2024.

A. J. Holyoake and J. N. McElwaine. High-speed granular chute flows. *Journal of fluid mechanics*, 710:35–71, 2012.

M. Houssais and D. J. Jerolmack. Toward a unifying constitutive relation for sediment transport across environments. *Geomorphology*, 277:251–264, 2017.

M. Houssais, C. P. Ortiz, D. J. Durian, and D. J. Jerolmack. Rheology of sediment transported by a laminar flow. *Phys. Rev. E*, 94, 2016. doi: 10.1103/PhysRevE.94.062609.

R. M. Iverson. The physics of debris flows. *Reviews of Geophysics*, 35:245–296, 1997.

R. M. Iverson and R. P. Denlinger. Flow of variably fluidized granular masses across three-dimensional terrain: 1. coulomb mixture theory. *Journal of Geophysical Research: Solid Earth*, 106, 2001.

R. M. Iverson and D. L. George. A depth-averaged debris-flow model that includes the effects of evolving dilatancy. i. physical basis. *Proceedings of the Royal Society. A, Mathematical, physical, and engineering sciences*, 470(2170), 2014.

R. M. Iverson, M. E. Reid, and R. G. LaHusen. Debris-flow mobilization from landslides. *Annual Review of Earth and Planetary Sciences*, 25, 1997. doi: https://doi.org/10.1146/annurev.earth.25.1.85.

R. M. Iverson, M. Logan, R. G. LaHusen, and M. Berti. The perfect debris flow? aggregated results from 28 large-scale experiments. *Journal of Geophysical Research*, 115(F3), 2010.

P. Jalali, J. Ritvanen, and P. Sarkomaa. Stress fluctuations in monodisperse and bidisperse rapid granular shear flows. *Physica A theoretical and statistical physics.*, 369(2), 2006.

J. T. Jenkins and S. B. Savage. A theory for the rapid flow of identical, smooth, nearly elastic, spherical particles. *Journal of Fluid Mechanics*, 130:187–202, 1983. doi: 10.1017/S0022112083001044.

D. J. Jerolmack and K. E. Daniels. Viewing earth's surface as a soft-matter landscape. *Nature reviews physics*, 1(12):716–730, 2019.

L. Jing, C. Y. Kwok, Y. F. Leung, and Y. D. Sobral. Characterization of base roughness for granular chute flows. *Physical review. E*, 94(5-1), 2016.

L. Jing, J. M. Ottino, R. M. Lueptow, and P. B. Umbanhowar. A unified description of gravity- and kinematics-induced segregation forces in dense granular flows. *Journal of Fluid Mechanics*, 925, 2021. doi: 10.1017/jfm.2021.688.

C. G. Johnson, B. P. Kokelaar, R. M. Iverson, M. Logan, R. G. LaHusen, and J. M. N. T. Gray. Grain-size segregation and levee formation in geophysical mass flows. *Journal of Geophysical Research: Earth Surface*, 117, 2012. doi: https://doi.org/10.1029/2011JF002185.

P. C. Johnson and R. Jackson. Frictional-collisional constitutive relations for granular materials, with application to plane shearing. *Journal of Fluid Mechanics*, 176:67–93, 1987.

P. Jop, Y. Forterre, and O. Pouliquen. A constitutive law for dense granular flows. *Nature*, 441:727–730, 2006.

C. Josserand, A. Tkachenko, D. Mueth, and H. Jaeger. Memory effects in granular materials. *Physical review letters*, 85:3632–3635, 2000.

J. W. Kean, J. A. Coe, V. Coviello, J. B. Smith, S. W. McCoy, and M. Arattano. Estimating rates of debris flow entrainment from ground vibrations. *Geophysical research letters*, 42(15):6365–6372, 2015.

B. Keim and M. de' Michieli Vitturi. Beyond the average: Computation of vertical profiles in dilute pyroclastic density currents and their use in shallow-water models. *Journal of Geophysical Research: Solid Earth*, 130(1), 2025.

N. C. Keim, J. D. Paulsen, Z. Zeravcic, S. Sastry, and S. R. Nagel. Memory formation in matter. *Rev. Mod. Phys.*, 91, 2019. doi: 10.1103/RevModPhys.91.035002.

T. Keyes. Instantaneous normal mode approach to liquid state dynamics. *The Journal of Physical Chemistry A*, 101(16):2921–2930, 1997. doi: 10.1021/jp963706h.

M. Kheiripour Langroudi, J. Sun, S. Sundaresan, and G. Tardos. Transmission of stresses in static and sheared granular beds: The influence of particle size, shearing rate, layer thickness and sensor size. *Powder technology*, 203(1):23–32, 2010.

S. Kim and K. Kamrin. Power-law scaling in granular rheology across flow geometries. *Physical Review Letters*, 125, 2020.

B. Kokelaar, R. Graham, J. Gray, and J. Vallance. Fine-grained linings of leveed channels facilitate runout of granular flows. *Earth and Planetary Science Letters*, 385:172–180, 2014.

K. Konno and T. Ohmachi. Ground-motion characteristics estimated from spectral ratio between horizontal and vertical components of microtremor. *Bulletin of the Seismological Society of America*, 88(1):228–241, 1998. doi: 10.1785/BSSA0880010228.

R. Kostynick, H. Matinpour, S. Pradeep, S. Haber, A. Sauret, E. Meiburg, T. Dunne, P. Arratia, and D. Jerolmack. Rheology of debris flow materials is controlled by the distance from jamming. *Proceedings of the National Academy of Sciences*, 119 (44), 2022. doi: 10.1073/pnas.2209109119.

C. Levy, A. Mangeney, F. Bonilla, C. Hibert, E. S. Calder, and P. J. Smith. Friction weakening in granular flows deduced from seismic records at the soufrière hills volcano, montserrat. *Journal of Geophysical Research: Solid Earth*, 120:7536–7557, 2015.

T. Li, R. Garg, J. Galvin, and S. Pannala. Open-source mfix-dem software for gas-solids flows: Part ii — validation studies. *Powder technology*, 220:138–150, 2012.

T. Li, Y. Wang, Q. Cheng, Q. Lin, J. Ming, K. Li, A. Shi, L. Gou, and X. Wei. Basal stresses and seismic signals generated by laboratory granular flows: The role of basal particle agitation in flow mobility. *Journal of geophysical research. Earth surface*, 130(3), 2025.

A. J. Liu and S. R. Nagel. The jamming transition and the marginally jammed solid. *Annual review of condensed matter physics*, 1(1):347–369, 2010.

M. Logan, R. M. Iverson, and M. K. Obryk. Video documentation of experiments at the usgs debris-flow flume 1992–2017. U.s. geological survey open-file report 2007–1315, United States Geologic Survey, 2018.

G. Lois, A. Lemaître, and J. M. Carlson. Spatial force correlations in granular shear flow. i. numerical evidence. *Phys. Rev. E*, 76:021302, 2007. doi: 10.1103/PhysRevE.76.021302.

E. Longhi, N. Easwar, and N. Menon. Large force fluctuations in a flowing granular medium. *Physical review letters*, 89, 2002.

G. Lube, E. C. Breard, J. Jones, L. Fullard, J. Dufek, S. J. Cronin, and T. Wang. Generation of air lubrication within pyroclastic density currents. *Nature Geoscience*, 12:381–386, 2019.

G. Lube, E. C. P. Breard, T. Esposti-Ongaro, J. Dufek, and B. Brand. Multiphase flow behaviour and hazard prediction of pyroclastic density currents. *Nature Reviews Earth and Environment*, 1:348–365, 2020.

C. K. Lun, S. B. Savage, D. J. Jeffrey, and N. Chepurniy. Kinetic theories for granular flow: Inelastic particles in couette flow and slightly inelastic particles in a general flowfield. *Journal of Fluid Mechanics*, 140, 1984.

T. S. Majmudar and R. P. Behringer. Contact force measurements and stress-induced anisotropy in granular materials. *Nature*, 435, 2005.

M. R. Maxey and J. J. Riley. Equation of motion for a small rigid sphere in a nonuniform flow. *The Physics of Fluids*, 26(4):883–889, 1983.

S. W. McCoy, J. W. Kean, J. A. Coe, G. E. Tucker, D. M. Staley, and T. A. Wasklewicz. Sediment entrainment by debris flows: In situ measurements from the headwaters of a steep catchment. *Journal of Geophysical Research: Earth Surface*, 117, 2012. doi: https://doi.org/10.1029/2011JF002278.

S. W. McCoy, G. E. Tucker, J. W. Kean, and J. A. Coe. Field measurement of basal forces generated by erosive debris flows. *Journal of Geophysical Research: Earth Surface*, 118:589–602, 2013.

M. Mehrabadi, S. Tenneti, R. Garg, and S. Subramaniam. Pseudo-turbulent gas-phase velocity fluctuations in homogeneous gas–solid flow: fixed particle assemblies and freely evolving suspensions. *Journal of Fluid Mechanics*, 770:210–246, 2015.

G. D. R. MiDi. On dense granular flows. *European Physical Journal E*, 14:341–365, 2004.

S. R. Nagel. Experimental soft-matter science. *Reviews of modern physics*, 89(2), 2017.

A. K. Naismith, I. Matthew Watson, R. Escobar-Wolf, G. Chigna, H. Thomas, D. Coppola, and C. Chun. Eruption frequency patterns through time for the current

(1999–2018) activity cycle at volcán de fuego derived from remote sensing data: Evidence for an accelerating cycle of explosive paroxysms and potential implications of eruptive activity. *Journal of volcanology and geothermal research*, 371:206–219, 2019.

C. Ness and J. Sun. Flow regime transitions in dense non-brownian suspensions: Rheology, microstructural characterization, and constitutive modeling. *Physical Review E - Statistical, Nonlinear, and Soft Matter Physics*, 91, 2015.

D.-H. Nguyen, E. Azéma, P. Sornay, and F. Radjai. Effects of shape and size polydispersity on strength properties of granular materials. *Phys. Rev. E*, 91, 2015.

C. S. O'Hern, L. E. Silbert, A. J. Liu, and S. R. Nagel. Jamming at zero temperature and zero applied stress: The epitome of disorder. *Phys. Rev. E*, 68, 2003. doi: 10.1103/PhysRevE.68.011306.

E. T. Owens and K. E. Daniels. Acoustic measurement of a granular density of modes. *Soft Matter*, 9:1214–1219, 2013. doi: 10.1039/C2SM27122B.

J. D. Paulsen, N. C. Keim, and S. R. Nagel. Multiple transient memories in experiments on sheared non-brownian suspensions. *Phys. Rev. Lett.*, 113, 2014. doi: 10.1103/PhysRevLett.113.068301.

P.-E. Peyneau and J.-N. Roux. Frictionless bead packs have macroscopic friction, but no dilatancy. *Phys. Rev. E*, 78, 2008. doi: 10.1103/PhysRevE.78.011307.

M. Piantini, F. Gimbert, E. Korkolis, R. Rousseau, H. Bellot, and A. Recking. Solid concentration as a main proxy for basal force fluctuations generated by highly concentrated sediment flows. *Geophysical Research Letters*, 50(1), 2023.

O. Pouliquen. Scaling laws in granular flows down rough inclined planes. *Physics of fluids*, 11:542–548, 1999.

S. Pradeep, P. E. Arratia, and D. J. Jerolmack. Origins of complexity in the rheology of soft earth suspensions. *Nature communications*, 15, 2024.

J. Ren, J. A. Dijksman, and R. P. Behringer. Reynolds pressure and relaxation in a sheared granular system. *Phys. Rev. Lett.*, 110, 2013. doi: 10.1103/PhysRevLett.110.018302.

G. Risica, M. Rosi, M. Pistolesi, F. Speranza, and M. J. Branney. Deposit-derived block-and-ash flows: The hazard posed by perched temporary tephra accumulations on volcanoes; 2018 fuego disaster, guatemala. *Journal of geophysical research. Solid earth*, 127(6), 2022.

F. M. Rocha, C. G. Johnson, and J. M. N. T. Gray. Self-channelisation and levee formation in monodisperse granular flows. *Journal of Fluid Mechanics*, 876: 591–641, 2019. doi: 10.1017/jfm.2019.518.

O. Roche. Depositional processes and gas pore pressure in pyroclastic flows: an experimental perspective. *Bulletin of volcanology*, 74:1807–1820, 2012.

D. Schofield and P. Wroth. *Critical state soil mechanics*. McGraw-Hill, London, 1968.

S. Shipley and A. M. Sarna-Wojcicki. Distribution, thickness, and mass of late pleistocene and holocene tephra from major volcanoes in the northwestern united states: A preliminary assessment of hazards from volcanic ejecta to nuclear reactors in the pacific northwest. Technical report, U.S. Geological Survey, 1993.

L. E. Silbert, A. J. Liu, and S. R. Nagel. Vibrations and diverging length scales near the unjamming transition. *Phys. Rev. Lett.*, 95, 2005. doi: 10.1103/PhysRevLett.95.098301.

S. Siman-Tov and E. E. Brodsky. Distinguishing between rheophysical regimes of fluid-saturated granular-flows using dilatancy and acoustic emission measurements. *Granular matter*, 23(2), 2021.

S. Stein and M. Wysession. *An introduction to seismology, earthquakes, and earth structure*. Blackwell, Malden, MA, 2003.

Q. Sun, F. Jin, J. Liu, and G. Zhang. Understanding force chains in dense granular materials. *International journal of modern physics. B, Condensed matter physics, statistical physics, applied physics*, 24(29):5743–5759, 2010.

M. Syamlal. Mfix documentation numerical technique. Technical report, EG and G Technical Services of West Virginia, Inc., Morgantown, WV (United States), 1998. URL `https://www.osti.gov/biblio/656644`.

M. Syamlal, W. Rogers, and T. J. O'Brien. MFIX Documentation Theory Guide. Technical report, U.S. Department of Energy, Morgantown, WV, 1993.

N. Taberlet, P. Richard, J. T. Jenkins, and R. Delannay. Density inversion in rapid granular flows : the supported regime. *The European physical journal. E, Soft matter and biological physics*, 22(1):17–24, 2007.

A. Tanguy, B. Mantisi, and M. Tsamados. Vibrational modes as a predictor for plasticity in a model glass. *Europhysics Letters*, 90(1), 2010. doi: 10.1209/0295-5075/90/16004.

M. Toiya, J. Stambaugh, and W. Losert. Transient and oscillatory granular shear flow. *Phys. Rev. Lett.*, 93, 2004. doi: 10.1103/PhysRevLett.93.088001.

A. Tordesillas, J. Shi, and T. Tshaikiwsky. Stress-dilatancy and force chain evolution. *International journal for numerical and analytical methods in geomechanics*, 35: 264–292, 2011.

M. Trulsson, B. Andreotti, and P. Claudin. Transition from the viscous to inertial regime in dense suspensions. *Physical Review Letters*, 109, 2012.

V. C. Tsai, B. Minchew, M. P. Lamb, and J.-P. Ampuero. A physical model for seismic noise generation from sediment transport in rivers. *Geophysical Research Letters*, 39(2), 2012. doi: https://doi.org/10.1029/2011GL050255.

Y. Tsuji, T. Tanaka, and T. Ishida. Lagrangian numerical simulation of plug flow of cohesionless particle in a horizontal pipe. *Powder Technology*, 71:239–250, 1992.

D. R. Tunuguntla, A. R. Thornton, and T. Weinhart. From discrete elements to continuum fields: Extension to bidisperse systems. *Computational particle mechanics*, 3(3):349–365, 2016.

J. W. Vallance and R. M. Iverson. Chapter 37 - lahars and their deposits. In H. Sigurdsson, editor, *The Encyclopedia of Volcanoes (Second Edition)*, pages 649–664. Academic Press, Amsterdam, second edition edition, 2015. ISBN 978-0-12-385938-9. doi: https://doi.org/10.1016/B978-0-12-385938-9.00037-7.

L. Vanel, D. Howell, D. Clark, R. P. Behringer, and E. Clément. Memories in sand: Experimental tests of construction history on stress distributions under sandpiles. *Phys. Rev. E*, 60, 1999. doi: 10.1103/PhysRevE.60.R5040.

E. H. Vanmarcke. Properties of spectral moments with applications to random vibration. *Journal of engineering mechanics*, 98:425–446, 1972.

J. L. Vinningland, Øistein Johnsen, E. G. Flekkøy, R. Toussaint, and K. J. Måløy. Granular rayleigh-taylor instability: Experiments and simulations. *Physical Review Letters*, 99, 2007.

B. Walsh, V. Coviello, L. Capra, J. Procter, and V. Márquez-Ramirez. Insights into the internal dynamics of natural lahars from analysis of 3-component broadband seismic signals at volcán de colima, mexico. *Frontiers in Earth Science*, 8, 2020.

T. Weinhart, R. Hartkamp, A. R. Thornton, and S. Luding. Coarse-grained local and objective continuum description of three-dimensional granular flows down an inclined surface. *Physics of Fluids*, 25, 2013.

T. Weinhart, C. Labra, S. Luding, and J. Y. Ooi. Influence of coarse-graining parameters on the analysis of dem simulations of silo flow. *Powder Technology*, 293:138–148, 2016.

Wyart, M. On the rigidity of amorphous solids. *Ann. Phys. Fr.*, 30(3):1–96, 2005. doi: 10.1051/anphys:2006003.

B. Yohannes, L. Hsu, W. E. Dietrich, and K. M. Hill. Boundary stresses due to impacts from dry granular flows. *Journal of Geophysical Research: Earth Surface*, 117, 2012.

A. B. Yu and N. Standish. Estimation of the porosity of particle mixtures by a linear-mixture packing model. *Industrial engineering chemistry research*, 30(6): 1372–1385, 1991.

D. Zeyl and B. Sattler. Plato's Timaeus. In E. N. Zalta and U. Nodelman, editors, *The Stanford Encyclopedia of Philosophy*. Metaphysics Research Lab, Stanford University, Fall 2023 edition, 2023.

Q. Zhang and K. Kamrin. Microscopic description of the granular fluidity field in nonlocal flow modeling. *Physical Review Letters*, 118, 2017.

P. J. Zrelak, E. C. P. Breard, and J. Dufek. Basal force fluctuations and granular rheology: Linking macroscopic descriptions of granular flows to bed forces with implications for monitoring signals. *Journal of geophysical research. Earth surface*, 129(7), 2024.